EASA
European Aviation Safety Agency

Final Report EASA_REP_RESEA_2008_5

Research Project:

Hail Threat Standardisation

An agency of the European Union

Disclaimer

This study has been carried out for the European Aviation Safety Agency by an external organization and expresses the opinion of the organization undertaking the study. It is provided for information purposes only and the views expressed in the study have not been adopted, endorsed or in any way approved by the European Aviation Safety Agency. Consequently it should not be relied upon as a statement, as any form of warranty, representation, undertaking, contractual, or other commitment binding in law upon the European Aviation Safety Agency.

Hail Threat Standardisation
FINAL report for EASA.2008.OP.25

Date: 20th November 2009 (revised 11th November 2010)

Authors: Field P.R., Hand W., Cappelluti G., McMillan A., Foreman A., Stubbs D. and Willows M.

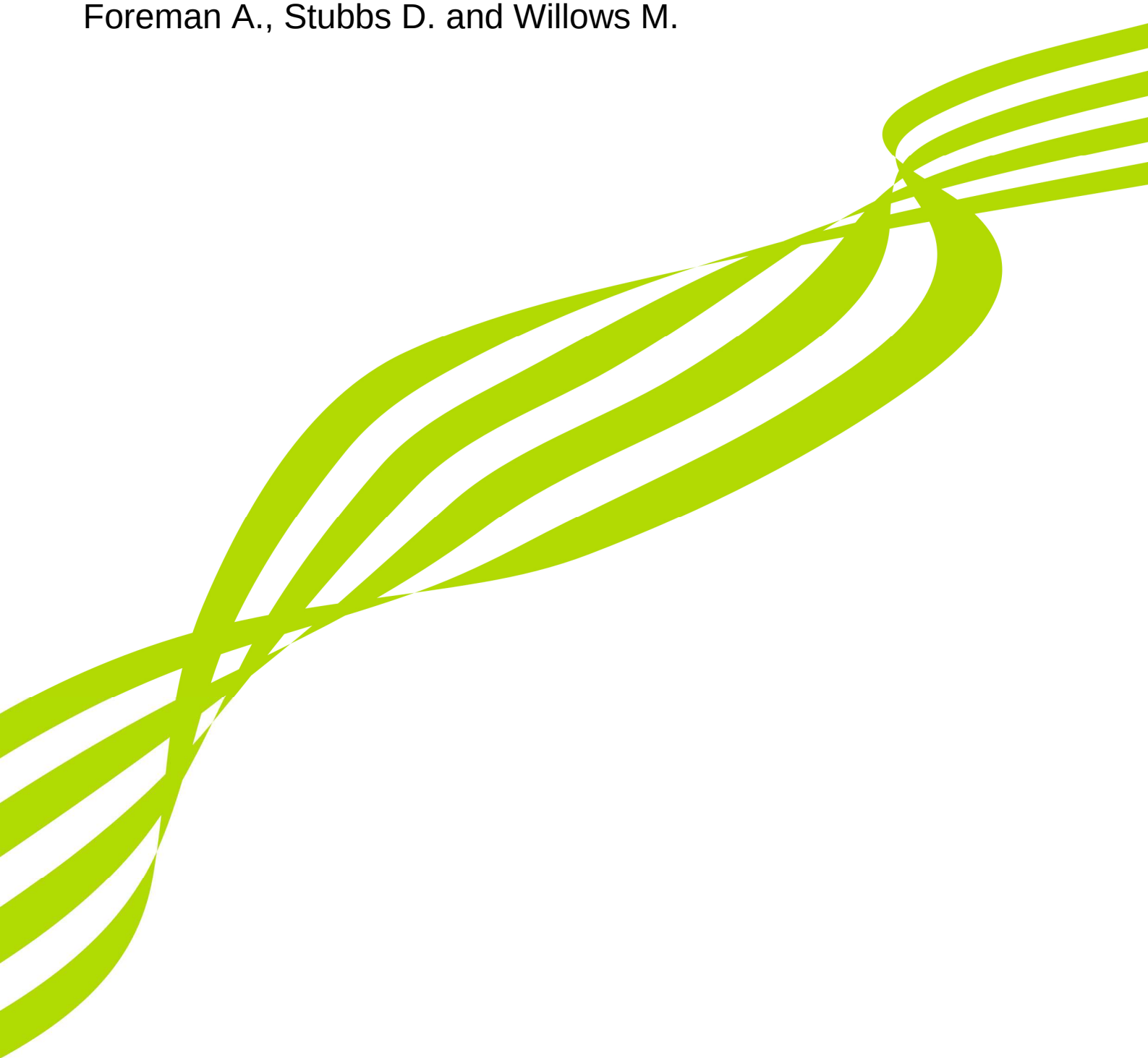

Table of Contents

List of Figures

List of tables

GROUND IN HAIL CASE. THE CUMULATIVE PROBABILITY COLUMN INDICATES THE PROBABILITY OF OBSERVING A HAILSTONE SIZE SMALLER THAN THE SIZE GIVEN IN THE FIRST COLUMN. THEREFORE, THE PROBABILITY OF OBSERVING A HAILSTONE LARGER THAN A GIVEN SIZE IS 1-CUMULATIVE PROBABILITY. 130

Acknowledgements

This study was funded by EASA: EASA.2008.OP.25

We acknowledge use of lightning data from NASA. TRMM radar data from NASA and the University of Utah. Hail reports from the Storm Prediction Center.

1 Executive Summary

The aims of this work were to review the existing literature of global hail threat data, develop a climatology for hail, review the existing regulatory frameworks with reference to hail threat and understand how the threat varies across the aircraft for different materials. This study provides a foundation for developing a Hail Threat Standard.

The literature review indicated that a worst case hail density of 917 kg m^{-3} would be appropriate for safety applications. Similarly, the worst case fallspeed relationship as a function of air density is $V(m/s) = \rho_{air}(kg/m^3)^{-1/2} 156 D(m)^{1/2}$.

To produce a globally consistent climatology of hail two general approaches were considered, but only the latter was able to provide climatological information in three dimensions. The first was a numerical weather prediction model (NWP) based approach where hail was diagnosed from environmental variables obtained from an atmospheric global circulation model. The NWP-model-based hail prediction used to provide global climatological data is empirically based relating ground observations of hail size to radiosonde measurements of upper air temperature and humidity structures over the USA. Data was obtained for 274 occasions of hail during the period from Jan 1st 1950 through to 1953. The hail observations had sizes ranging from 3mm to 100mm with 166 observations having diameters less than 12mm. The NWP-model-based results were extended to make allowance for melting of hailstones which was in line with recommendations made in the original paper. A second approach was to make use of radar observations from space. These data provide a vertical profiling capability associated with a relatively small sampling area. The radar based approach was compared against ground based hail observations over the USA from 1998 to 2006. Radar data were used to provide a hail threat by estimating hail occurrence and the likelihood of collision within three temperature ranges.

Hail occurrence is largely confined to land areas and has a strong diurnal character with the peak in observations occurring in the late afternoon. Outside of the tropics a seasonal peak in hail occurrence is observed in early summer. Radar observations suggest that hail is more frequent close to the freezing level than at colder temperatures (higher altitudes).

Using the radar approach and assuming a worst case situation, hail sizes that are intercepted for 'random flying' at approximately the 10^{-5} probability event level are about 70 mm for the -2 to -5C and -15 to -20C temperature ranges, but much smaller (less than 10 mm) for the -35 to -40C range. At the 10^{-3} probability event level the hail sizes are much smaller than 10mm at all temperatures. These values are similar for an aircraft intercepting particles along the leading edge and from above assuming forward and horizontal cross sectional areas of 50 and 400 m^2, respectively. For the case when only hail regions are encountered the size of the hail at the 10^{-3} event level when flying in hail regions is ~100 mm for all temperature ranges and at the 10^{-5} event level it is ~120 mm. On the ground the worst case size of hail at the 10^{-3} event level is ~110 mm. Spacings between strikes for 10 mm particles is of the order of 10 cm for a traverse of 5 km region of hail. For hail larger than 70 mm collisions are likely to be single particle strikes. The results from the radar based approach are sensitive to the assumptions used to convert radar reflectivity to hail size distribution. This study has used assumptions that err on the side of caution and will bias the results towards larger hail sizes. We have not stated estimates here at the 10^{-9} event level because of the large extrapolations required.

Although hail impact has been recognised as a serious problem since the early fifties, recent studies concerning the consequences of hail impact on aircraft structures are somewhat rare. Thus the GARTEUR Group (AG30) has been undertaking a number of fundamental tests to gain a greater understanding of the mechanical properties of ice at different temperatures and the behaviour of ice under impact to more closely define the threat it poses to aircraft. Evidence shows that ice exhibits a clear strain rate effect behaving in a ductile manner at low strain rates whereas at higher strain rates the mechanical behaviour becomes much more brittle. The temperature of the ice during the impact event is critical. In addition a range of ice impact tests have been performed on both carbon and glass composite panels to determine the type (modes) and extent of damage that is generated. Composites are particularly susceptible to damage when loaded out-of-plane (i.e. in a direction perpendicular to the laminate), such as in the case of ice impacts, and often the damage sustained is barely visible, existing in the form of subsurface matrix cracks, back face fibre failure and delaminations between the different plies. In carrying out these tests the group has been able to develop new test procedures to help ensure adequate quality, consistency and repeatability in the ice projectile is attained.

2 Background

The next generation of aircraft are making extensive use of composite structures in exposed applications. It is necessary that the use of such material does not reduce the level of safety historically provided by the use of conventional materials such as metals. The behaviour of composites may be significantly different to metallic structures and damage such as delamination may be difficult to detect in composite structures.

Blunt impacts to composite structures from hail are of concern. The extent of the damage caused will be a complex function of the properties of the impactor and the different types of composite structure that are employed. While there have been many examples of extensive hail damage to composite structures the significance of such damage has been limited due to the use of such materials in less critical structural applications. Historically the hail threat has not been important in metallic structural applications and so only threats considered to be significant to conventional structural material behaviour such as bird strike have been considered. Standards dealing with threats like hail that were not thought to be significant for metal structures have been less well defined. Because of the growing extensive use of composites in aircraft structures it is necessary to define and understand the hail threat so that standards can be developed.

3 Aims and Objectives

Two strands were proposed for this work. The first was meteorological. The goals of that work were to review the existing literature of global hail threat data and develop a 2d and 3d climatology of hail. The second strand was concerned with aircraft structures. The aims of that part of the study were to review the existing regulatory frameworks with reference to hail threat and work with the aircraft manufacturers and FAA to understand how the threat varies across the aircraft for different materials. The final original goal of the project was to produce a global hail threat model that would combine the meteorological data with the aircraft structures information to form the basis of a hail threat standard. Together, the meteorological and aviation information contained in this study should act as a foundation for the development of a hail threat standard.

4 Meteorological Component: Literature Review

4.1 Properties of hail and graupel

4.1.1 Formation of graupel and hail

Formation mechanisms are summarised in List (1985) and Knight and Knight (2001), and references therein. Hailstones are lumps of ice/water/air mixture with sizes greater than 5mm that are generally opaque with layered structure. For sizes between 5-10mm they generally appear spherical or conical. 10-20mm sized hailstones tend to be ellipsoidal or conical. Larger 10-50mm hailstones take on ellipsoidal shapes with lobes, while still larger hailstones between 40-100mm appear irregular (including disk shapes) with protuberances.

Hail and graupel form in the updrafts of convective storms at temperatures colder than the freezing point of water. There are two main routes to the formation of hail but both proceed through the accretion of supercooled liquid droplets. It is easier to understand the growth of hail by considering the evolution in an air-relative frame. In this frame the cloud droplets are essentially stationary and collectors fall through the field of droplets. One route is for an ice crystal or aggregate of ice crystals to act as the collector and fall through the droplet field and rime by collecting droplets that freeze, increasing the mass of the particle, its fallspeed and rate of droplet collection. The latent heating effect of the droplets freezing determine if the growth will be 'dry' or 'wet'. If the growing particle is able to lose heat to the atmosphere faster through diffusion than latent heat is released from droplet freezing then the surface will be ice, colder than 0C and the layers will build up containing many air bubbles - 'dry' growth. If the latent heat is released faster than it can be diffused away from the particle then the liquid water will exist on the surface, air can escape and ice will build up with few air bubbles included - 'wet' growth.

Early on in the accretion process the accretion is generally through the dry growth mode leading to the formation of graupel. Graupel appears as white, opaque and conical (sometimes irregular) pellets with sizes up to 5 mm. If the graupel is exposed to more supercooled liquid it will continue to grow into a hailstone. By convention (AMS glossary) the transition to hail occurs when graupel particles exceed 5 mm. The formation of the graupel can be thought of as the generation of a hailstone embryo. The other common embryo for hailstone formation is a frozen rain drop which acts as the collector falling through the supercooled droplets. The creation of the embryos either through graupel formation of raindrop formation followed by freezing takes about 15 minutes. Growth of the hailstone then proceeds by further accretion of supercooled liquid droplets. The alternation of different growth modes can give rise to a layered shell structure. This used to be thought to indicate that hail forms by undergoing several excursions between warm and cold temperatures, but hailstone trajectories are now thought to be mainly simple up-down arcs with most of the mass growth taking place between -10C and -20C and the layering represents differences in icing conditions

encountered: supercooled liquid water content, temperature and relative speed of the collector. Growth from 1 mm to 2cm takes about 30 minutes (Knight et al. 1982)

Figure 4.1 summarises the formation of hail and also indicates feedback processes that can lead to the development of further hail embryos. During wet growth liquid water can be shed from the surface of the hailstone producing raindrops that can subsequently freeze. Collisions between hail/graupel with supercooled droplets can lead to freeze-splintering that generates more ice crystals.

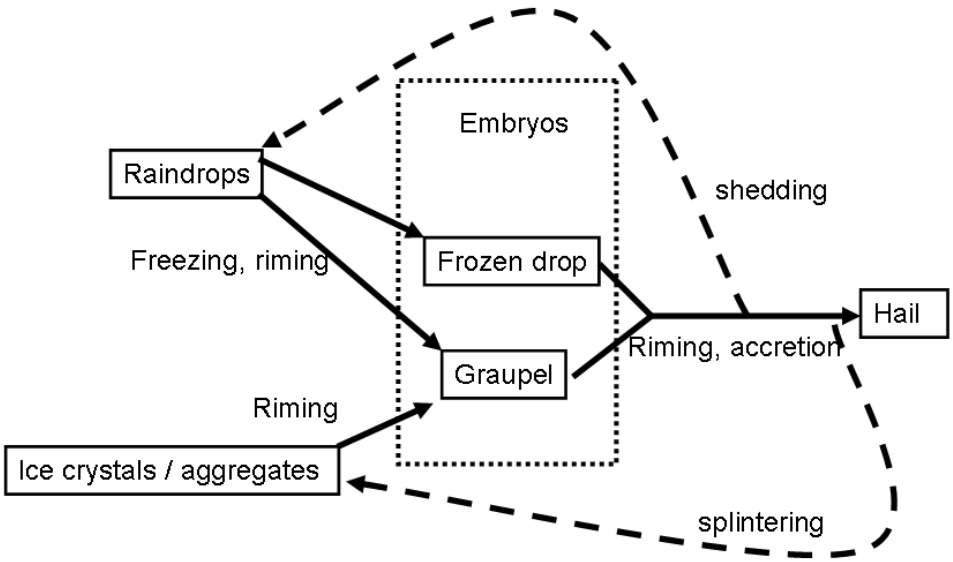

Figure 4.1 Schematic representation of the production of hail. Boxes represent hydrometeor types. Arrows represent conversion processes. Dashed arrows represent processes that can feed back on the production of hail.

4.1.2 Density

Actual measurements of graupel and hail density vary considerably. Figure 4.2 indicates the ranges of experimentally determined densities and particle sizes given in table 1. It can be seen that for sizes smaller than 20 mm there is a considerable range of densities from 50 to 890 kg m^{-3}. For larger sizes the density measurements tend to indicate high densities of 810 to 915 kg m^{-3} (density of solid ice is 917 kg m^{-3}). The lower density particles are likely to be quite fragile.

The density of graupel and hail is dependent upon the conditions under which supercooled droplets are accreted and how long the exposure is to different conditions. Macklin (1962) showed from experimental data that the density of accreted ice increases with the product of droplet size, r, and impact velocity, V_0, and decreases with the amount of supercooling of the collector surface, T_s. Macklin and others (e.g. Pflaum and Pruppacher, 1979, Castellano 2002) have been able to parametrize the density of ice accretions, ρ_{acc} ,

with a power law of the form $\rho_{acc} = \eta X^{\theta}$ where X is the parameter $-r \cdot V_0 / T_s$ and η and θ are positive constants. It can be seen that as a hailstone evolves it will grow more massive, increasing V_0 and descend to warmer temperatures (reducing T_s) so that the density of the ice accreted on the hail, and hence the mean density of the hail, will increase. Evidence in support of this was found by Prodi (1970). Because of the dependence upon these environmental conditions, there will be considerable variation in the density of graupel and hail as a function of size.

Various authors have used parametrizations based on the Maklin (1962) results to predict hail characteristics as they evolve. Rasmussen and Heymsfield (1987) show results from ensembles of hail evolving in 3D wind fields. Their results indicate bulk densities of 750±200kg m^{-3} for 5mm hail rising to 920±10 kg m^{-3} beyond 25mm. These modelling results are in broad agreement with the picture that graupel and small hail smaller than ~20mm vary widely in density, but tend towards a value close to the density of solid ice as the particles exceed ~20mm. Cloud modellers have tended to adopt a density of 400 kg m^{-3} for graupel (e.g. Ferrier et al 1995, Thompson 2004) and 917 kg m^{-3} for hail (e.g. Lin et al. 1983, Ferrier et al 1995).

In the light of the evidence it seems reasonable to assume a worst case density of solid ice (917 kg m^{-3}) for hail.

size range [mm]	density range [kg m^{-3}]	reference
0.5 3.0	50 450	Locatelli & Hobbs (1974)
0.5 1.0	450 700	Zikamunda and Vali (1972)
1.0 2.0	250 450	Zikamunda and Vali (1972)
0.4 3.0	80 350	Bashkirova and Pershina (1964)
0.5 3.0	850 890	Braham (1963)
0.5 6.0	500 700	List (1985)
0.8 3.0	130 130	Magono (1953)
8.0 19.0	310 610	Knight and Heymsfield (1983)
1.0 7.0	200 700	Heymsfield 1978
26.0 36.0	834 856	Prodi (1970)
11.0 31.0	810 900	Vittori and Di Caporiacco 1959
9.0 39.0	870 915	Macklin et al. 1960

Table 1 Experimentally determined densities of graupel and hail (hail: sizes>5 mm) and size ranges.

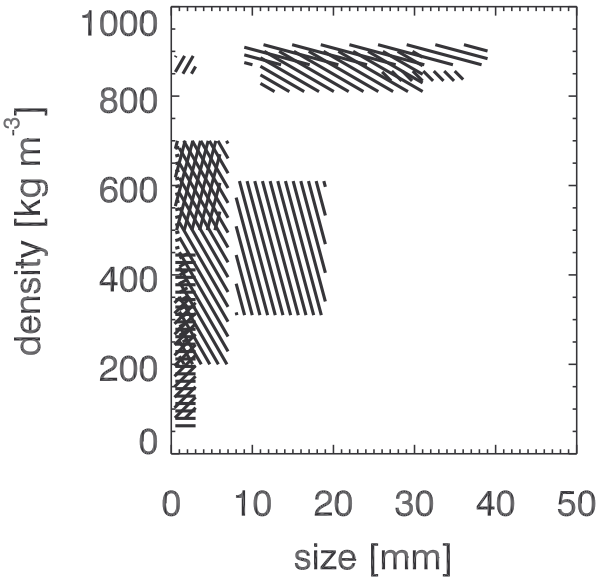

Figure 4.2 Experimentally determined densities for graupel and hail given in table 1.

4.1.3 Fallspeed for graupel and hail

The terminal fallspeed, V, for a sphere is

$$V = \left(\frac{4 g \rho_{hail} D}{3 C_d \rho_{air}} \right)^{\frac{1}{2}} \tag{4.1}$$

where g is the acceleration due to gravity, ρ_{hail} is the density of the graupel or hail, D is the size of the hail or graupel, C_d is the drag coefficient and ρ_{air} is the air density. Hence, the fallspeed increases with hail/graupel density and size, but decreases with increasing drag coefficient and air density.

Empirical relations between fallspeed and size have been determined by a number of authors. These relations require a density correction to be used outside of the environmental conditions under which they were sampled. Within the literature different definitions have been used for the particle size. Some studies use the maximum dimension or span of the particle to represent D, whereas others use an equivalent diameter based on the size of an equivalent ice sphere that has the same mass. Different definitions will lead to variability in results quoted in the literature, but we will not attempt to disentangle those assumptions here. Instead we note that measurements of shape ratio defined as the size of the maximum to minimum dimension for graupel and hail in the sizes ranging from 1 to in excess of 25 mm is about 0.8, with most

values typically lying between 0.6 and 1.0 (Matson and Huggins 1980, Barge and Isaac 1973, Heymsfield 1978). Therefore potential biases in sizing between different studies could be of the order of 20%.

Because the graupel and hail can be rough and nonspherical the drag coefficient can be varied to represent departures from a smooth sphere. The drag coefficient is a function of Reynolds number and for graupel and hail, Reynolds numbers (Re) exceed 100. Matson and Huggins (1980) and Castellano and Nasello (1997) summarise drag coefficients from previous work. These results show a gradual decrease in Cd from 0.5-4 for Re=100 to 0.3-2 for Re=10,000. A value of 0.6 is often adopted for hail work (Morgan 1982), although higher values may be more appropriate in the mean.

Figure 4.3 shows terminal fallspeeds for a number of studies and eq. 4.1 for a range of drag coefficients for conditions -4.5C at 700mb. The grey swath depicts fallspeeds using equation 4.1 assuming hail densities of 917 kg m^{-3} and drag coefficients ranging from 0.5 (greatest fallspeeds) to 1.5 (slowest fallspeeds). This range of drag coefficients encompasses the empirical relations. It can be seen that 10mm particles have fallspeeds in the range of 9-17m s^{-1} and 50 mm particles have fallspeeds in the range of 20-35 m s^{-1}. To obtain the actual fallspeed, aloft, relative to the ground the local updraft speed needs to be added. This will be highly variable and can lead to hail with significant fallspeeds being lifted higher, or alternatively, hail located in downdrafts will fall much faster relative to the ground. Updrafts and downdrafts can be of the order of 10 m s^{-1} in thunderstorms.

To be conservative, a worst case estimate of hail fallspeed is given by assuming a hail density of 917 kg m^{-3}, and a drag coefficient of 0.5. Equation 4.1 then becomes $V(m/s) = \rho_{air}(kg/m^3)^{-1/2} 156\, D(m)^{1/2}$

Fallspeed, $V = \left(\frac{\rho_{ref}}{\rho_{air}}\right)^{0.5} aD^b$

Reference	size range [mm]	a	b	D units	V units	ρ_{ref} [kg m^{-3}]
Ferrier et al 1995 [+]	0 5	351.2	0.37	cm	cm/s	1.23
Ferrier et al 1995 [*]	0-	1094.3	0.64	cm	cm/s	1.23
Heymsfield and Kajikawa 1987 [◊]	0 5			m	m/s	1.23
Auer et al. (taken from Heymsfield 1978) [Δ]	0.5 20	0.95	0.911	mm	m/s	1.05
Lozowski and Beattie 1979 [□]	4 10	12.43	0.5	cm	m/s	1.23
Matson and Huggins 1980 [χ]	5 25	11.45	0.5	cm	m/s	0.993

Table 2 Empirical fallspeed relations. Appropriate units for the coefficients and reference air density are given. Symbols used in figure 4.3 are also shown.

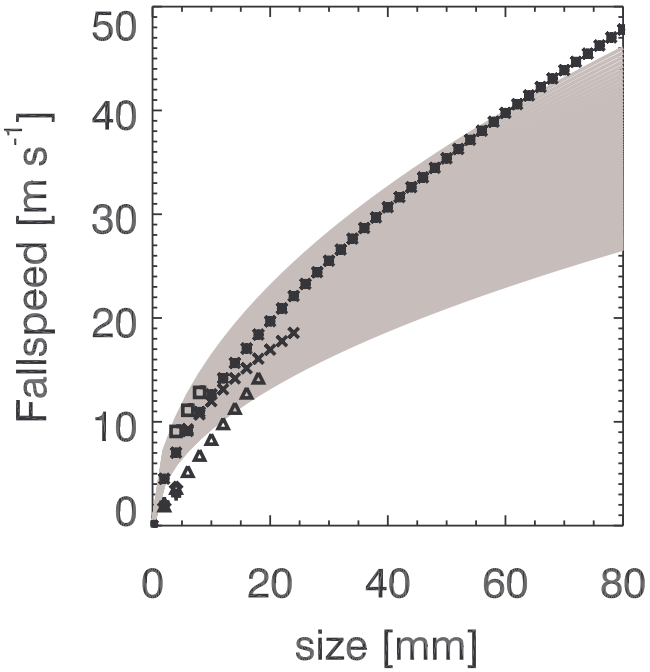

Figure 4.3 Fallspeeds of graupel and hail at -4.5C, 700 mb. The grey region indicates the range of fallspeedsgiven by eq. 1 for ρ_{hail}=917 kg m^{-3} and Cd varying from 0.5 (upper border of region) to 1.5 (lower border). Empirical fallspeed relations have been overplotted for these conditions (see table 2

4.2 Size distributions of graupel and hail

Observations using hailpads at the surface, foil impactors and optical array probes on aircraft (Ulbrich and Atlas, 1982; Cheng and English 1983; Federer and Waldvogel 1975, Spahn and Smith, 1976, Morgan,1982, Peterson et al. 1991 , Musil et al 1991) have indicated that the size distribution of hail is well approximated by an exponential function of the form:

$$n(D) = N_0 \exp(-\lambda D) \quad \text{[units: m}^{-4}\text{]} \qquad (4.2)$$

so that n(D)dD gives the number concentration of particles observed in the size range D to D+dD. This distribution shape has generally been determined from measurement methods sensitive to particles bigger than 5 mm in size. When smaller particles have been considered, an alternative power law form ($n(D)=aD^b$) for the distribution was suggested by Auer and Marwitz (1972) based on foil impactor data collected from aircraft. A study combining foil impactor observations with an optical array sensor that was sensitive to larger particles also indicated a power law behaviour in the size distribution. However, Musil et al. (1976) interpreted similar distributions as two separate exponential distributions with a cross over around 3 mm in

size. Particles smaller than 3 mm were presumably dominated by non-hail particles (e.g. raindrops, ice aggregates and graupel).

Airborne data were generally obtained between temperatures of -2 to -12C, hail water contents were below 3 g m^{-3} and concentrations less than 20 m^{-3} for particles larger than 5 mm were observed (Spahn and Smith 1976, Musil et al 1991). For surface observations the Cheng and English study encountered hail water contents smaller than 0.8 g m^{-3} and concentrations less than 4 m^{-3} for particles larger than 4mm. Slope parameter (λ) values for fitted exponential distributions have been found to vary from approximately 1.5-10cm^{-1} (Cheng and English, 1983 using subset of samples, Ulbrich and Atlas 1982, Federer and Waldvogel, 1975) and between 2-4cm^{-1} (Morgan and Summers 1985), whilst the exponential intercept values (N_0) have been found between 0.1 and 100 m^{-3} mm^{-1} (Cheng and English 1983, using subset of samples, Federer and Waldvogel 1975, Spahn and Smith 1976). Exponential distributions are obtained by averaging over time and space. Distributions formed from limited amounts of data can look like truncated distributions (Morgan and Summers, 1985) perhaps due to size sorting effects and/or statistical effects. Some useful relations for exponential distributions are given in the Appendix.

Useful correlations have been found between parameters describing the exponential distribution. Cheng and English (1983) found power law relations between N_0 and λ from surface hailpad data that allows the exponential function to be completely specified if the water content is known. Spahn and Smith (1976) used aircraft data to obtain relations between water content and parameters of the exponential distribution.

Modellers representing graupel and hail have tended to adopt the exponential distribution (Lin et al. 1983, Reisner et al. 1998, Ferrier et al. 1995, Morrison et al. 2005, Straka and Mansell 2005) with the intercept parameter set to $4x10^6$ m^{-4} following Federer and Waldvogel 1975, or in the range $1x10^3$-$4x10^5$ m^{-4} according the graupel or hail category (Straka and Mansell 2005). Other modellers have used gamma distributions ($N(D)=N_0D^v\exp(-\lambda D)$) to represent graupel/hail (Thompson et al. 2004, Milbrandt and Yau 2005). Thompson et al. (2004) uses a representation where N_0 and λ are interdependent and functions of graupel water content with a fixed shape parameter (v), whereas Milbrandt and Yau allow the shape parameter to vary as the distribution evolves.

Figure 4.4 shows the ranges of exponential distribution parameters (N_0 and λ) reported in the literature. There are more estimates available for the slope of the distribution (λ) than the intercept parameter (N_0) and these estimates have a consistent lower bound of 200 m^{-1}. This value is chosen to represent the worst case giving rise to the broadest distribution of hail.

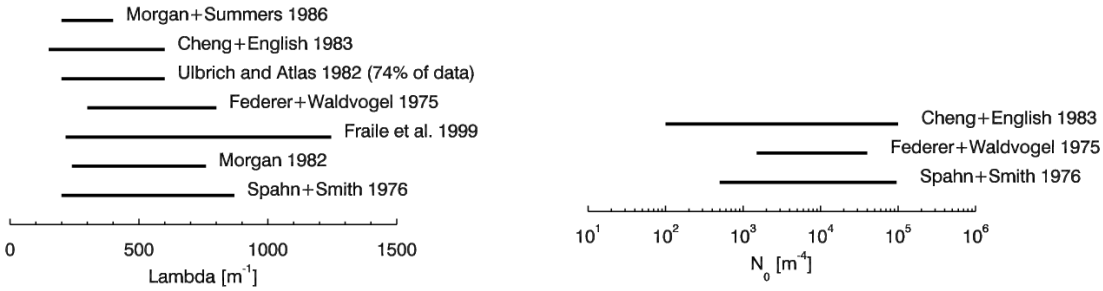

Figure 4.4 Range of measured parameters for exponential distributions describing hail distributions.

4.3 Vertical structure of hail/graupel profiles

The vertical distribution of graupel and hail is intimately related to the structure of thunderstorms that can be composed of so-called multi-cell and supercell components (Browning 1986) and also be embedded within mid-latitude frontal features. Although the definition of a convective cell is not well defined (Knight et al. 1982) the basic idea is that it represents the regions of convective activity within a thunderstorm, driving the microphysics that leads to the generation of graupel and hail.

Figure 4.5 and 4.6 show schematic cross sections of the radar structure of an idealised multi-cell and supercell storm at a mature stage in their development. Examining the storms at other times will reveal different structures and larger storms will be composed of elements of these at various stages of their lifecycle. The schematic diagrams reveal that the regions of intense radar reflectivity have a span of the order of 2 to 5 km.

The multi-cell storm contains cells at different stages in the lifecycle. The updraft drives the production of cloud droplets and ice particles. This leads to the production of graupel and the onset of strong radar echoes in the upper parts of the cloud. Further growth forming large precipitation particles and hail throughout the depth of the cloud eventually leads to a drag effect that can impede the convective activity. Evaporation of hydrometeors below the cloud cools the air and can create or enhance downdrafts. These events lead to the dissipation of the cell. All these stages can be present in a multi-cell storm as indicated in figure 4.5. The supercell is different to single cells in that it can have a long lived updraft and downdraft couplet existing adjacently that can drive the generation of large precipitation particles without destroying the updraft. Such systems are characterised by ‘vault’ regions where strong slanting updrafts drive the production of supercooled droplets but exclude larger precipitation particles leading to low radar returns. Production of graupel higher up in the cloud eventually falls out of the strong updraft and continues to grow into hail as it falls. The falling, and evaporating, precipitation will generate a downdraft that can reinforce the updraft at the front of the system. Such a dynamical setting can produce long lived storms characterised by a single cell. In reality circulations are more complex and three dimensional (see Browning for more details).

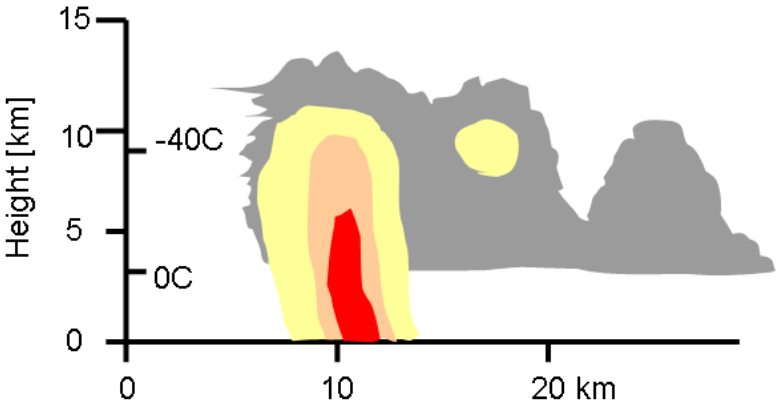

Figure 4.5 Schematic vertical cross-section of a multi-cell storm (Adapted from Browning 1986). The grey shading represents the cloud. The colour shading represents different levels of significant radar reflectivity (> 30dBZ) , increasing from yellow to red (in 10 dBZ steps).

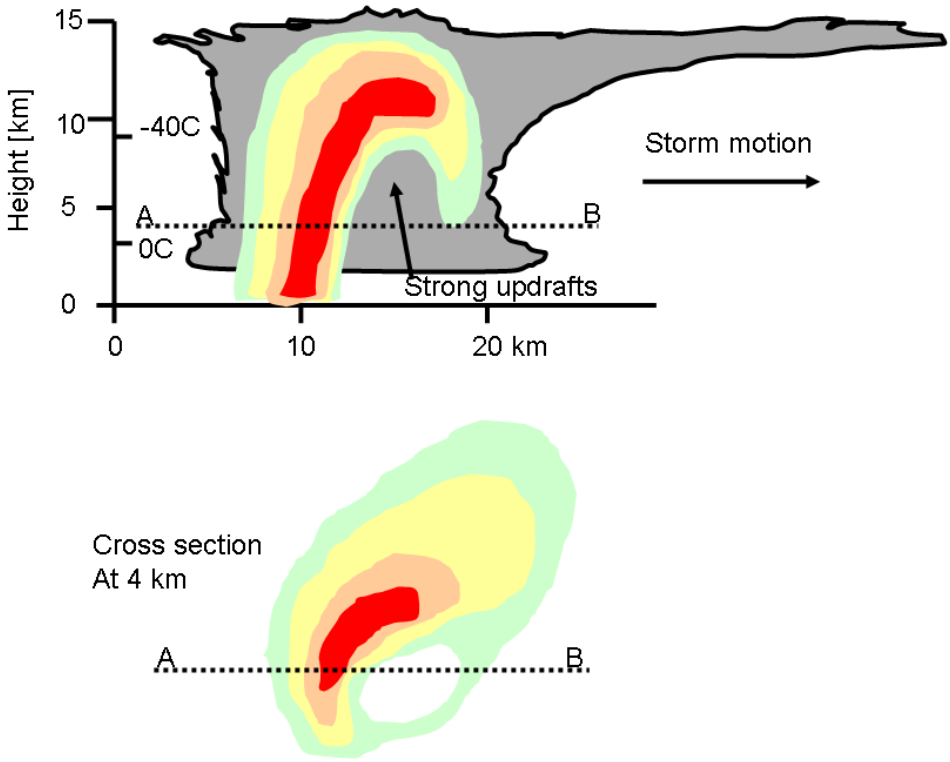

Figure 4.6 Schematic vertical and horizontal cross-sections of a supercell storm (Adapted from Knight et al. 1982). The grey shading represents the cloud. The colour shading represents different levels of significant radar reflectivity (>20dBZ), increasing from green to red (in 10 dBZ steps).

Vertical profiles of radar reflectivity provide the best way to infer the mass loading by precipitation sized particles in these systems. The schematic diagrams and case studies presented in Knight and Squires (1982) indicate that regions of high radar reflectivity and hence regions of graupel and hail can extend to

high altitudes (>10km). The TRMM (Tropical Rainfall Measurement Mission) satellite mission has produced the largest sampling of convective storms (Zipser et al. 2006). Of all the storms identified within 36deg of the equator, 0.1% have 40dBZ radar echoes extending to heights greater than 10km. The difficulty with using radar reflectivity is knowing how to attribute the signal to different types of particles. However, it seems clear that reflectivities exceeding 50 dBZ and above the freezing level are likely to contain graupel and hail (Straka et al. 2000). Liu et al. (2008) show joint histograms of maximum reflectivity versus height within structures identified as precipitation features or storms. These indicate that for a kilometre above the freezing level (~5 km in the tropics) the fraction of precipitation features with radar reflectivities exceeding 50 dBZ is less than 10% over land, whereas over the oceans is an order of magnitude or more smaller. There is a tendency for radar reflectivity to increase downwards through the cloud. Although this will result for a range of reasons it seems plausible to expect hail water content to be also increase towards cloud base.

4.4 Existing hail Climatologies

4.4.1 Introduction

Hail has traditionally been most commonly recorded through human observation. That is, collecting stones, categorizing and measuring them. However, in the last 30 years, automatic systems using hailpads have become more common. Hailpads consist of a square piece (often circa 30 cm x 30 cm) of styrofoam material about 25 mm thick, mounted in an aluminium bracket on the top of a post about 1.5 m above the ground. The hailpad exposure surface is sometimes lightly painted with a white paint to prevent disintegration by ultraviolet rays of sunlight. Falling hail hits the exposed surface of the styrofoam leaving permanent dents which can then be analyzed either by eye or using digital imaging techniques. Errors such as bird pecks, scattering and bouncing of hail tend to be minimized through sampling large numbers of hailstones, and therefore hailpads are seen as the most up to date successful sampling scheme to employ in large areas at a reasonable cost and sufficient density for objective recording of hailfalls. Hailpad data can provide size distributions and concentration of hailstones from which the hail kinetic energy and other parameters can be calculated, Long (1980).

4.4.2 Geographical and seasonal distribution

4.4.2.1 General

Hail forms in strong thunderstorms, particularly those with intense updraughts, high liquid water content, great vertical extent, large water droplets, and where a good portion of the cloud layer is below freezing. The growth rate is maximized at about −12 ℃, and b ecomes vanishingly small below −30 ℃ as at those

temperatures supercooled water droplets become rare. For this reason, hail is most common in mid-latitudes during Spring and early Summer where surface temperatures are warm enough to promote the instability associated with strong thunderstorms, but the upper atmosphere is still cool enough to support ice. For example, see Schuster et al (2005) and Zhang et al (2008), Accordingly, hail at the surface is less common in the tropics despite a much higher frequency there of thunderstorms than in the mid-latitudes. This is because the atmosphere over the tropics tends to be warmer over a much greater depth. However, hail does occur regularly throughout the year in the tropics. Entrainment of dry air into thunderstorms over continents can increase the frequency of hail by encouraging evaporative cooling which lowers the freezing level in thunderstorm clouds giving hail a larger volume to grow in.

Hail is also much more common along and near mountain ranges because mountains force horizontal winds upwards (through a process known as orographic lifting), thereby intensifying the updraughts within thunderstorms and making hail more likely. Deflection of airflows resulting in convergence and ascent of volumes of air is also another important mechanism for increasing the strength of updraughts. One of the most notorious regions for large hail is the mountainous area of northern India and Bangladesh (Frisby and Sansom, 1967), which have reported more hail-related deaths than anywhere else in the world and also some of the largest hailstones ever measured. Other topographical (mountain) effects have been observed, for example, in the central Tibetan plateau (Zhang et al., 2008), SW France and the Alps (Vinet, 2001) and the Pyrenees (Fraile, 2003).

Many countries are establishing local climatologies, however, the difficulty with hail is that it is a very localised phenomenon on the global scale and information has to come from a variety of sources, including the general populace. This means that location maps can often be biased to regions where there is enough human activity to provide reports. Court and Griffith (1986) reproduce a global composite of hail days based on earlier reports. This is reproduced in figure 4.7 and shows higher values over mountainous regions. However, there are likely to be large data voids where population densities are low or reporting was incomplete.

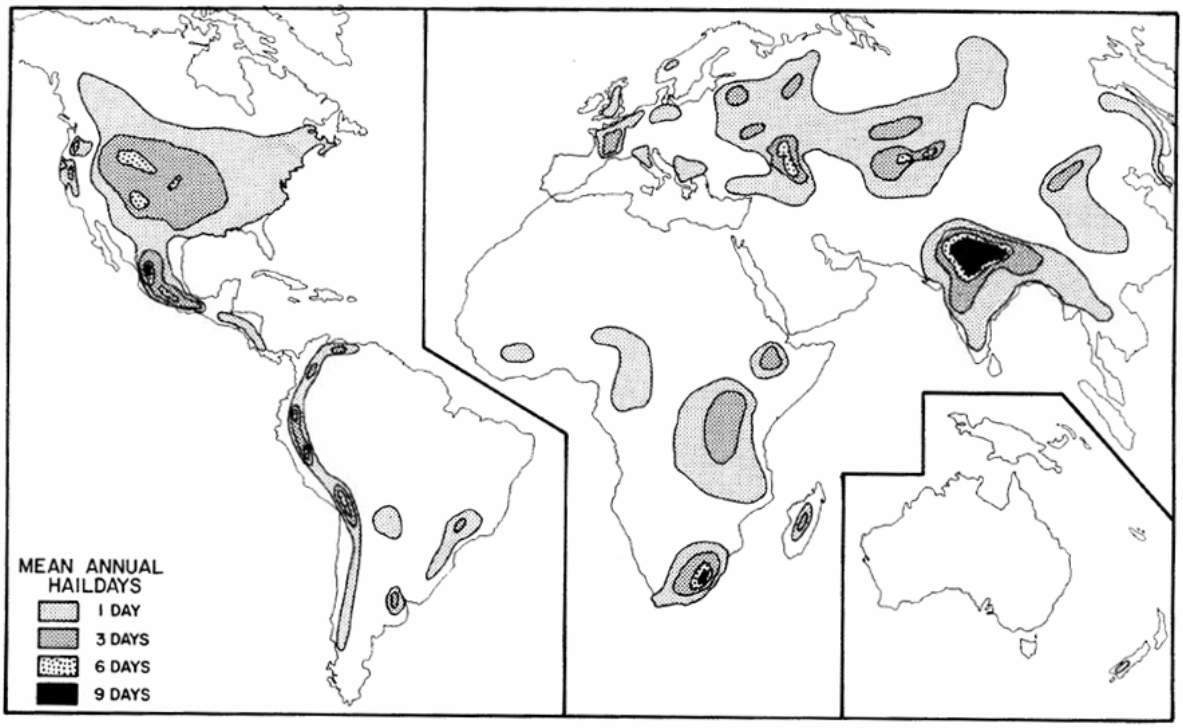

Figure 4.7 World composite of hail days reproduced from Court and Griffith (1986).

Brief summaries of documented hail distributions in parts of the globe now follow.

4.4.2.2 Australia – New South Wales

Figure 4.8 shows the number of hailstorms and 'hail days' observed in New South Wales (Australia) during the period 1791 to 2003. Hailstorms are separate thunderstorms producing hail whereas a 'hail day' is observed if hail falls at any time during the day regardless of whether it came from one storm or many.

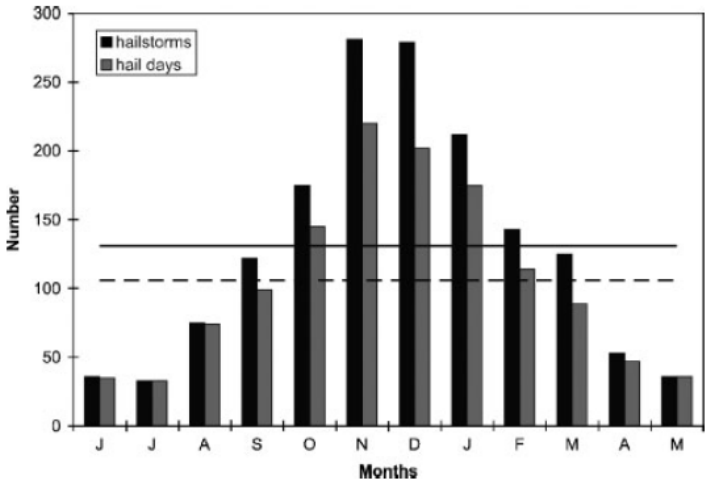

Figure 4.8 Total number of hailstorms and hail days (see text) occurring in each month in New South Wales (NSW) from 1791 to 2003. The solid line is the monthly average number of hailstorms and the dashed line is the monthly average number of hail days (reproduced from Schuster et al, 2005).

This long series of hail data shows a nice symmetric distribution centred on late Spring (November), clearly demonstrating that, although there is a risk of hail at any time of the year in NSW it is during late Spring and early Summer that the risk is greatest. Clearly some hail days outside the winter period also comprise of two or more separate hailstorms indicating that the daily risk will vary more during the warm season.

4.4.2.3 Canada

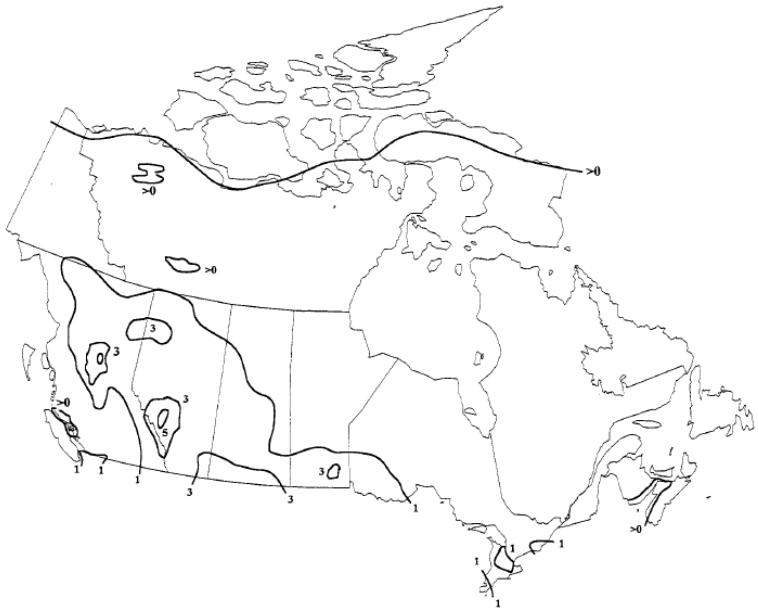

Figure 4.9 Average number of hail days per year based on 1951-1980 May to September data. (Reproduced from Etkin and Brun, 1999).

Figure 4.9 clearly shows that the incidence of hail increases the closer one gets to the Rockies. The period May to September was chosen in order to filter out reports of graupel being classed as hail during the cold season.

4.4.2.4 China

The influence of orography on the incidence of hail is clearly demonstrated in Figure 4.10. The average annual frequency of hail days can be seen to increase steeply around the Himalayas.

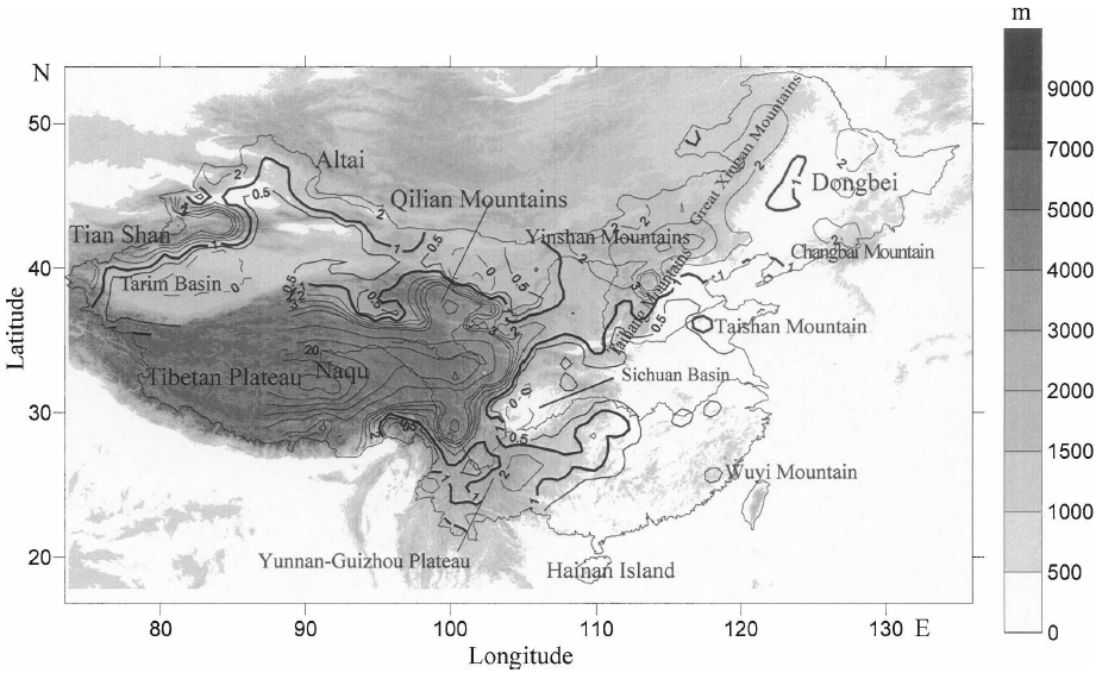

Figure 4.10 Mean annual hail day frequency in China 1961-2005. (Reproduced from Zhang et al., 2008).

4.4.2.5 Finland

Although Finland has a cold climate and a low population density, (approximately 16 persons in each km² on average), large hail (≥ 2 cm in diameter) is observed every year mainly as a consequence of the damage it causes. A map showing cases of large hail in Finland in the period 1930-2006 is presented in Figure 4.11.

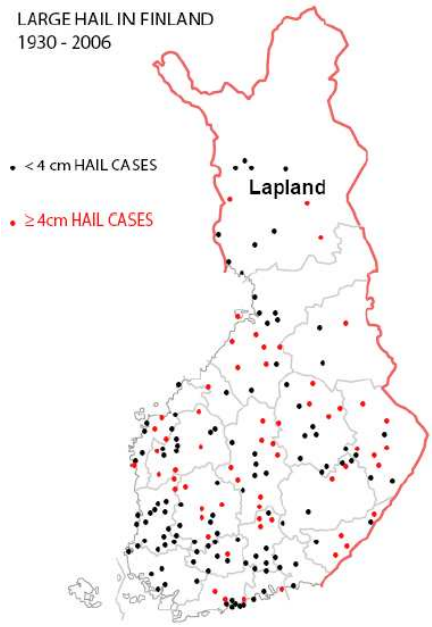

Figure 4.11 The geographical distribution of large hail cases in Finland (reproduced from Tuovinen et al., 2006). The black dots indicate under 4 cm and greater than 2 cm diameter hailstone cases and the red 4 cm or larger. The red line is a land border with Russia, Norway and Sweden; in the south and southwest, Finland is surrounded by sea.

This figure is interesting in that it shows a fairly uniform distribution of large hail cases in the 75 year period tending to get more sparse as one goes north that could be correlated with decreasing population density.

Figure 4.12 shows that most of the large hail cases occur during the Summer and none after September or before May. Large hail is rare though in Finland. In the second half of July, 71 cases of large hail were observed in Finland during the period giving an average frequency of just under 1 per year in the whole country.

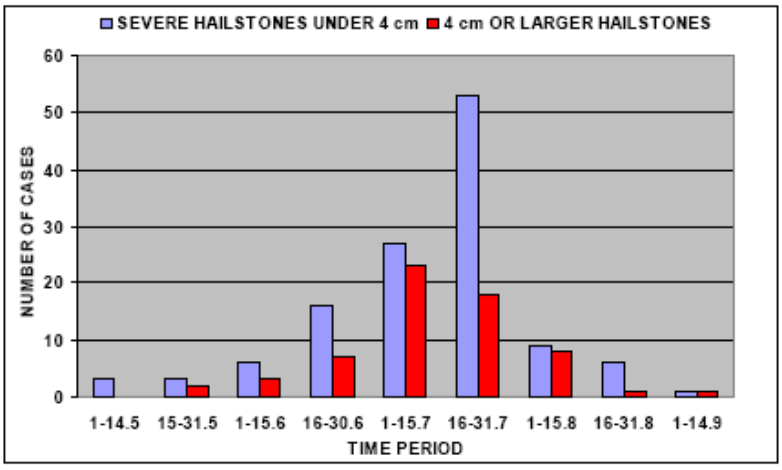

Figure 4.12 Monthly distribution of large hail cases in Finland 1930-2006. Every month has been divided in two, starting from May and ending to mid-September. Blue bars indicate severe hail-stones under 4 cm and red bars 4 cm or larger hailstones. (Reproduced from Tuovinen et al., 2006).

4.4.2.6 Europe

The European Severe Storms Laboratory (ESSL) started as an informal network of European scientists in 2002 seeking to record and study severe weather events throughout Europe. The ESSL is now a non-profit research organisation. One aim of the organisation is to provide a hail climatology for Europe. A start has been made and a composite preliminary climatology is shown in Figure 4.13

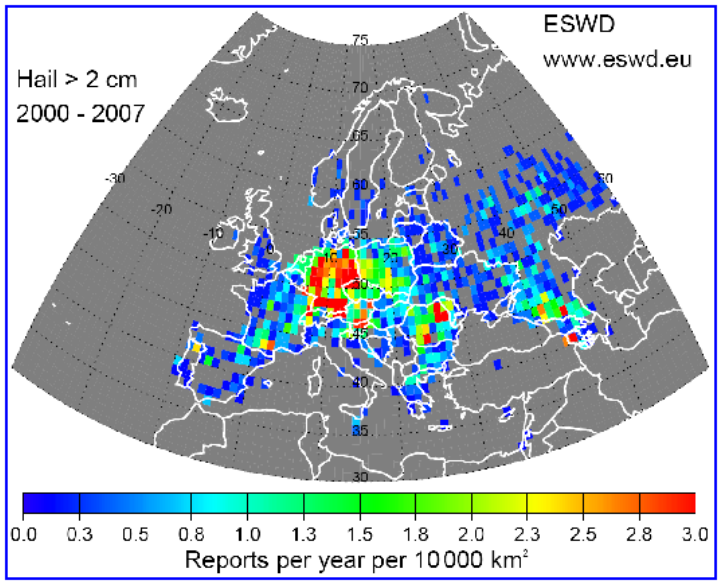

Figure 4.13 Preliminary climatology of large hail (> 2cm) over Europe showing average number of reports per year per 10000 km^2 in the period 2000-2007. (Reproduced from http://www.essl.org/research/).

Unfortunately this map is biased by a very dense observing network over Germany prior to 2005. nevertheless some interesting signals are beginning to emerge. For example, peaks in frequency near the Pyrenees and over the Alps and a rapid decrease in frequency north of 60N.

4.4.2.7 Greece (reproduced from Sioutas, Meaden and Webb, 2008)

The authors write: " Data from weather stations of the Hellenic National Meteorological Service (HNMS) indicated a mean yearly point frequency varying between 1 and 2 hail days for Central Macedonia. Crop insurance data from the Hellenic National Agricultural Insurance Organization (ELGA) showed a mean regional frequency of 22.3 hail days for the total cultivated area of Central Macedonia, about 6,500 km^2, for the warm season, from April to September. Hailpad data representing almost one third of the total cultivated area of Central Macedonia, indicated a regional average of 8 hail days and 45 hailpads recording hail for the warm season. Spatial analysis over the hailpad area (Figure 4.14) revealed a large variability of hail

occurrence, with local maxima at the higher altitude and close to mountain barrier areas and a decreasing frequency over areas closer to the sea. ”

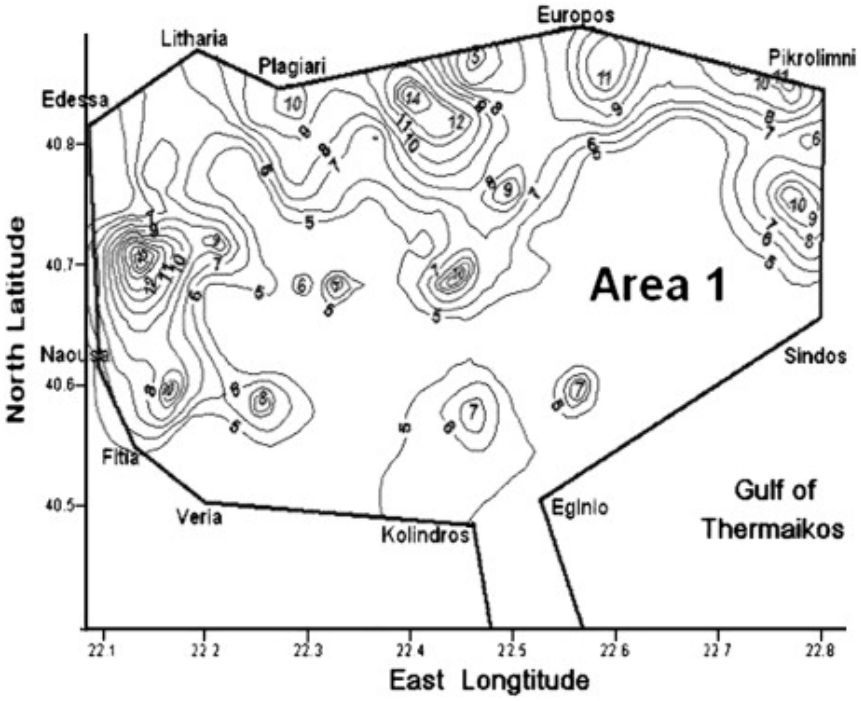

Figure 4.14 Total number of hailfalls at each hailpad site location for 17 seasons of the hailpad network operation, within the period 1984–2004. (Reproduced from Sioutas et al., 2008).

The figure of 6500 km^2 will represent a typical operating area for larger airports in varying terrain. It illustrates how highly variable in space the risk of hail may be as aircraft land and take-off. The figure also shows that there may be ‘preferred’ areas for hail falls which is encouraging for future assessments of risk etc.

4.4.2.8 USA

A range of hail incidence maps are publicly available from the National Severe Storms Laboratory (NSSL) in the States at http://www.nssl.noaa.gov/hazard/totalthreat.html .

Figure 4.15 shows the average number of hail days per year during 1980-1999. The map is for hail greater than 0.75 inches in diameter (~2 cm) and gives the mean number of days per year with one or more events within 25 miles of a point.

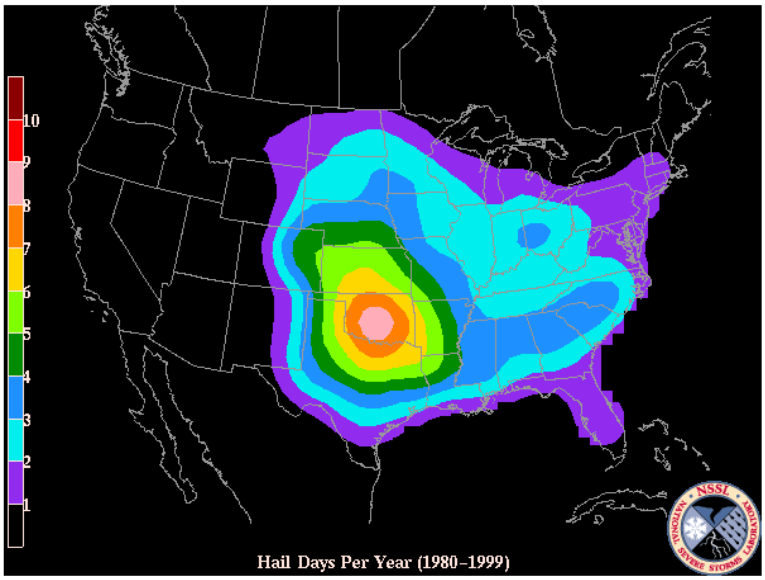

Figure 4.15 Hail days per year (1980-1999) from NSSL, (see text for details).

Large hail (> 0.75 inch diameter) hazard maps for specific locations in the USA are also available as a clickable map from http://www.nssl.noaa.gov/hazard/hazardmap.html as a function of time throughout the year (fig. 4.16).

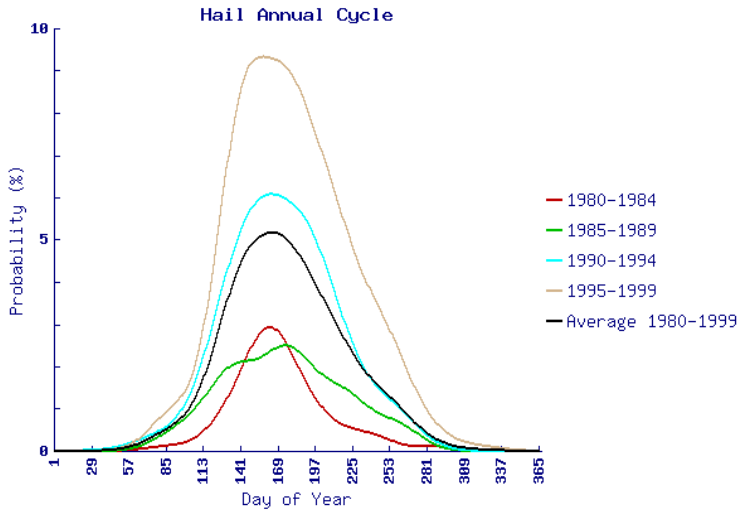

Figure 4.16 Example of a point hail climatology from NSSL according to day of year.

Changnon (1999) states that hail damage to property is very serious in the USA. In 1997 money terms the average annual loss during the 1990s was estimated at $1.2 billion. In their paper a hail risk map was prepared taking into account expected hail frequency and intensity. This is an interesting approach and may be worthy of further study. The map is reproduced as Figure 4.17.

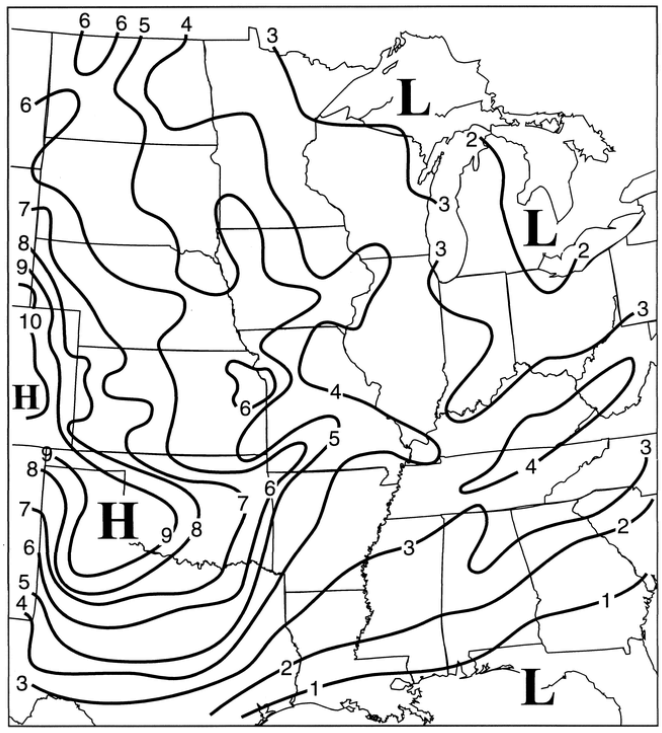

Figure 4.17 A hail risk pattern for property in the USA based on indices determined by combining point data on average hail day values and average hailstone size. The value of 1 is the lowest risk. These data are based on hail records for the period 1901-1996. (Reproduced from Changnon, 1999).

4.4.2.9 Tropics

Some good information on the distribution of hail in the tropics is available in Frisby and Sansom (1967). The authors detail average incidences of hail at specific places as well as over large geographical areas as shown in Figure 4.18.

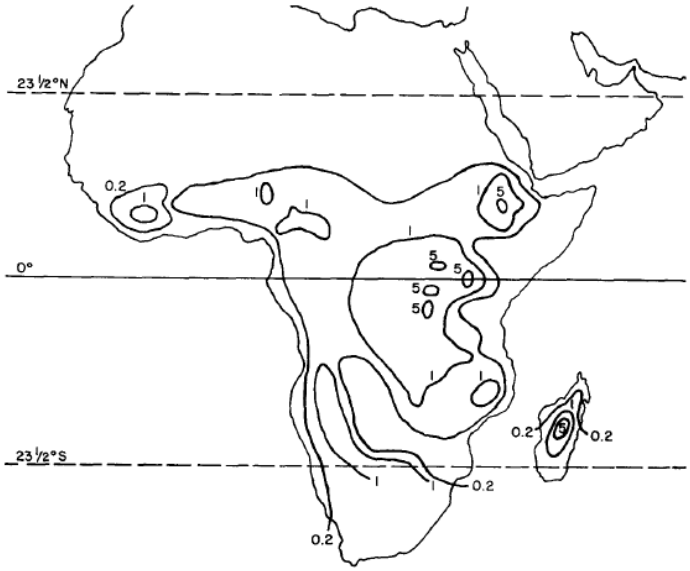

Figure 4.18 Mean annual frequency of hail over Africa (10 year record).

The larger values coincide with topographical features.

4.4.2.10 United Kingdom

Webb, Elsom and Meaden (2009) studied large hail (>1.5 cm diameter) events during the period 1930 to 2004. The geographical distribution of hailstorms in the British Isles shows that the highest frequency of significant, damaging hail storms (over 1.5 cm diameter) is in central and eastern England, with the East Midlands, East Anglia and the lower Thames Valley (including Heathrow) most conspicuous when the incidences are mapped (Figure 4.19).

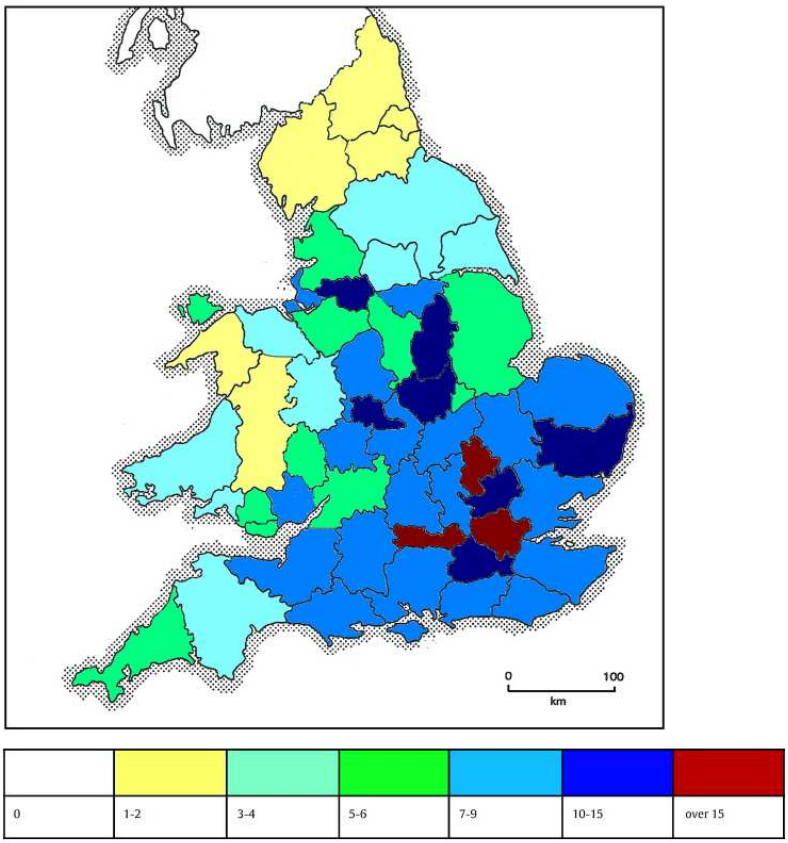

Figure 4.19 Number of hailstorms (per 1000 km^2 per 100 years) containing hail reaching or exceeding 1.5 cm diameter, for counties of England and Wales, 1930-2004. (reproduced from Webb et al., 2009).

Over Scotland the number is less than 3, apart from the Edinburgh area where it is in the range 3-4. It is interesting to note that the incidence of hailstorms correlates quite well with the areas in the map showing the average number of days of thunder in the British Isles (Figure 4.20). This is not too surprising, however, since hailstorms occur in the same type of clouds that produce thunderstorms.

Figure 4.20 Mean number of days of thunder in the British Isles(1971-2000).Key ■ 15–19 days ■10–14 days ■5–9 days □ under 5 days. (From Webb et al., 2009).

The monthly distribution of hailstorms with hail greater than 1.5 cm diameter is shown in Figure 4.21 and confirms the late Spring/early Summer maximum seen in other climatologies.

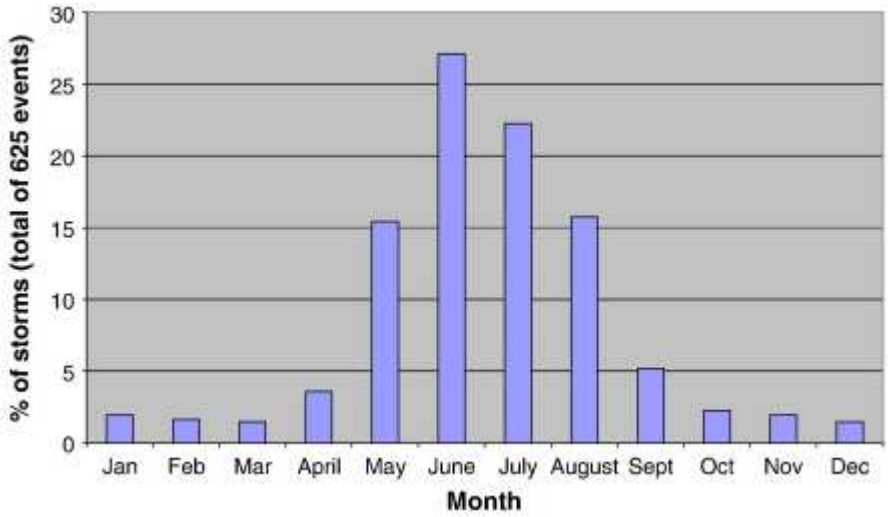

Figure 4.21 Monthly percentage distribution of hail storms with hail diameter greater than 1.5 cm over the British Isles in the period 1930-2004. (From Webb et al., 2009).

4.4.3 Long term frequency

Great care has to be taken in interpreting recent trends in the incidence of hail. As public awareness increases and with better communication technology, such as mobile phones, in recent years; the incidence of hailfalls may appear to rise as a consequence. A good example of this is TorDACH (http://www.tordach.org/de/hail.htm). TorDACH, founded in 1997, is a network of more than 30 scientists from different fields and laymen who collect information on severe weather, including hail, in Germany, Austria and Switzerland. The current climatology is shown in Figure 4.22.

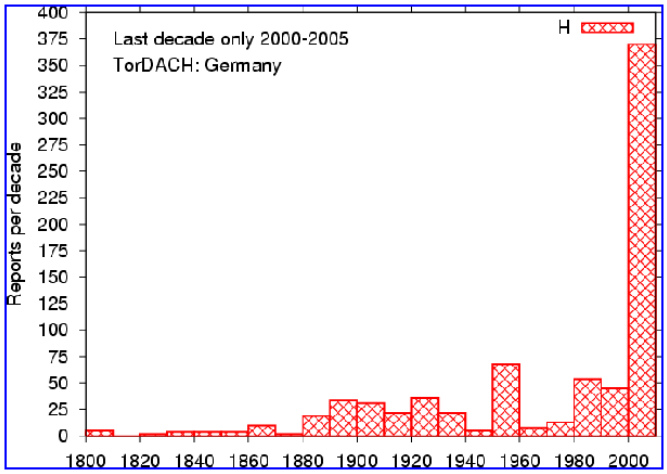

Figure 4.22 Number of reports of large hail (> 2 cm) in Germany, Austria and Switzerland for each decade from 1800 to 2005.

It is extremely unlikely that the huge rise in the number of reports in the first decade of the 21st Century reflects a real increase in the incidence of large hail as opposed to a greater awareness of and opportunity to report such events.

Schuster et al (2005) describe a climatology for New South Wales in Australia from 1791 to 2003. Over the study period, a total of 1570 thunderstorms produced hail. On average, 10 hailstorms per year were recorded in Sydney in the last 50 years. However, there is a statistically significant decrease in the hailstorm frequency during the last 14 years compared with the preceding 36 years.

Another interesting long term climatology is available from Finland (Tuovinen et al, 2006). The number of days with large hail (> 2 cm diameter) during the 1940's is small due to the war years. In recent years, there has been some increase in the number of cases and large hail days. This is presumed to be mostly due to more widespread interest in severe weather events among the general public and more systematic collecting of reports.

These examples illustrate that the reported frequency of hail is very variable and that the number of reports can be influenced by human activity. There is no clear signal for a change in hail frequency over the decades.

4.4.4 Diurnal distribution

Generally hail falls during the afternoon and evening periods with peaks of intensity between 14 and 20 hours local time (LT). However, in parts of China hail has often been observed overnight (Zhang et al. , 2008). The morning is the period when hail falls are least likely.

There are more local variations on this theme. Dessens (1986) and Gaiotti et al. (2003), in south-west France and Northern Italy respectively, noted that hailstorms peaked around 16 UTC, but that the proportion of overnight events increased later in the season (i.e. July to September). In New Zealand, Steiner (1989) noted that the general peak time for damaging hailstorms was between 12 and 18 hours LT, except along the western coastal strip of the South Island which both experienced a winter storm maxima and peak occurrence from 00 to 06 hours LT. In the UK, Webb et al. (2008) showed that the peak time for hail storms with diameters greater than 3 cm was between 15 and 18 hours LT, see Figure 4.23

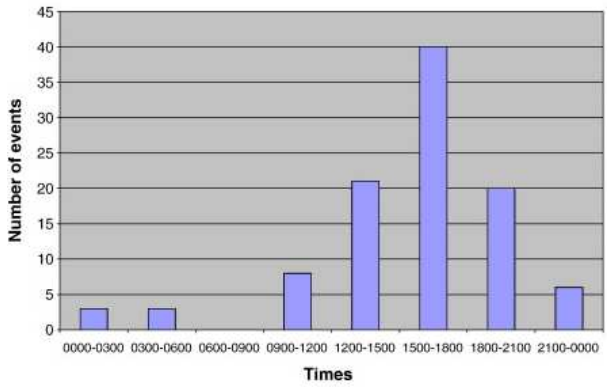

Figure 4.23 Number of hail storms occurring between the years 1800 and 2004 with hail diameters greater than 3 cm according to 3 hourly time-of-day periods. (From Webb et al., 2008).

4.4.5 Hail swath characteristics

In the 1986 paper by Dessens a study of the mean characteristics of 30 of the most severe storms which have caused damage in Aquitaine (France) in the period 1950-1980 showed that a typical long-traveling hailstorm moves at 15 m s^{-1} for 1.5 h, dropping a hail strip 86 km long and 6 km wide.

Tracks have also been studied in the UK by Webb et al. (2008). Here the authors report that " between 1800 and 2004, path lengths are known for 120 of the 156 hailstorms in Great Britain of intensity H4–5 (30-50 mm hail) upwards. Of these 120 events, 66% cases had swath lengths of 20 km or more and 87% of these hailstorms had swath lengths of 10 km or more. Since 1800, all but three of the 41 hailstorms of intensity H5–6 (40-60mm hail) or more are known to have had swath lengths of 20 km or more. Hailstorms with a swath length of 200 km or more have occurred on five occasions." The authors further note that "since 1800, the 13 storms assessed as (a) H4–5 intensity or more and (b) with a known swath length of 100 km or more have had an average maximum width of 12 km, emphasising the magnitude of these events. Historical claims of hail swaths exceeding a width of 20 km are probably attributable to two or more separate storms following parallel, even overlapping tracks. It may be noted that hail swath widths are more difficult to identify for historic events as a denser number of reports are needed than for just swath lengths."

4.5 Lightning Climatology

The presence of graupel/hail is important for cloud charging leading to lightning discharges (Saunders, 2008). Therefore lightning could be used as a proxy for the presence of graupel and potentially hail. It is thought that the non-inductive charging mechanism whereby ice crystals growing by diffusion rebound from collisions with graupel/hail growing by accretion of water droplets is the most important (Blyth et al. 2001, Latham et al. 2007). During collisions charge is transferred and differences in sedimentation rate lead to charge separation within the cloud, potentially resulting in a lightning discharge. Therefore, lightning climatologies can provide a picture of when graupel and hail amounts are likely to be maximum throughout the day and seasonally. A number of researchers have shown linear correlations between ice water content and flash rate (Petersen et al. 2005). Deierling et al. (2008) used multiparameter radar data to identify hydrometeor types and demonstrate that both graupel and hail content show a strong correlation with lightning flash rate within the storms studied. Potentially, these relations could be used to convert flash rate climatologies into graupel amounts.

A global climatology based on radio emissions (Lay et al. 2007) indicates a strong diurnal signal over the tropics and mid-latitude land areas. The peak in the diurnal signal is around 17LT, but the peak is earlier in Europe (15LT) and later in N. America (20LT). Over the sea the diurnal cycle is much weaker and peaks around 8LT. A satellite-borne optical detector has been used to construct a global map of lightning distribution and frequency (Christian et al. 2003). It shows heightened activity over much of South America, North America (excluding Canada), sub-Saharan Africa, Indian sub-continent, South East Asia, Australasia and Southern Europe to a lesser extent. The most intensely affected region is Central Africa. The mid-latitude regions are most affected by seasonal variations with the peak in activity during the local summer. Seasonal variations in the tropics are less apparent.

Dieirling et al. (2008) provide linear relations, derived from ground based radar, for lightning flashes and hail or graupel mass of the form: $F = A \cdot m + B$, where *F* is flashes per minute over the radar volume and *m* is

the mass of hail or graupel in the radar volume. *A* and *B* are constants appropriate for graupel or hail. Therefore, the lightning flash data could potentially be inverted to provide graupel and/or hail mass.

NASA have made available a lightning flash density climatology based upon spaceborne lightning detectors. These data combine 5 years OTD (optical transient detector) and 8 years of LIS (lightning imaging sensor) data that can detect both in-cloud and cloud to ground lightning. These data are provided as gridded monthly products in 2 hourly local time bins globally at 2.5x2.5degrees.

Figure 4.24 indicates the mean climatologies of lightning for the morning and afternoon in two seasons. It is immediately clear that the lightning flash rate is generally greater over land. The local afternoon period over land has greater flash densities than the local morning. The local summer extent of flash densities exceeding 0.001 km^{-2} day^{-1} is to within about 20 degrees of the pole over continental areas in the Northern Hemisphere and not so extensive in the southern hemisphere. The flash density in the mid-latitudes is modulated by the season with the summer giving rise to the greatest flash rates. Finally, there is no strong correlation between flash density and topographic features.

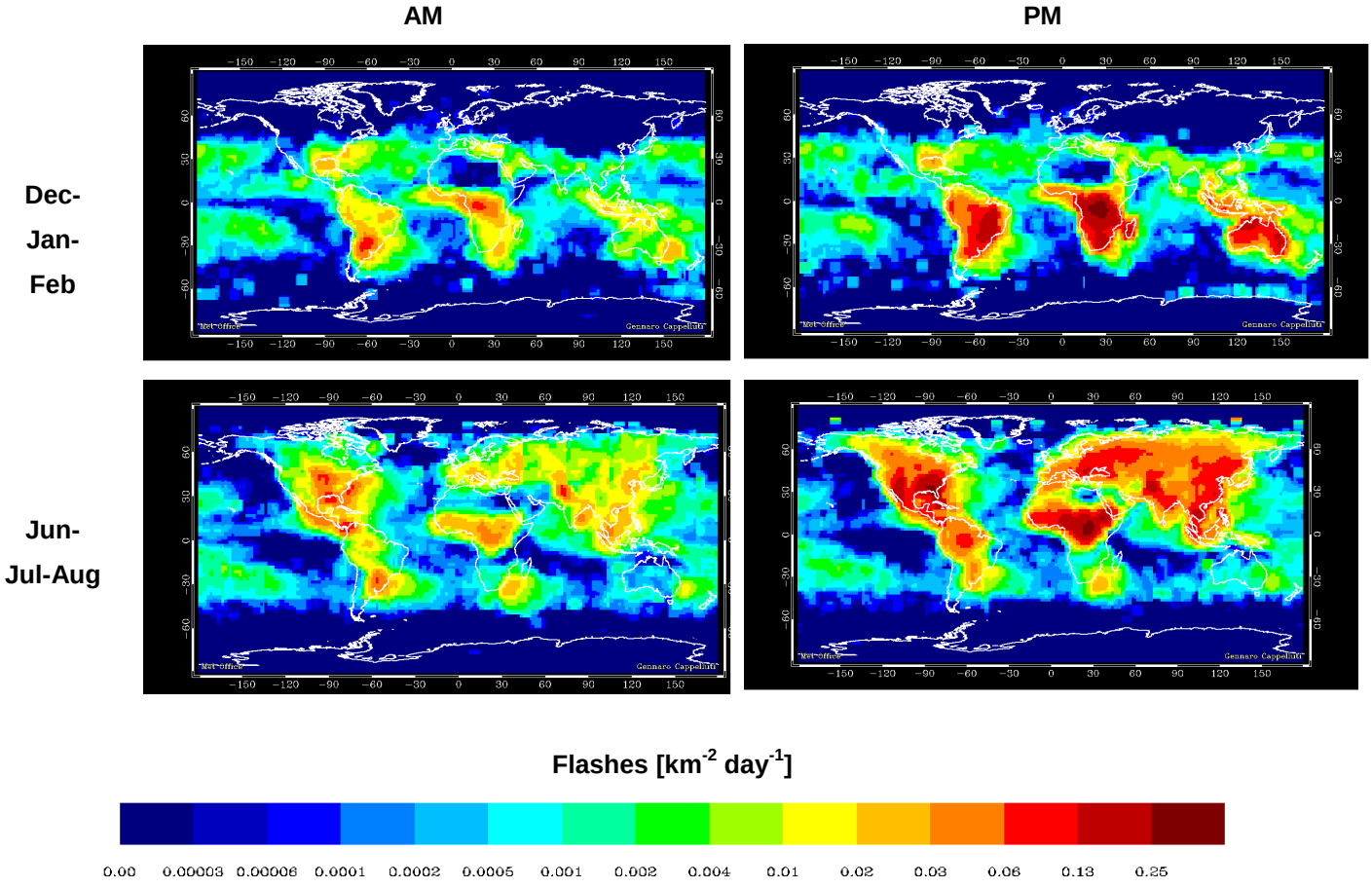

Figure 4.24 Mean lightning flash density for December-January-February and June-July-August in the local morning and local afternoon. Derived from NASA LIS/OTD lightning climatology

4.6 Review of Operational forecasting of hail using NWP models

4.6.1 Introduction

To forecast hail, deep moist convection is required, in addition to these three basic ingredients:

- Adequate updraughts to keep hailstones aloft for an appropriate amount of time.
- Sufficient supercooled water near the hailstone to enable growth as it travels through an updraught.
- A small fragment of ice or snow for it to grow upon.

All large hail events are associated with deep convection and usually, thunderstorms. However, there is no clear distinction between storms that do and do not produce hailstones. Nearly all severe thunderstorms probably produce hail aloft, though it may melt before reaching the ground. The more common multi-cellular thunderstorms can produce many hailstones, but not usually the largest hailstones. In the life cycle of the multi-cell thunderstorm, the mature stage is relatively short so there is not much time for growth of the hailstone. Supercell thunderstorms have sustained strong updraughts that support large hail. In all cases, the hail falls when the thunderstorm's updraught can no longer support the weight of the ice. The stronger the updraught the larger the hailstone can grow. Smaller hail events are also associated with deep convection though with less vigorous updraughts allowing the stones to fall out very quickly. Thunderstorms may or may not accompany small hailfalls.

Ideally hail forecasting will utilise outputs from numerical models capable of resolving the complex processes within convective clouds and thunderstorms. Although such models exist, the computing capacity required to run these operationally over large areas is prohibitive and so hail cannot be explicitly forecast. Therefore, in order to provide forecasts, the likelihood of hail is diagnosed from larger scale variables which can be predicted. This paper will review operational methods for diagnosing hail from large scale numerical weather prediction (NWP) model outputs.

4.6.2 Methods and techniques for diagnosing hail from NWP model outputs

4.6.2.1 General guides

Model winds are used to calculate vertical wind shear throughout the depth of deep convective clouds. Vertical wind shear is required to separate updraughts and downdraughts in multi-cellular storms underneath a cloud so that updraughts can persist long enough for hail formation (e.g. see Browning 1963).

Convective cloud tops above 15000 feet (4500m) and cloud top temperatures less than -20℃ will ensure that clouds are deep enough with sufficient supercooled water droplets.

Generally freezing levels, particularly wet-bulb freezing levels, need to be low enough in the atmosphere to prevent hailstones melting before they reach the ground. However, freezing level is less important for assessing hail size aloft.

Convectively available potential energy (CAPE) is often calculated and used to estimate vertical velocity in updraughts. CAPE is the amount of energy a parcel of air would have if it is lifted for a distance vertically through the atmosphere. CAPE is effectively the positive buoyancy of an air parcel and is an indicator of atmospheric instability. The larger the CAPE the greater the speed of the updraughts and hence the greater the risk of larger hail. CAPE is related to the peak updraught velocity W by assuming that the potential energy CAPE equals the kinetic energy of ascent of a portion of air. i.e. $W=\sqrt{(2.CAPE)}$.

In the USA an Energy Shear Index, which is CAPE x (Wind shear from 0 to 6 km), is used to estimate the duration of updraughts in thunderstorms. (Brimelow et al, 2002). Brimelow also cites another paper (Renick and Maxwell, 1977) which provides a diagram relating maximum hail size on the ground to the peak speed of updraughts and the air temperature in the updraughts (Figure 4.25).

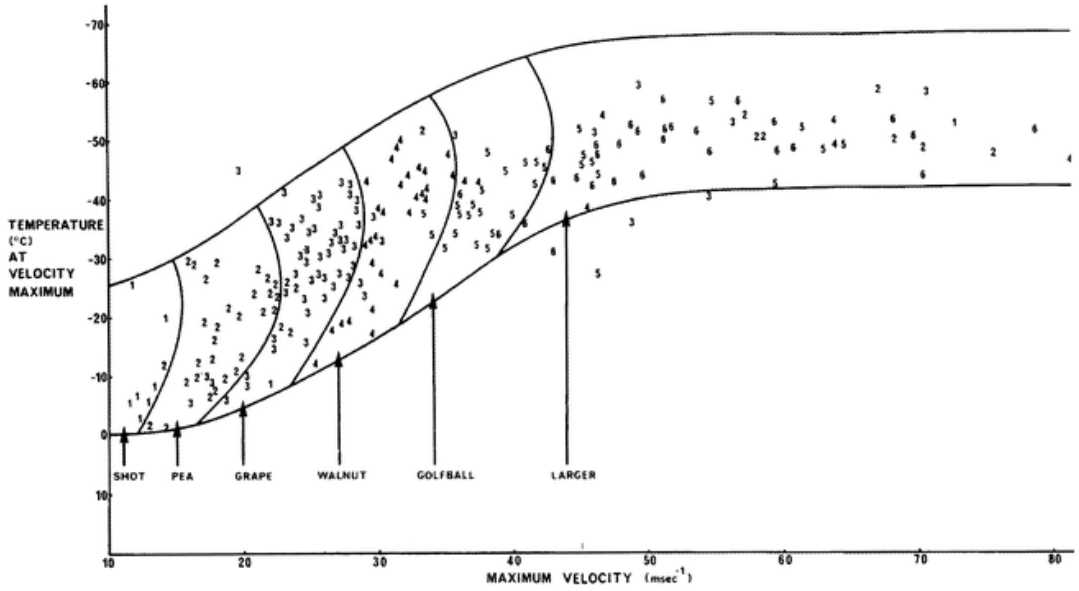

Figure 4.25 Nomogram developed by Renick and Maxwell (1977) that relates the maximum observed hail size on the ground to the forecast maximum updraught velocity and the temperature at the updraught maximum. Numbers 1–6 correspond to shot through greater-than-golfball-size hail.

Edwards and Thompson (1998) showed that taking parameters in isolation, such as cloud depth, CAPE and freezing level gave little skill in predicting whether hail would occur. Therefore, several predicted parameters need to be used in combination to provide reliable diagnoses of hail formation. All successful methods and techniques do this.

4.6.2.2 Specific methods and techniques

4.6.2.2.1 UK Met Office

In the old Met Office Nimrod Nowcasting system, (Golding, 1998), and in its recent successor, the Met Office UK high resolution model post-processing system (UKPP); hail is diagnosed if the numerical model predicts precipitation and the convective cloud base temperature is > 5℃ and the convective cloud top temperature is < -15℃ and the updraught vertical velocity is > 10 m/s. If the updraught vertical velocity exceeds 20 m/s then large (>10 mm diameter) hail is diagnosed.

Early this century the Met Office Nowcasting system was extended to include a package devoted to warnings of severe convective weather (SCW), including large hailstones impacting the ground. The probability of getting large hail in the SCW system was derived using statistically significant parameters from the NWP model which are detailed in Hand (2001).

Hail size is based on the technique of Fawbush and Miller (1953) which relates hail diameter to measurements from the vertical profile of temperature and humidity at a model grid point through a look-up table. The technique was extended by Miller (1972) to account for melting of hailstones in warm conditions and this has also been included. The technique was fully assessed by Hand (2000) before operational implementation with promising results. A sample of 16 cases in the UK was used to test the accuracy of the technique for forecasting large hail using Met Office Mesoscale Model forecast data. Out of the sixteen cases, eight were when large hail fell somewhere in the UK and eight were when no large hail was reported. The hit rate in the experiments was 63% with a false alarm ratio of 37% and a forecast bias of 1.0. However, the key result was that in the five cases when large hail was both forecast and observed, the old Mesoscale Model was able to pinpoint single occurrences of large hail accurately (to within 50km or four gridpoints). The model was also able to provide a useful indication of size, up to 9 hours ahead in one case.

The Fawbush and Miller (FM) technique is now being trialled in the current Met Office Site Specific Processing System (SSPS) which endeavours to provide accurate post-processed site specific forecasts from NWP model data globally.

The FM technique has also been trialled in Belgium (Dehenauw, 2003) with the conclusion that the technique can be used successfully to forecast large hail from mesoscale NWP model output. The cases examined proved to be in good agreement with available observations, which were the most memorable severe (convective) Belgian weather events since 1967.

4.6.2.2.2 Canada

Brimelow et al (2006) investigated the feasibility of producing maps of the forecast maximum hail size over the Canadian prairies using 12-h forecast soundings from an operational NWP model as input for a numerical hail growth model (HAILCAST). Specifically, the Global Environmental Multiscale (GEM) model run by the Canadian Meteorological Centre was used to provide the initial data for the HAILCAST model on a 0.5° by 0.5° grid. Maps depicting maximum hail si ze for the Canadian prairies were generated for 00 UTC for each day from 1 June to 31 August 2000. The forecast hail-size maps were then compared with radar-derived vertically integrated liquid water data over southern Alberta and surface hail reports. Verification results suggested that the forecast technique was skilful at identifying the occurrence of a hail day versus no-hail day up to 12 hours in advance. The technique was also skilful at predicting the main hail threat areas. The maximum diameter of hailstones was generally forecast quite accurately when compared with surface observations. However, the technique demonstrated limited skill when forecasting the distribution of hail on a small spatial scale (<60km).

HAILCAST comprises a steady-state cloud model linked to a hail growth model. The cloud model requires vertical profiles of ambient temperature, humidity, and wind. These data are then used to compute vertical profiles of liquid water content, updraught velocity, and in-cloud temperature that are representative of the hail growth environment close to the updraught's core. The time-dependent hail model then uses these data to simulate the growth of hail in the updraught. A drizzle-sized hail embryo is introduced at cloud base and this then grows by either wet or dry growth. Allowance is made for melting of a hailstone as it descends below the in-cloud freezing level. During wet growth (melting), excess accreted water (meltwater) on the surface of the stone is shed.

Work is ongoing to test whether a probabilistic approach from NWP ensembles may assist in predicting the location and size of hail, with maps showing the probability of hail diameter exceeding certain thresholds, as well as the standard deviation of the forecast hail sizes.

4.6.2.2.3 USA

Most hail forecasting in the USA from NWP models is achieved subjectively by looking for key combinations of factors important for hail formation in model outputs as described in section 4.6.1 . The FM technique is also used to determine hail size. Gordon (2000) provides a check list that forecasters in the States will follow when considering hail formation.

4.6.2.2.4 Spain

A poster prepared by Segala et al (2002) shows a system for objectively providing hail forecasts from NWP derived instability indices. This approach is archetypal of those employed in other Met. Services. The algorithm used is a decision tree based on values of important indices for convective activity derived from NWP outputs. The final output is the probability of getting hail in three categories; high, moderate and low. Performance so far has been satisfactory but with some shortcomings.

4.6.2.2.5 Russia

Shakina et al. (2000) discuss a possible application of output data from operational forecasting models to predict hail-hazard situations over the Northern Caucasus. Discriminant analysis is used to estimate the information value of different predictors calculated in large-scale models for predicting hail-hazard situations.

4.6.2.2.6 Greece

Dalezios and Papamanolis (1991) examine the performance of several atmospheric instability indices for operational hail forecasting in the Greek National Hail Suppression Program (GNHSP). These indices are part of the adopted forecasting procedure in the GNHSP, which also involves a synoptic index of convection and a scheme for determining the synoptic scale of likely threats. The assessment of the indices was accomplished objectively through a multivariate statistical technique, namely factor analysis.

4.6.3 Summary

It is very difficult to predict and even diagnose hail on small space and time-scales. Direct modelling of hail is possible in a research environment but prohibitively expensive operationally, however, the HAILCAST model shows promise. The most common approach is to use statistical methods using NWP large scale parameters as predictors with varying degrees of success and still plenty of room for improvement. There is no universally agreed set of predictors and it is recognised that these may vary locally anyway.

5 Meteorological Component: Methodology

Ground based reports of hail suffer from a number of limitations including generally being constrained to regions of habitation, subjective reporting and an increase in the number of reports correlated with the spread of communications and population. To produce a globally consistent climatology of hail two general approaches were considered. The first was a model based approach where hail was diagnosed from

environmental variables obtained from an atmospheric global circulation model. It is not yet possible to carry out routine high resolution (~1km grid spacing) modelling of the global atmosphere and so archived data from the operationally run Met Office global model was used to diagnose the presence of hail. While this method will provide a global picture of hail occurrence at the surface it is difficult to extend this method to provide estimates of the likelihood of hail at different altitudes. Results from the model based hail climatology will be shown. A second approach was to make use of satellite observations. Passive microwave observations of ice were first considered, but the broad footprint of the satellite sensing area, the sensitivity of the instrument to other types of ice and the lack of diurnal behaviour exhibited by these observations but expected for hail meant that this approach was abandoned. Radar observations from space provide a vertical profiling capability associated with a relatively small sampling area. These data were used to estimate hail occurrence within three temperature ranges. To compute probabilities of collision between an aircraft and hail two pieces of information need to be combined. First, the frequency of radar reflectivities representing hail containing volumes and secondly the physical environment assumed to exist within such volumes.

6 Meteorological Component: Implementation

6.1 Model Approach: Convective Diagnosis Procedure

The convective diagnosis procedure (CDP) is used by the Met Office to obtain information about significant weather events that are not explicitly represented in the weather model (see section 4.6.2.2.1). Such events include probability of lightning and maximum hail size at the ground. Algorithms to determine these are typically carried out at discrete sites around the world such as aerodromes.

To diagnose the occurrence of hail the following procedure is followed (see Hand 2000). Only locations over land where the global model diagnosed convective rainfall were considered. If the parcel CAPE (Convective Available Potential Energy) is greater than 50 JKg^{-1} (equivalent to a peak vertical velocity of 10 ms^{-1} at cloud top) and cloud top temperature is less than -20℃ with a cloud depth greater than 3500m and a base below 5000m above ground level, then the potential for hail is assessed. These conditions will provide an increased likelihood of cumulonimbus clouds with strong updrafts, liquid water, and with a good portion of the cloud layer below freezing (0 ℃). Possible hail size is determined using the technique of Miller (1972) which has provided useful guidance to Met Office forecasters in recent years.

The method uses convection parcel theory to estimate the available potential energy that is converted into the vertical velocity acquired by a parcel ascending in the lower part of a cloud below the -5℃ level. The greater the vertical velocity then the larger the size of the hail stone that can be developed by accretion processes. Depth of cloud below the -5℃ level is assessed through inspection of thermodynamic profiles. Provided the cloud top is sufficiently cold for ice to form (< -20℃) then a relatively large cloud layer below the -5℃ level will provide ideal conditions for hail growth. However, the relationship between having sufficient upward motion to support large hail and favourable conditions for hail growth is such that both are needed for really large stones to develop.

A look-up table based on Miller (1972) provides hail size based upon estimates of the available potential energy and cloud depth. If the wet-bulb freezing level is higher than 3350m then hailstones are allowed to melt by an amount according to the height of the wet-bulb freezing level and diagnosed hail size. All hailstones of any size are deemed to melt completely before reaching the ground if the wet-bulb freezing level exceeds 4400m. As a last check, if the final hail size is greater than or equal to 10 millimetres and CAPE is less than 400 JKg^{-1} then the hail size is set to 5 mm since peak vertical velocities implied from the CAPE would theoretically not be large enough to support large stones.

Global model fields for 00,06,12,18 UTC were obtained for every day between the beginning of 2004 and the end of 2008 to produce a 5 year climatology using the CDP. The CDP hail day density maps have been produced by counting the soundings with hail size greater than or equal to 15 mm in each 1°×1° cell and in at least one 6h LT (local time) slot each day, between Jan 2004 and Dec 2008. The seasonal hail day densities per 1 degree square have been computed by dividing the seasonal number of these soundings in each cell by the total number of daily soundings in the season excluding days when model data were missing at all the four times of 00, 06, 12 and 18 UTC.

Similarly, CDP hail day histogram tables have been produced by counting the soundings with hail size greater than or equal to 15 mm in at least one of the 1°×1° cells of each ROI (Region Of Interest) and in at least one 6h LT slot each day, between Jan 2004 and Dec 2008. The monthly hail day densities have been worked out by dividing the monthly number of these soundings in each ROI by the monthly number of daily soundings and excluding days when model data were missing at all four times. Results from this approach are shown in section 7.1.

6.2 Radar approach: hail probabilities from TRMM radar data

6.2.1 Introduction

To obtain hail information at different levels throughout the atmosphere we have made use of the TRMM (Tropical Rainfall Measurement Mission) satellite-borne radar. We have utilised data from the TRMM cloud and precipitation database produced by the University of Utah and described in Liu et al (2008). The level1 data from this database contains entries for each radar profile. For the purposes of this hail study each radar sample is assumed to be independent, covers a region about 5 km wide and returns vertical profiles of radar reflectivity in 250 m range gates. The orbit of the TRMM satellite restricts data coverage to between 37N and 37S (see fig.6.1, 7.9 for geographic coverage). Although the coverage is not global the lightning climatology (fig. 4.24) indicates that this region has the most intense lightning activity and hence likely to also represent the highest frequency of graupel and hail. This geographic bias in the radar sampling will likely bias the radar

probability distribution functions (pdfs) to a greater relative frequency of high reflectivity samples than if the whole globe were sampled.

The TRMM precipitation radar is a 13.8 GHz single parameter radar and so only reflectivity factor is available to use as an indicator of the presence of hail. Previous work has indicated that reflectivity factors exceeding 45 dBZ indicate the presence of hail (Straka et al. 2000). Donaldson (1961) showed that 50 dBZ at 9km was accompanied 53% of the time by large hail (D>12mm) and 71% of the time by hail. Cecil (2009) shows that 74% of the 49.1 dBZ values from TRMM at 9km altitude are associated with hail on the ground greater than 20mm in size and 43% of those cases where 43.1 dBZ was observed at 9km. Hail detection algorithms appropriate for the US weather radar network use thresholds for hail between 40 and 50 dBZ (Witt et al. 1998, Donavon and Jungbluth 2007). In particular the height difference between the maximum height of the 50dBZ and melting layer has been used to provide an estimate of the severity and presence of hail at the ground.

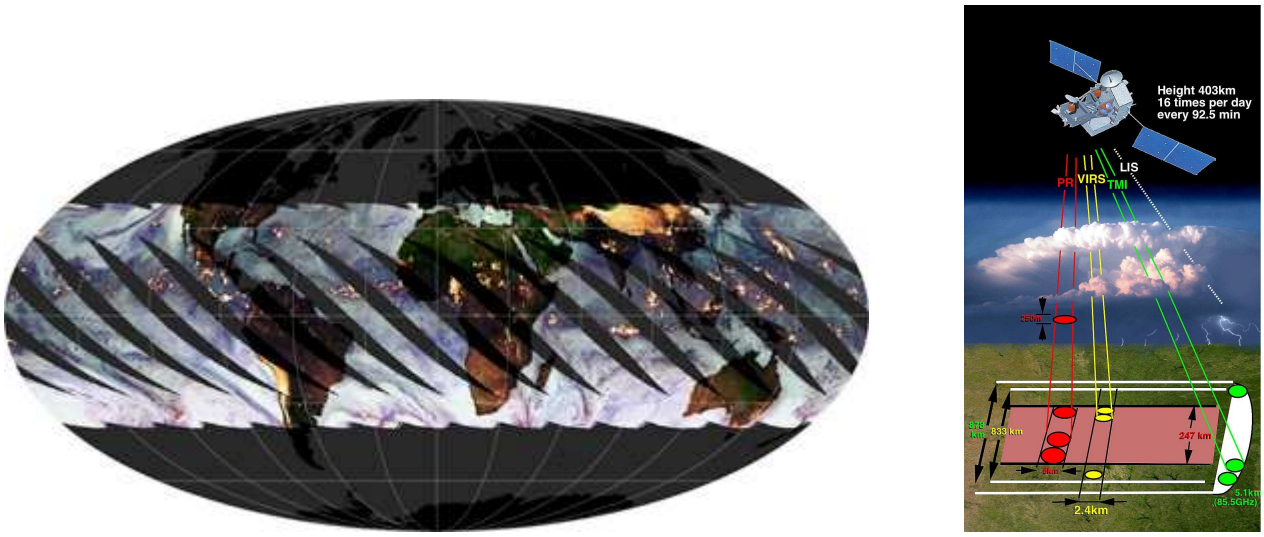

Figure 6.1. Left: Image showing the global tropical coverage of the TRMM satellite. Right: Schematic of TRMM satellite sampling. Of interest here is the Precipitation radar (red, PR) Images reproduced from NASA.

Each radar profile is reported in terms of height. However modelling studies show that graupel water contents tend to reach a maximum about the freezing level. Therefore, given the wide geographical sampling of the TRMM satellite and the variation in the height of the freezing level, it was decided that the radar data should be ordered in terms of temperature. Three temperature ranges were chosen (-2 to -5C, -15 to -20C, -35 to -40C). Radar height was converted to temperature using NCEP reanalysis data. For each profile, the maximum reflectivity from any individual 250m height range within the temperature range was used. Choosing temperature ranges colder than freezing also helps to avoid contamination from rain that can generate a large reflectivity signal.

Nine years of data (1998-2006) have been used. The data have been binned in 2°x2° boxes (180 longitude , 37N-37S latitude range), six 4-hour time windows throughout the day and 1dBZ wide radar reflectivity bins.

For this study the reflectivity factor needs to be converted to a hail size distribution. To do this a number of assumptions need to be made.

i) Assume that the microphysical environment within the 5km radar footprint is homogeneous and contains only hail. Regions of hail may be smaller, more intense and surrounded by other hydrometeor types. Rain can give rise to high radar reflectivities. Assuming uniformity allows the computation of the probability of intercepting one or more hailstones for a given size or bigger when regions possessing a given reflectivity factor are considered.

ii) Assume dry hail. Relatively more larger dry hail are required to produce the same radar signal as wet hail.

iii) Assume an exponential distribution describes the hail size distribution to large sizes (~10cm) [$N(D)=N_0\exp(-\lambda D)dD$]

iv) Assume that regions exceeding a threshold value for radar reflectivity contain hail.

v) Assume that each hail region is independent

vi) Assume that the TRMM attenuation correction is accurate for the conditions when hail is present.

vii) Because there are two parameters in the exponential distribution and only one observed variable, a further assumption has to be made about one of these parameters. A minimum slope value (λ=200 m^{-1}) based on a minimum value representative of the observations has been chosen. This is a worst case value that leads to the highest relative frequency of large particles within a size distribution. Therefore, all of the resulting probabilities and concentrations will be worst case estimates.

Assuming an exponential distribution represents the instantaneous distribution of hail, assumptions about the parameters controlling the distribution can be made to link the shape of the hail size distribution to radar reflectivity when Mie scattering is considered.

$$Z = 10^{18}\frac{\Lambda^4}{k^2\pi^5}\int n(D)\sigma(D)dD \quad , \qquad 6.1$$

Where Z is the equivalent radar reflectivity factor [$mm^6\ m^{-3}$], Λ [m] is the radar wavelength, k^2=0.93 for water, σ [m^2] is the radar cross section derived using the Mie solution for solid ice spheres with diameter D [m], and n(D) [m^{-3}] is the concentration of particles between D and D+dD. Reflectivity factor in dBZ is then $Z_{dBZ}=10\log_{10}(Z)$. A size distribution was found for each value of Z using an iterative approach.

6.2.2 Single events – collisions with one or more hailstones

Assuming a Poisson distribution the probability of seeing one or more particles (event A) larger than D_0 for a given reflectivity factor range is given by

$$P\left[A\middle|Z' < Z_{dBZ} < Z' + \Delta Z' \cap D > D_0\right] = 1 - \exp\left(-N\left(D > D_0, Z' < Z_{dBZ} < Z' + \Delta Z'\right)V\right), \quad 6.2$$

Where V is the volume swept out by an aircraft passing through the region represented by the satellite measurement of reflectivity factor. V=[width of region] x [frontal cross-sectional area of aircraft]. The frontal cross sectional area will vary with aircraft, but for illustration a value of 50 m^2 has been adopted, while the width of the region is 5000 m. Additionally, there is the possibility of collisions from above. For this case the sample volume is V=[width of region]/[airspeed]x[horizontal cross-section of aircraft]x[hailstone fallspeed]. For an aircraft with a horizontal cross sectional area of ~400m^2 ,an airspeed of 250 m s^{-1} the sample volumes are similar. Therefore, the results for intercepting particles on the leading edge and top side of the aircraft will be similar.

The probability of an event, A (at least one collision), taking place and reflectivity, Z_{dBZ}, being in the range $Z' < Z_{dBZ} < Z' + dZ'$ given that the particle size, D, is greater than a threshold size $D > D_0$ is

$$P\left[A \cap Z' < Z_{dBZ} < Z' + \Delta Z' \middle| \; D > D_0\right] =$$
$$P\left[A\middle|Z' < Z_{dBZ} < Z' + \Delta Z' \cap D > D_0\right] \times \int_{Z'}^{Z'+\Delta Z'} f(Z)\,dZ_{dBZ} \quad 6.3$$

Where the RHS is the product of the probability of an event, A, occurring given that Z_{dBZ} and D are both in their respective ranges and the integral of the pdf of Z_{dBZ} over the range Z' to Z'+dZ'.

So, the probability of an event, A, occurring if regions of radar reflectivity are encountered randomly according to the full pdf for Z_{dBZ} is

$$P\left[A\middle|D > D_0\right] = \sum_{Z'=-\infty}^{\infty} P\left[A \cap Z' < Z_{dBZ} < Z' + \Delta Z'\middle|D > D_0\right] \times \int_{Z'}^{Z'+\Delta Z'} f(Z)\,dZ_{dBZ} \quad 6.4$$

To assess the probability of the event if only regions of reflectivity that represent hail are sampled (P_h) a hail reflectivity pdf should be used: $f_{hail}(Z)$.

$$P_h\left[A\middle|D > D_0\right] = \sum_{Z'=-\infty}^{\infty} P\left[A \cap Z' < Z_{dBZ} < Z' + \Delta Z'\middle|D > D_0\right] \times \int_{Z'}^{Z'+\Delta Z'} f_{hail}(Z)\,dZ_{dBZ} \quad 6.5$$

where pdf in eq. 6.5 is defined as

$$f_{hail} = \frac{f(Z_{dBZ})}{\int_{Z_{dBZ} > Z_{hail}} f(Z_{dBZ}) dZ_{dBZ}}$$

$Z_{dBZ} \geq Z_{hail}$,

$Z_{dBZ} < Z_{hail}$, $f_{hail} = 0$ 6.6

And because the reflectivity data are binned in terms of reflectivity the pdfs are in the form of histograms $\int_{Z'}^{Z'+\Delta Z'} f_{hail}(Z) dZ_{dBZ}$, $\int_{Z'}^{Z'+\Delta Z'} f(Z) dZ_{dBZ}$ that can be used directly in eqs 6.4, 6.5.

6.2.3 Multiple events – collisions with many hailstones

While Poisson statistics are required to analyse infrequent events, once multiple events of order 10s or 100s are considered then it is possible to simply inspect the product of the particle concentration and sample volume.

7 Meteorological Component: Outputs and Results

7.1 Comparison between CDP data and existing climatologies

The hail days estimated by the CDP are in general agreement with the local climatologies, both in terms of spatial distribution and in terms of temporal occurrence. However, they differ significantly in magnitude, the CDP data are systematically higher. This could be due to the higher grid density of the CDP data, larger sample area and the fact that the available local climatologies are based on data collected over long time periods, sometimes over a century ago when the reports were less numerous than today. Another possible cause of the amplitude mismatch may be the definition of hail size in the climatologies. The hail size reported in the different climatologies may represent either the maximum hail size recorded on the ground or the average.

Inspection of figure 7.1 shows that in DJF (December-January-February) the northern hemisphere has a low number of hail days, with most of the events occurring in Africa, over the Andes and in New South Wales (fig. 7.1 top left). The number of hail days in Europe, North America and Asia, increases in MAM (March-April-May, fig. 7.1 top right) and peaks in JJA (June-July-August, fig.7.1, bottom left). In SON (September-October-November) the highest hail occurrence is recorded mostly along the American and African mountain ranges, along with the Himalayas (fig. 7.1,bottom right).

A comparison of the CDP climatology with the global composite hail climatology (fig. 4.7) and lightning climatology (fig. 4.24) indicates that the CDP picks out relatively high occurrences of hail associated with topographical features such as the Rockies, Andes and Himalayas (fig. 4.7). However, the CDP does not

seem to completely reproduce the pattern seen in the lightning climatology over Africa which extends much further westward than the CDP suggests. Additionally, central USA is not highlighted as a region of frequent hail events by the CDP while both the lightning and global composites suggest that this region experiences relatively frequent hail events.

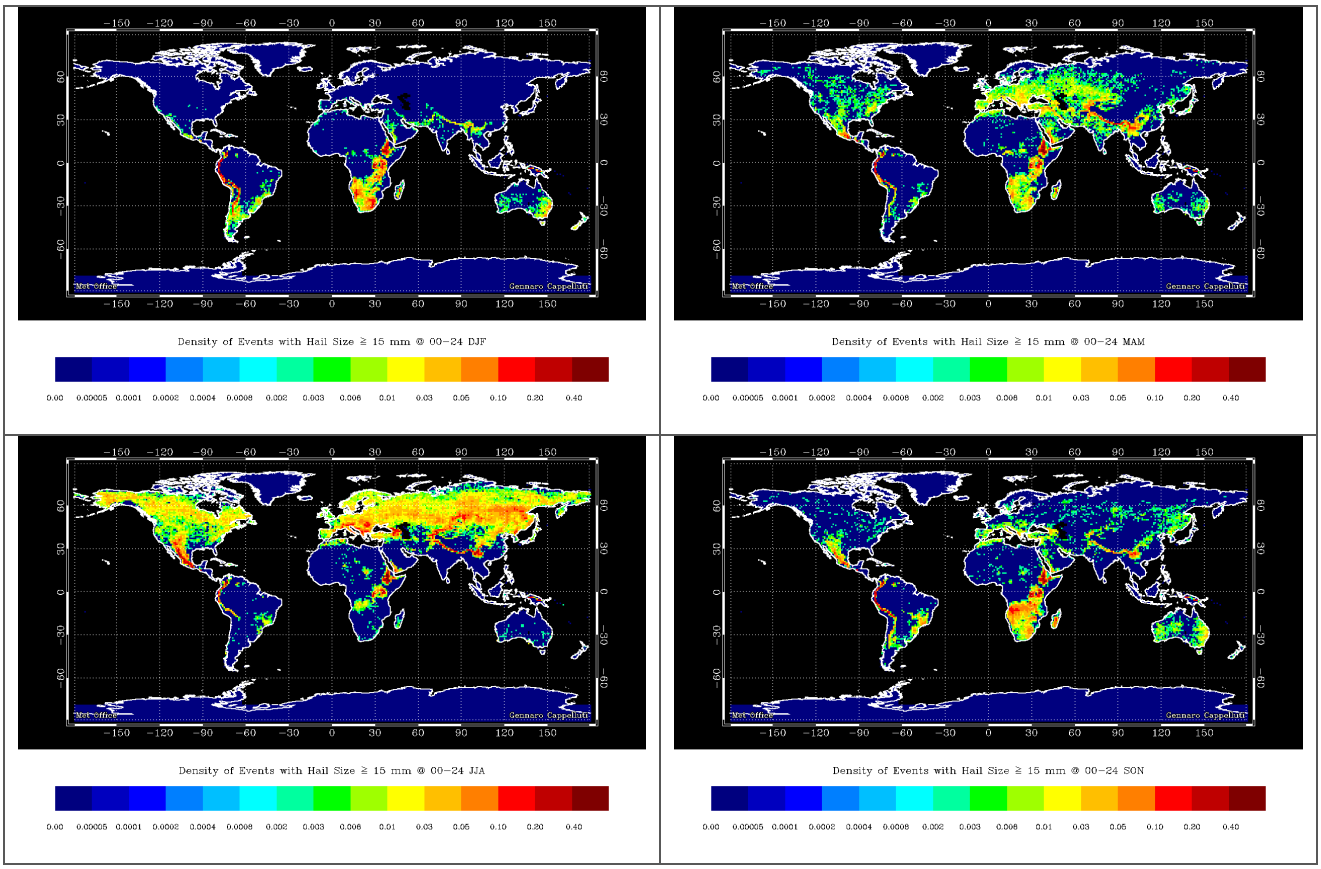

Figure 7.1: Global distribution of hail occurrence (number of events per day per 1 degree square) in each season.

7.1.1 New South Wales

The local climatology shows a peak in hail days in November, with 220 events over 212 years, which translates into about one event every November, over the whole of New South Wales. The number of events estimated using the CDP peaks in December with 2662 events, which corresponds to about one hail day every third day, in any location of New South Wales. This ROI is large and so this could be more realistic in the month with the greatest number of hailstorms.

Table 3 shows the CDP normalised density of hail days over the year. The relative frequency of normalised hail days in New South Wales are consistent with fig. 4.8.

	New South Wales	Finland	USA	UK
	Normalised relative frequency			
January	0.13		0.01	0.00
February	0.18		0.02	0.00
March	0.08		0.04	0.05
April	0.04		0.09	0.05
May	0.04	0.11	0.15	0.14
June	0.01	0.20	0.17	0.15
July	0.01	0.43	0.17	0.22
August	0.02	0.21	0.16	0.19
September	0.05	0.04	0.11	0.05
October	0.11		0.05	0.16
November	0.15		0.03	0.00
December	0.18		0.00	0.00

Table 3 Monthly distribution of hail days from CDP data. Each column shows the relative frequency of hail days in each ROI normalised to unity

Figure 7.2 shows the normalised density of hail days over New South Wales (NSW) in the different seasons. The monthly maximum over the selected ROI scaled up to represent 210 year totals as per the published NSW climatology (fig. 4.8) in DJF is 538 hail days, in MAM 100, in JJA 43 and in SON 247. Multiplying the maximum value divided by 210 years (a value of 2.6) can be used to convert the normalised density per month, per degree square (ranging between 0 and 1) shown in the maps into 'hail days per month per degree square'.

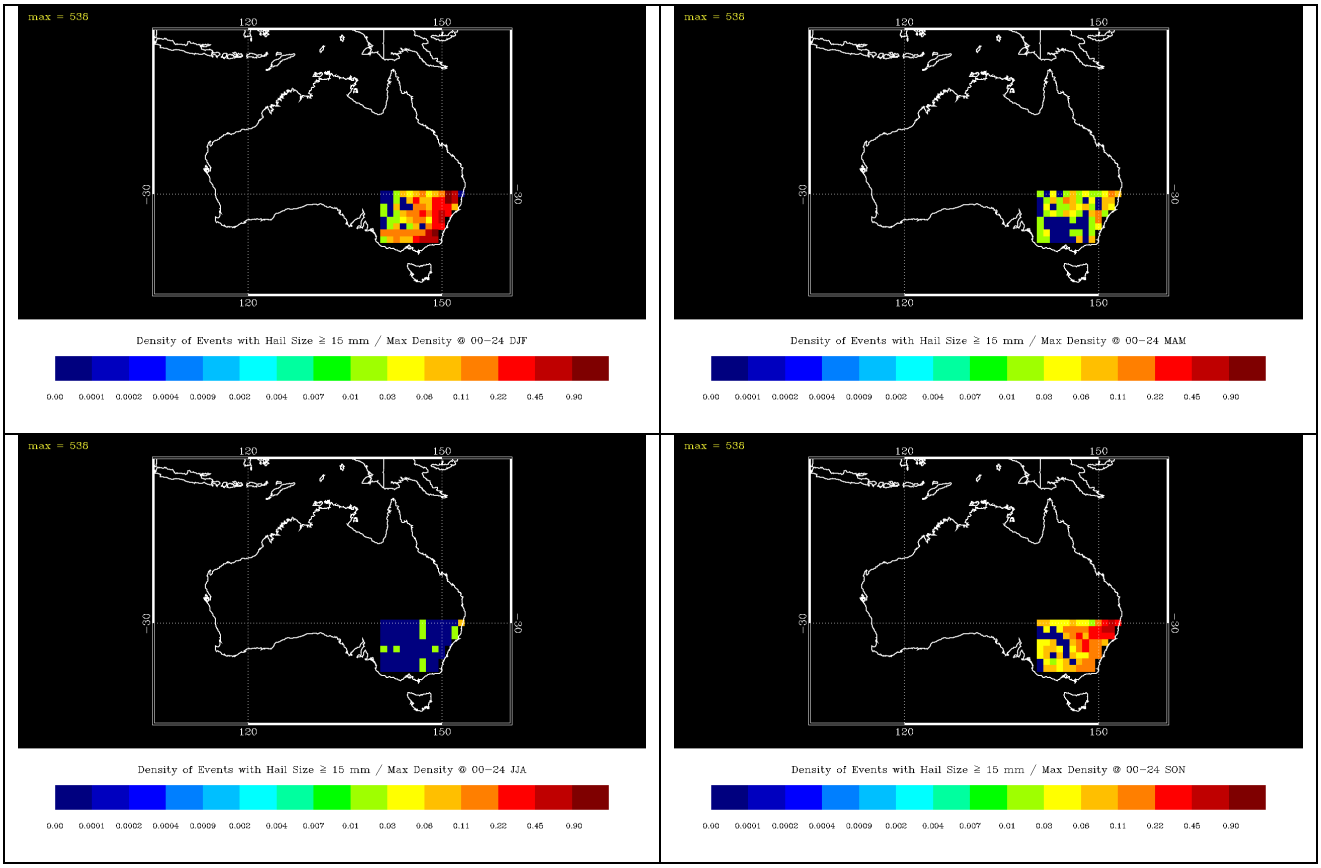

Figure 7.2 Normalised hail day density for 4 seasons over New South Wales. The density colour scale converts to 'hail days per month per degree square' by multiplying by 2.6.

7.1.2 Canada

The 30 year hail climatology for Canada (fig. 4.9) shows a peak of 5 hail days per year between May and September over the Rockies, while the CDP analysis (fig. 7.3) gives a peak of 8 hail days per year in the same period, but with hail days spread quite uniformly across the country.

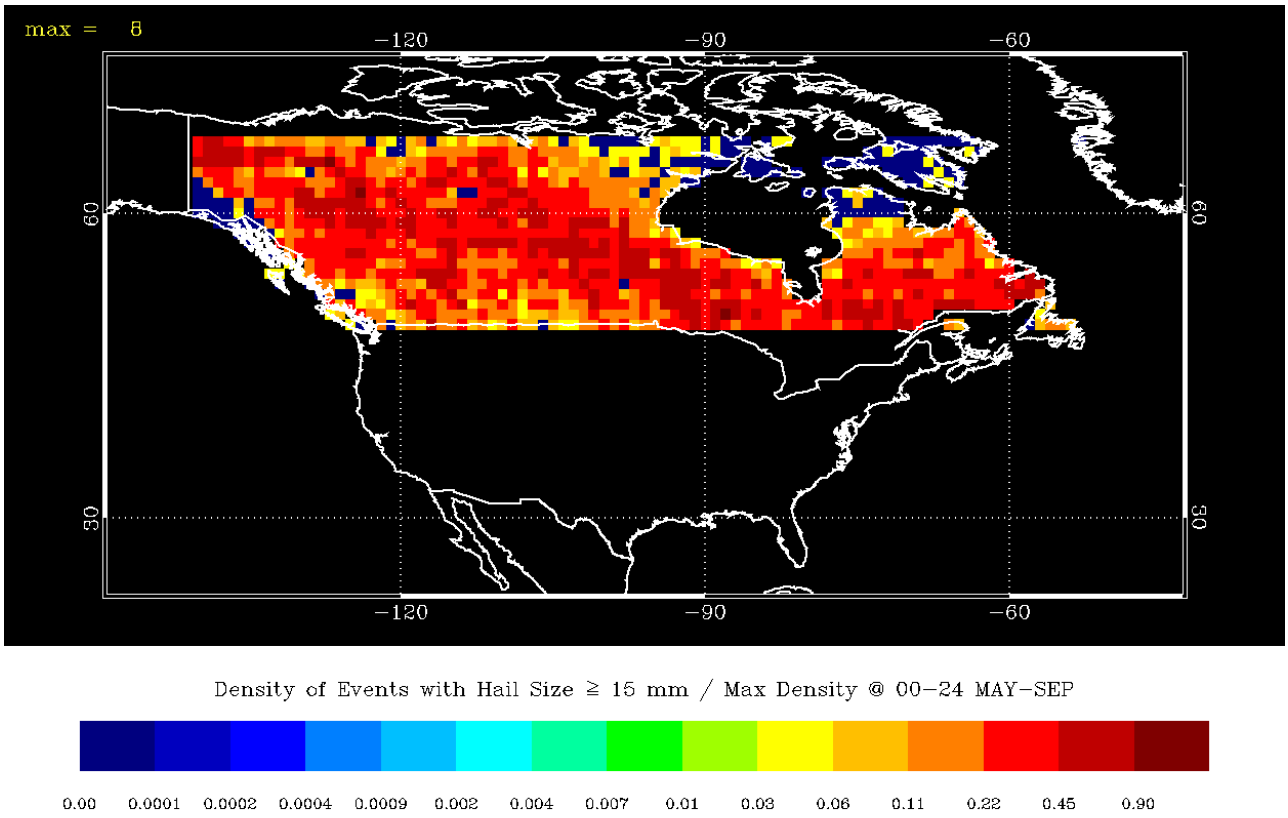

Figure 7.3 Normalised density of hail days per degree square in May-Sep over Canada. To convert the density colour scale to 'number of hail days between May and September per degree square' the values need to be multiplied by 8.

7.1.3 China

The 40 year published climatology for China shows a wide peak over the Tibetan Plateau, characterised by an average value of 20 hail days per year (fig. 4.10). The CDP has a maximum of 53 hail days per year at the border with Nepal and a reduction over Tibet and the Tarim Basin (fig. 7.4).

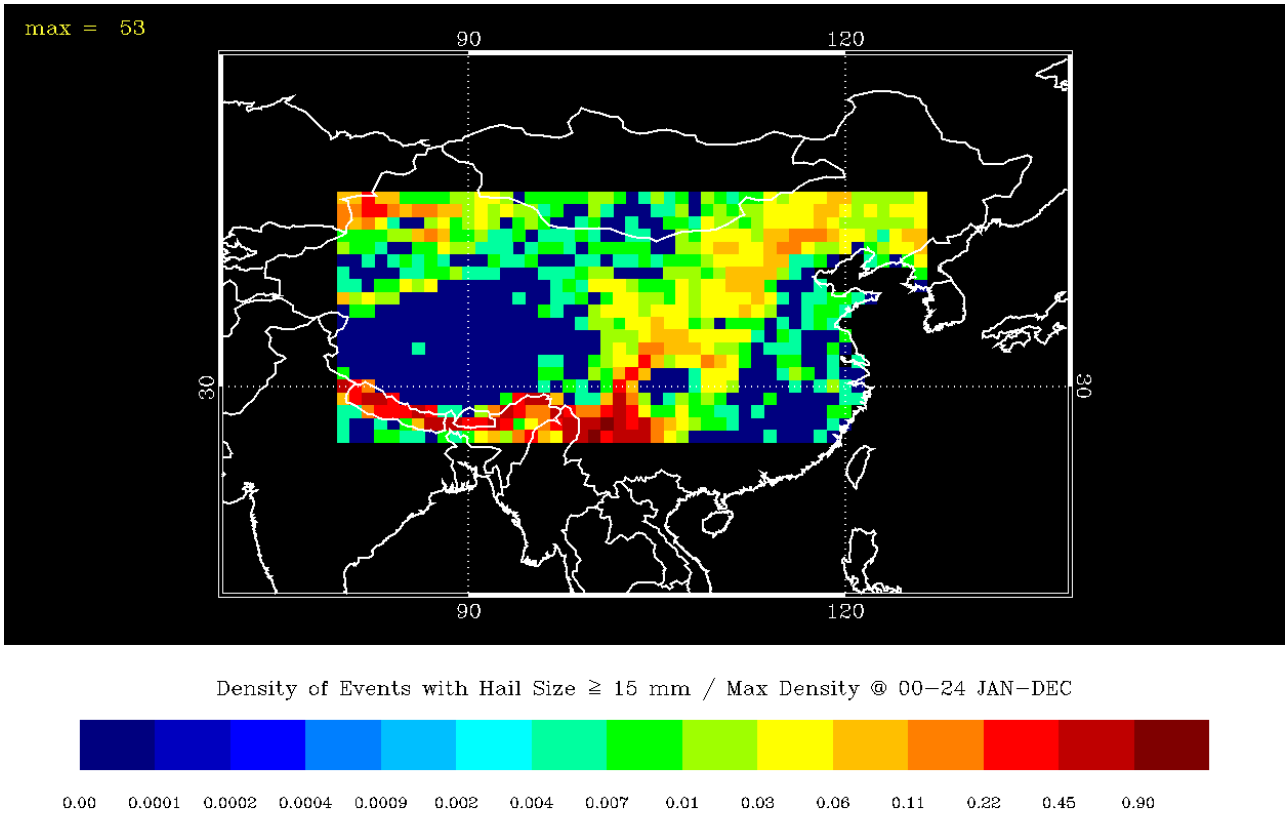

Figure 7.4 Normalised density of hail days per year per degree square over China and surrounding countries. To convert the density colour scale to 'number of hail days per year per degree square' the values need to be multiplied by 53.

7.1.4 Europe

The CDP data shows high densities of hail days over the Alps, Italy, Romania, ex Yugoslavia and Greece (the maximum being 22 hail days per year). Taking into account that the ESSL data (fig. 4.13) are biased over Germany due to a very dense observing network prior to 2005, the CDP peak areas broadly match the ESSL data, particularly over Romania and the Pyrenees.

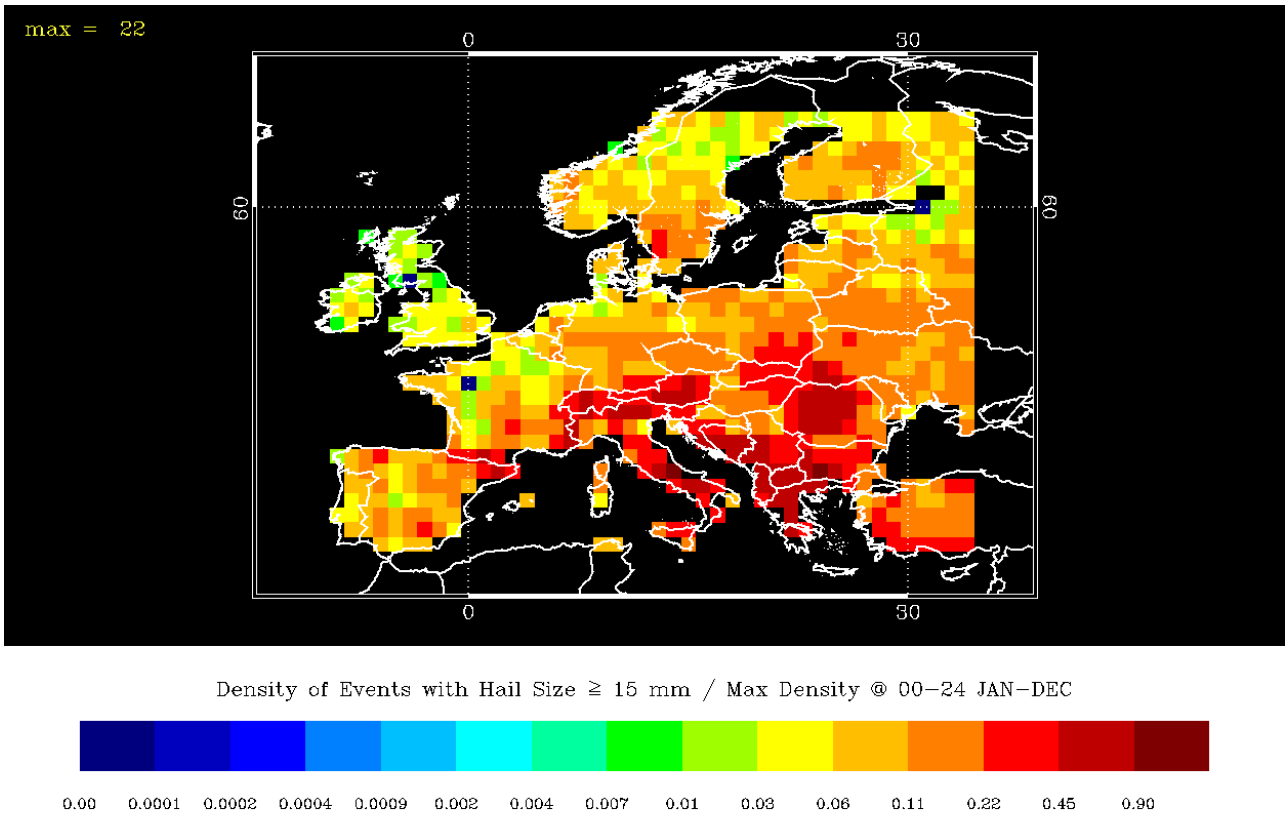

Figure 7.5 Normalised density of hail days per year per degree square over Europe. To convert the density colour scale to 'number of hail days per year per degree square' the values need to be multiplied by 22.

7.1.5 Finland

Table 3 shows the CDP normalised density of hail days between May and September with a good match with fig. 4.12. Figure 7.5 also shows the decrease in frequency of hail events in the north of the country.

7.1.6 UK

The distribution of density of hail days according to the month of the year (Table 3) is in good agreement with the local climatology (fig. 4.21). According to the CDP data, the highest number of hail days occur in central Ireland and the south east of England (fig 7.5) in good agreement with fig. 4.19.

7.1.7 USA

The NSSL observations show a peak in large hail days over Oklahoma (the local maximum is 9 hail days per year) and almost no large hail precipitation in the west of the country (fig. 4.15), whilst the CDP data shows New Mexico and Arizona as the areas with the highest density of hail days, the local maximum being 20

days per year (fig. 7.6). It is possible that smaller sized hail (less than ¾ inch or 19 mm) is much more widespread across the USA. Figure 4.15 only shows the frequency of hail for stone diameters greater than ¾ inch.

The NSSL point climatologies (fig. 4.16) show a constant increase in the number of hail days over the years, almost certainly because of increased habitation throughout the USA. Nevertheless, the shape of the NSSL probability distribution compares well with the CDP monthly frequency shown in Table 3.

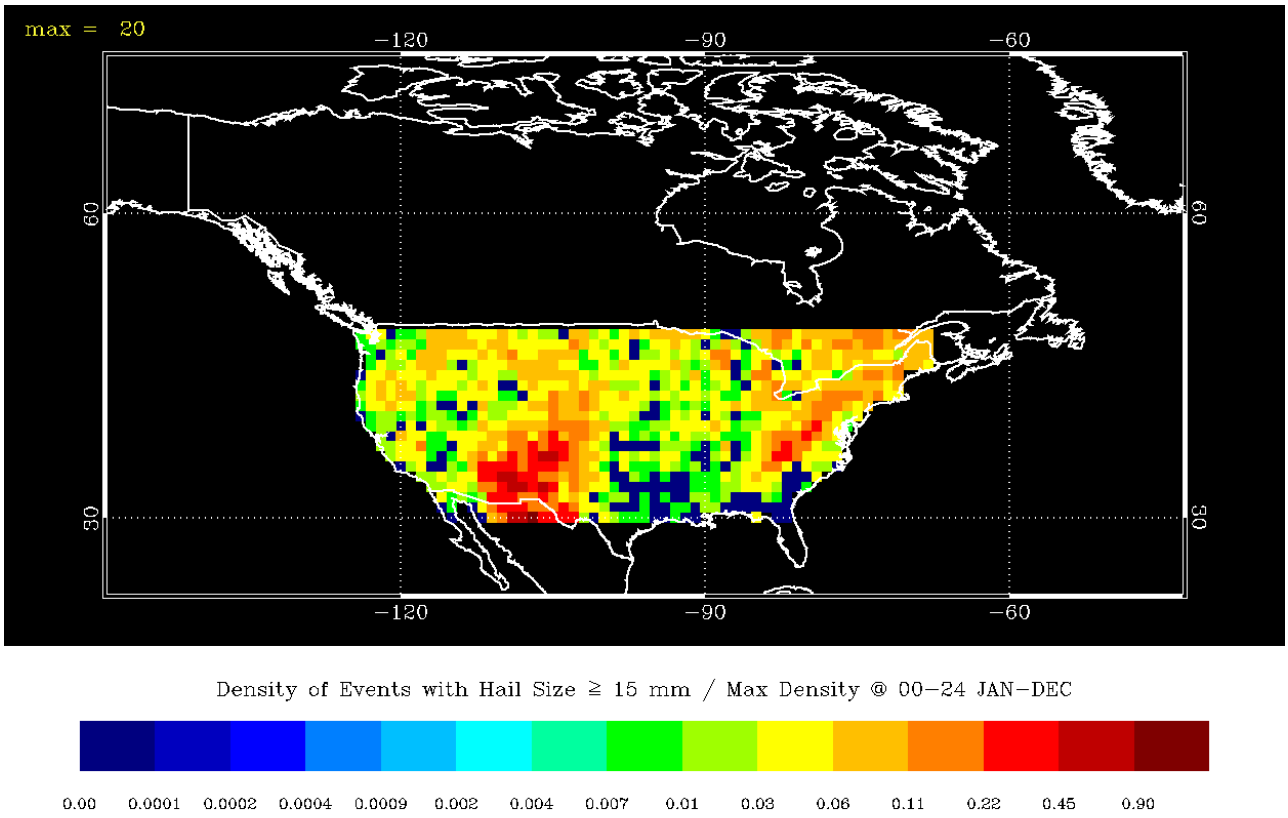

Figure 7.6 Normalised density of hail days per year per degree square over the USA. To convert the density colour scale to 'number of hail days per year per degree square' the values need to be multiplied by 20.

7.1.8 Africa

Over the African continent the CDP distribution (fig 7.7) matches the observed climatology very well (fig. 4.18) but the number of hail days where the maximum occurs, in Ethiopia, is much greater: 183 hail days per year against the 5 hail days per year reported by the 10 year climatology.

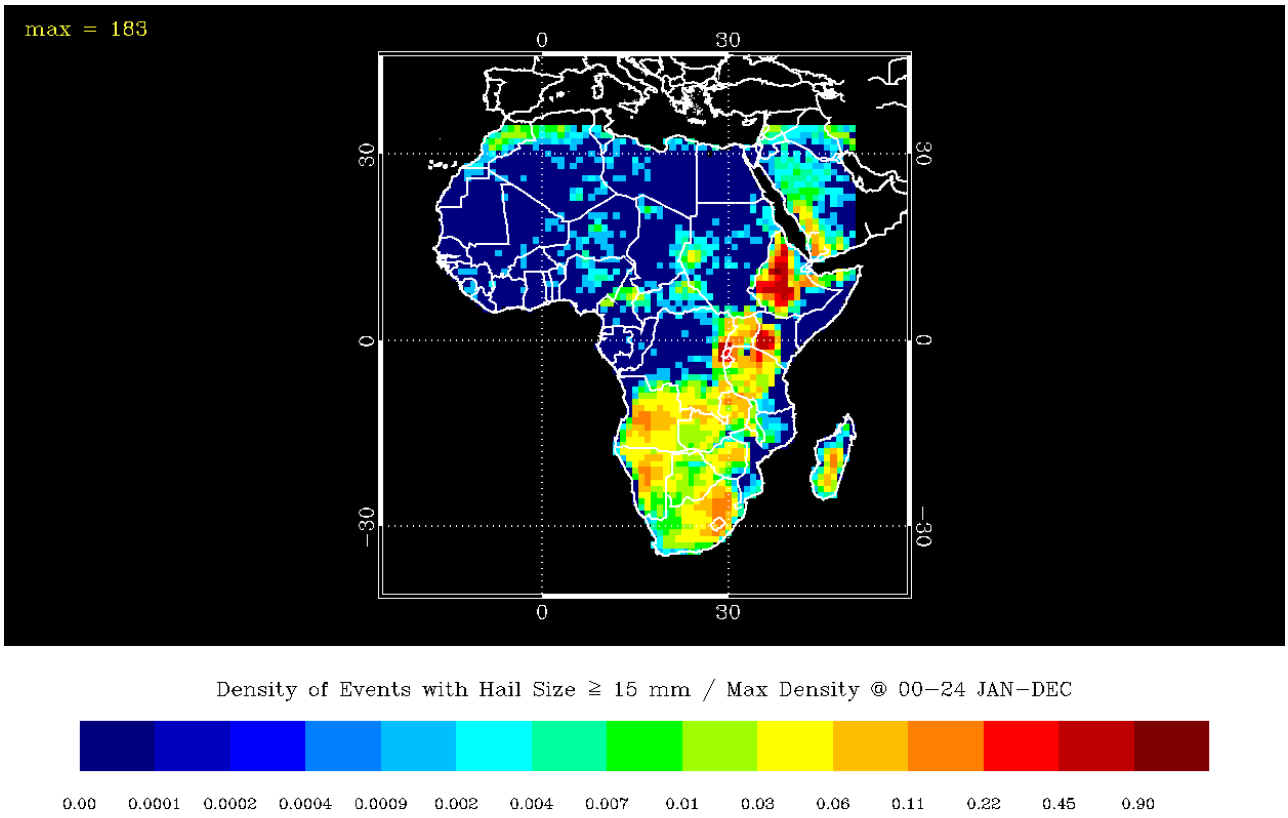

Figure 7.7 Normalised density of hail days per year per degree square over continental Africa. To convert the density colour scale to 'number of hail days per year per degree square' the values need to be multiplied by 183.

Generally the CDP results show a realistic seasonal behaviour. The diurnal behaviour of diagnosed convection usually results in an early peak in convective activity. This is true of most global models and will mean that the diurnal distribution of the occurrence of hail will also be slightly early. However, given the temporal coarseness of the data used (6 hourly) the diurnal variation produced by the CDP is also good with peaks mainly occurring in the 12-18 LT window.

7.2 Radar results

7.2.1 Evaluation of radar results

For hail we are interested in the pdf of reflectivities greater than some threshold value representative of hail. The threshold for detecting hail with the radar has been assessed by comparing the US Storm Prediction Center's database of severe hail events (hail with sizes exceeding 19 mm) with the TRMM observations. The Storm Prediction Center's hail database potentially suffers from under-reporting of hail events related to population density. Urban areas can report 2-3 times more than adjacent rural areas (Cecil 2009). Nevertheless, for each TRMM radar reflectivity observation within the chosen geographic domain (30.5N – 38N, 105W – 81.5W) the hail event database has been searched for events occurring within ±1° and ±1 ho ur of the TRMM observation. For this evaluation, the University of Utah TRMM database level 2 data (1998-

2006) has been used (liu et al. 2008). This dataset provides a maximum reflectivity profile for each storm identified (precipitation feature). If the individual 5km data were used this would lead to overestimates of the correlation of lower reflectivity values with hail.

Figure 7.8 shows the result for the three temperature ranges. Only points with greater than 10 radar observations have been shown. This graph shows the fraction of hail reports from the ground within 1 hour and 1 deg of the TRMM observation. It can be seen that ~90%, 60% and 30% of observations with 48 dBZ are associated with hail observations at the ground in the -35 to -40C, -15 to -20C and the -2 to -5C, temperature ranges. For low reflectivities (<35 dBZ) the fraction of associated hail observation tends to flatten out. This is a function of the search region in time and space. Greater search regions lead to greater background signals and also a greater maximum fraction of events associated with hail. These results essentially measure the correlation between the ground observations and the properties of the cloud at some temperature range. They do not constitute explicit evidence, but these curves can be used to imply the presence of hail within regions possessing relatively high radar reflectivities. One way to apply these curves would be to use them to filter the Z_{dBZ} pdfs to convert the TRMM observations to a pdf of hail events with an associated reflectivity. However, some assumptions would have to be made about choosing a reflectivity where the fraction of events goes to zero instead of the constant background value. A simpler approach is to threshold the reflectivities so that observations of Z_{dBZ} above this threshold are considered to be hail events. To some extent the choice of threshold is subjective but we have decided to pick the reflectivities where the curve for each temperature range exceeds the maximum fraction value minus half the difference between the maximum value and background level (fraction of events between 20 and 35 dBZ). The threshold reflectivities are 45, 49 and 50 dBZ for the -35to-40C, -15to-20C and -2to-5C ranges, respectively. As a compromise we have decided to use a single 48 dBZ as the threshold for all three temperature ranges. Sensitivity to this choice is discussed below.

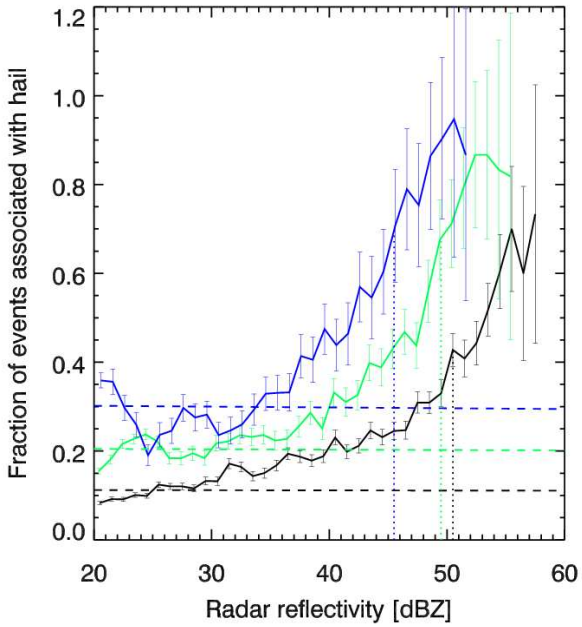

Figure 7.8 Fraction of hail events from TRMM radar observations associated with surface hail reports (solid lines). Black: -2 to -5C, Green: -15 to -20C, Blue -35 to -40C temperature ranges. The dashed lines represent the fraction of events between 20 and 35 dBZ and constitute a background for each temperature range. The errorbars are 1 standard deviation based on the number of events. The vertical dotted lines indicate the reflectivity value where the fraction of events exceeds the (maximum-0.5(maximum-background)).

Figure 7.9 shows the number of events in 2^o x 2^o boxes where reflectivities exceeded or equalled 48 dBZ between the temperatures of -2 and -5C for each season at 16-20 LT. To generate this map the number of observed events, n_{event}, per number of samples, $n_{samples}$, was scaled in the following way:

$$n = \frac{n_{event}}{n_{samples}} \frac{\left(2\times 111km\times 2\times 111km\times \cos\theta\right)\times\left(4h\times 30\times 3\right)}{\left(\pi\left(5km\right)^2/4\right)\times t_{event}}$$

This scales the fraction of observed events during the 4 h LT window in the 3 month period for a 2^o square (scaled with latitude, θ) by the areal and temporal coverage of the observations. The satellite sampling of each 5 km region is almost instantaneous. To avoid oversampling a time period is assumed for each observation that ensures observations are independent. The choice of value for this variable is open to debate but a value of 1 h has been chosen. Thus, n, is the number of events per 2^o square in the 4 h LT window for the given season if events last 1 h.

The patterns of hail events show a strong seasonal dependence and are confined mainly to the land. In the northern hemisphere spring (MAM) hail activity is confined to the Central and Eastern US, Central and West Africa, South and Eastern India and Northern Indonesia. There is also some activity in Brazil and Argentina. During northern hemisphere summer (JJA) activity spreads along the Rocky Mountains down into Central America, extends further eastwards in Central Africa and further to the north in India and China. The number

of events in South America are greatly reduced. Northern hemisphere autumn (SON) sees the reduction of events in the northern hemisphere, an increase in activity in South America and a migration of events further south in Africa. Finally, northern hemisphere winter (DJF) is the most intense season for South America and the southern half of Africa including Madagascar. Australia also shows a peak in activity during this season. This picture is largely in agreement with that produced from using microwave brightness temperatures (Cecil 2009). Figure 7.9 shows a good degree of correlation with the lightning climatology (fig. 4.24), with hail events extending into central and eastern USA as well as central and west Africa. However, one difference between the global composite of hail events (fig. 4.8) and the TRMM based climatology is the lack of events indicated by the radar over the Andes.

Figure 7.10 shows the number of events as a function of local time for one season only (JJA) and indicates that the afternoon hours contain the highest occurrence of events. The relative frequency of reflectivities greater than 48 dBZ show a peak in hail events exists within the 16-20LT time range. Therefore, in assessing the probability of encountering a hailstone during random flying the Z_{dBZ} pdf from 16-20 LT, JJA from over land points will be used to provide the highest probabilities.

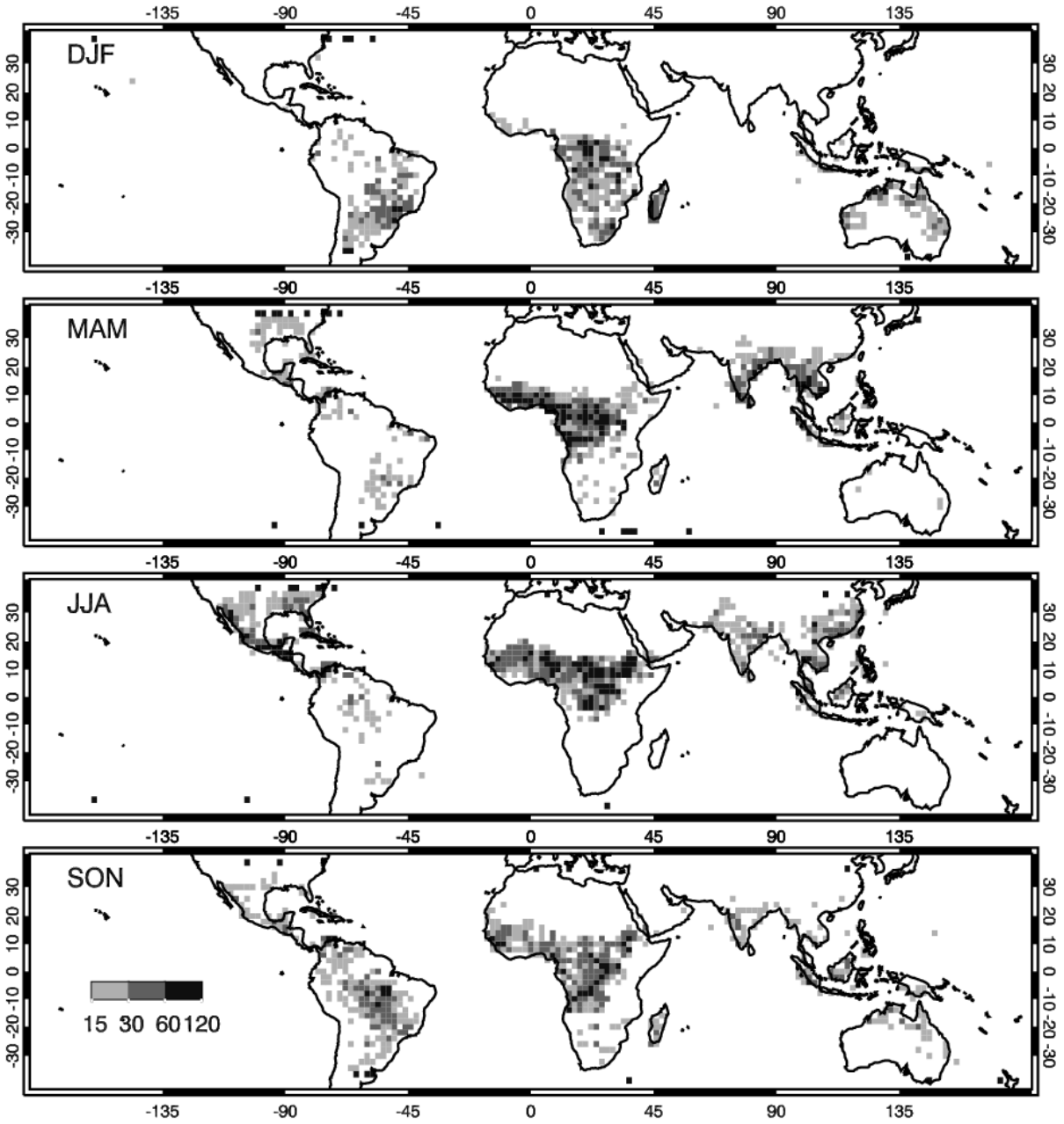

Figure 7.9 Scaled number of events per 2°x2° where Z_{dBZ}>48dBZ. Four seasons (DJF: December, January, February; MAM: March, April May; JJA: June, July, August; SON: September, October, November) are shown for the -2 to -5C temperature range and 16-20LT.

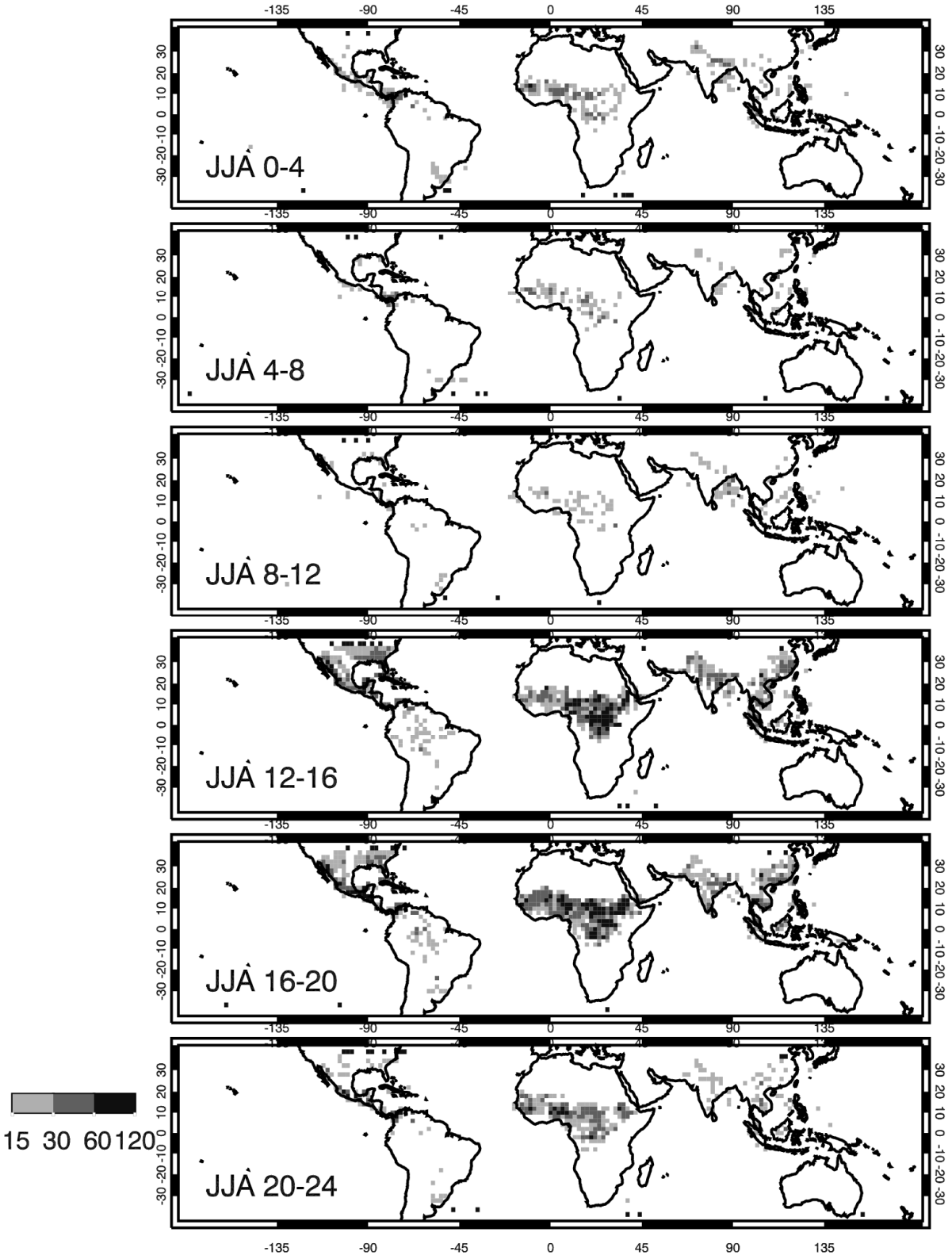

Figure 7.10 Scaled number of events per 2°x2° where Z_{dBZ}>48dBZ. A single season (JJA) for the -2 to -5C temperature range at 6 time periods (0-4, 4-8…LT) are shown.

It is clear that for different times of day, season and temperature range considered there is large variability in the frequency of reflectivities exceeding or equal to 48 dBZ. Figure 7.11 shows both cumulative distributions for radar reflectivities in 3 temperature ranges, for two seasons (DJF, JJA) and two time periods (8-12 LT, 16-20 LT) and a histogram of the same data in 1 dBZ reflectivity bins.

Figure 7.11 shows great variability but similarity in the shape of the distribution. If the distribution of reflectivities greater than some threshold representative of hail (Z_{hail}=48 dBZ) is considered then the distributions tend to converge. Fig 7.12 shows histograms of radar reflectivities greater than 48 dBZ, f_{hail}, formed from the full Z_{dBZ} pdf (eq. 6.6).

Figure 7.12 shows individual points for the 6 time periods throughout the day and two seasons (DJF, JJA). All of the points have collapsed onto single curves for each temperature range. Overplotted are histograms constructed from data obtained in all seasons and at all times for each of the three temperature ranges. These data (table 8) have been used to compute the probability of encountering hail of different sizes given that an aircraft is flying in regions of hail.

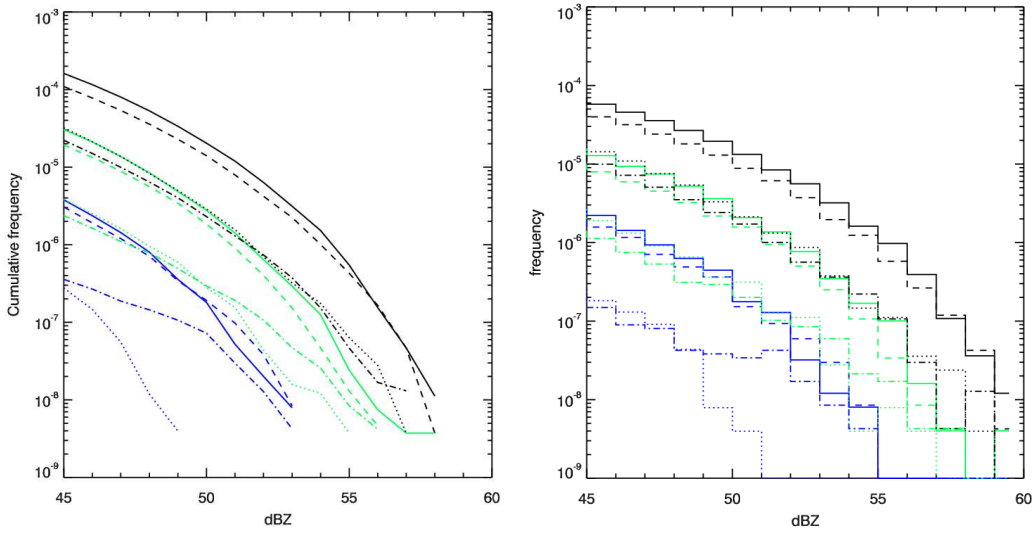

Figure 7.11(Left) Tail of the cumulative distribution of ZdBZ: $\int_{Z'}^{\infty} f(Z)dZ_{dBZ}$ **. (Right) histogram of normalised frequency of Z_{dBZ} observations:** $\int_{Z'}^{Z'+\Delta Z'} f(Z)dZ_{dBZ}$ **(see eq 6.4). Black lines: -2 to -5C, Green lines -15 to -20C, Blue lines -35 to -40C. Solid lines: JJA, 16-20LT, dashed lines DJF, 16-20LT, dotted lines: JJA, 04-08LT, dot-dash lines: DJF 04-08LT.**

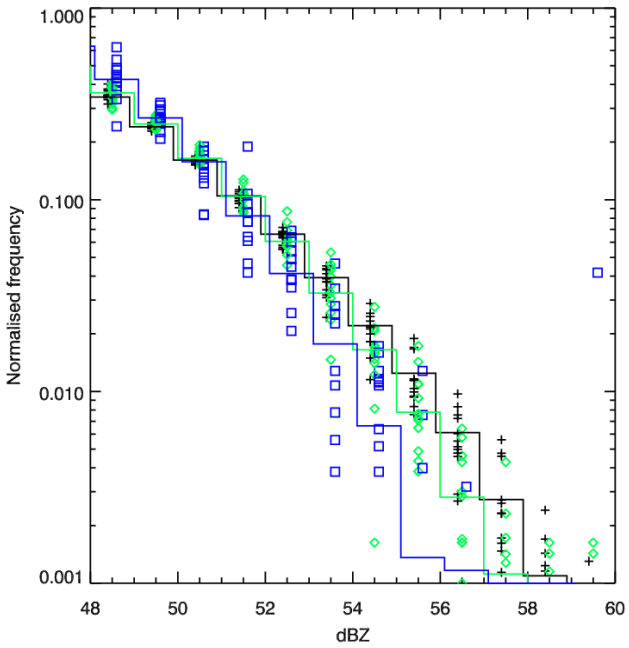

Figure 7.12 Solid lines are histograms of normalised frequency for regions where Z_{dBZ} is greater than the hail threshold (in this case 48 dBZ) derived from data from all seasons and all local times: $\int_{Z'}^{Z'+\Delta Z'} f_{hail}(Z)dZ$ (see eq. 6.5). Black lines: -2 to -5C, Green lines -15 to -20C, Blue lines -35 to -40C. The points are derived from the lines in fig. 7.11.

		dBZ											
Tmin [C]	Tmax [C]	48-49	49-50	50-51	51-52	52-53	53-54	54-55	55-56	56-57	57-58	58-59	59-60
-2	-5	3.40E-01	2.40E-01	1.60E-01	1.00E-01	6.60E-02	3.90E-02	2.20E-02	1.20E-02	6.10E-03	2.70E-03	1.10E-03	3.40E-04
-15	-20	3.60E-01	2.50E-01	1.60E-01	1.00E-01	6.10E-02	3.30E-02	1.60E-02	7.80E-03	2.80E-03	1.10E-03	3.10E-04	2.70E-04
-35	-40	4.20E-01	2.70E-01	1.60E-01	8.20E-02	4.10E-02	1.80E-02	6.60E-03	1.40E-03	1.20E-03	0.00E+00	0.00E+00	0.00E+00

Table 4 Histograms of f_{hail} : $\int_{Z'}^{Z'+\Delta Z'} f_{hail}(Z)dZ$ for different temperature ranges that can be used in eq. 6.5. The hail threshold reflectivity in this case is 48 dBZ.

7.2.2 Implied hail size distributions

Any measured value of radar reflectivity can be satisfied by a family of N_0 and λ values. By making an assumption about the value of one (λ) each reflectivity value gives rise to a unique pair of parameters to define the size distribution of the hail. Table 5 below shows reflectivity factors, the associated exponential size distribution parameters and the concentration of particles larger than a given size ($N(D>D_0)$) appropriate to that distribution.

			N(D>D0) [m^{-3}]									
			D0 [mm]									
Z [dBZ]	λ [m^{-1}]	N_0 [m^{-4}]	10	20	30	40	50	60	70	80	90	100
45.5	200	1.20E+02	8.10E-02	1.10E-02	1.50E-03	2.00E-04	2.70E-05	3.70E-06	5.00E-07	6.80E-08	9.10E-09	1.20E-09
46.5	200	1.40E+02	9.70E-02	1.30E-02	1.80E-03	2.40E-04	3.30E-05	4.40E-06	6.00E-07	8.10E-08	1.10E-08	1.50E-09
47.5	200	1.70E+02	1.20E-01	1.60E-02	2.10E-03	2.90E-04	3.90E-05	5.30E-06	7.20E-07	9.70E-08	1.30E-08	1.80E-09
48.5	200	2.20E+02	1.50E-01	2.00E-02	2.70E-03	3.70E-04	5.00E-05	6.80E-06	9.20E-07	1.20E-07	1.70E-08	2.30E-09
49.5	200	3.00E+02	2.00E-01	2.70E-02	3.70E-03	5.00E-04	6.80E-05	9.20E-06	1.20E-06	1.70E-07	2.30E-08	3.10E-09
50.5	200	3.60E+02	2.40E-01	3.30E-02	4.40E-03	6.00E-04	8.10E-05	1.10E-05	1.50E-06	2.00E-07	2.70E-08	3.70E-09
51.5	200	4.30E+02	2.90E-01	3.90E-02	5.30E-03	7.20E-04	9.80E-05	1.30E-05	1.80E-06	2.40E-07	3.30E-08	4.40E-09
52.5	200	5.50E+02	3.70E-01	5.10E-02	6.80E-03	9.30E-04	1.30E-04	1.70E-05	2.30E-06	3.10E-07	4.20E-08	5.70E-09
53.5	200	7.40E+02	5.00E-01	6.80E-02	9.20E-03	1.20E-03	1.70E-04	2.30E-05	3.10E-06	4.20E-07	5.70E-08	7.70E-09
54.5	200	8.90E+02	6.00E-01	8.20E-02	1.10E-02	1.50E-03	2.00E-04	2.70E-05	3.70E-06	5.00E-07	6.80E-08	9.20E-09
55.5	200	1.20E+03	8.10E-01	1.10E-01	1.50E-02	2.00E-03	2.70E-04	3.70E-05	5.00E-06	6.80E-07	9.10E-08	1.20E-08
56.5	200	1.40E+03	9.70E-01	1.30E-01	1.80E-02	2.40E-03	3.30E-04	4.40E-05	6.00E-06	8.10E-07	1.10E-07	1.50E-08
57.5	200	1.70E+03	1.20E+00	1.60E-01	2.10E-02	2.90E-03	3.90E-04	5.30E-05	7.20E-06	9.70E-07	1.30E-07	1.80E-08
58.5	200	2.20E+03	1.50E+00	2.00E-01	2.70E-02	3.70E-03	5.00E-04	6.80E-05	9.20E-06	1.20E-06	1.70E-07	2.30E-08
59.5	200	3.00E+03	2.00E+00	2.70E-01	3.70E-02	5.00E-03	6.80E-04	9.20E-05	1.20E-05	1.70E-06	2.30E-07	3.10E-08
60.5	200	3.60E+03	2.40E+00	3.30E-01	4.40E-02	6.00E-03	8.10E-04	1.10E-04	1.50E-05	2.00E-06	2.70E-07	3.70E-08

Table 5 Parameters required to generate observed radar reflectivity. Concentrations of particles larger than a given size, D0, given the exponential distribution parameters.

7.2.3 Probability results

Table 6 shows the probability, $P\left[A \middle| Z' < Z < Z' + \Delta Z' \cap D > D_0\right]$, of intercepting particles of sizes bigger than the given size, D_0, for an aircraft traversing a 5 km region for different reflectivity values representative of hail assuming a forward facing cross section of 50 m^2

	P											
	D0 [mm]											
Z [dBZ]	10	20	30	40	50	60	70	80	90	100	110	120
45.5	1.00E+00	1.00E+00	1.00E+00	1.00E+00	1.00E+00	6.00E-01	1.20E-01	1.70E-02	2.30E-03	3.10E-04	4.20E-05	5.70E-06
46.5	1.00E+00	1.00E+00	1.00E+00	1.00E+00	1.00E+00	6.70E-01	1.40E-01	2.00E-02	2.70E-03	3.70E-04	5.00E-05	6.80E-06
47.5	1.00E+00	1.00E+00	1.00E+00	1.00E+00	1.00E+00	7.30E-01	1.60E-01	2.40E-02	3.30E-03	4.50E-04	6.00E-05	8.20E-06
48.5	1.00E+00	1.00E+00	1.00E+00	1.00E+00	1.00E+00	8.20E-01	2.10E-01	3.10E-02	4.20E-03	5.70E-04	7.70E-05	1.00E-05
49.5	1.00E+00	1.00E+00	1.00E+00	1.00E+00	1.00E+00	9.00E-01	2.70E-01	4.10E-02	5.70E-03	7.70E-04	1.00E-04	1.40E-05
50.5	1.00E+00	1.00E+00	1.00E+00	1.00E+00	1.00E+00	9.40E-01	3.10E-01	4.90E-02	6.80E-03	9.20E-04	1.20E-04	1.70E-05
51.5	1.00E+00	1.00E+00	1.00E+00	1.00E+00	1.00E+00	9.60E-01	3.60E-01	5.90E-02	8.20E-03	1.10E-03	1.50E-04	2.00E-05
52.5	1.00E+00	1.00E+00	1.00E+00	1.00E+00	1.00E+00	9.90E-01	4.40E-01	7.50E-02	1.00E-02	1.40E-03	1.90E-04	2.60E-05
53.5	1.00E+00	1.00E+00	1.00E+00	1.00E+00	1.00E+00	1.00E+00	5.40E-01	9.90E-02	1.40E-02	1.90E-03	2.60E-04	3.50E-05
54.5	1.00E+00	1.00E+00	1.00E+00	1.00E+00	1.00E+00	1.00E+00	6.00E-01	1.20E-01	1.70E-02	2.30E-03	3.10E-04	4.20E-05
55.5	1.00E+00	1.00E+00	1.00E+00	1.00E+00	1.00E+00	1.00E+00	7.10E-01	1.60E-01	2.30E-02	3.10E-03	4.20E-04	5.70E-05
56.5	1.00E+00	1.00E+00	1.00E+00	1.00E+00	1.00E+00	1.00E+00	7.80E-01	1.80E-01	2.70E-02	3.70E-03	5.00E-04	6.80E-05
57.5	1.00E+00	1.00E+00	1.00E+00	1.00E+00	1.00E+00	1.00E+00	8.30E-01	2.20E-01	3.20E-02	4.40E-03	6.00E-04	8.20E-05
58.5	1.00E+00	1.00E+00	1.00E+00	1.00E+00	1.00E+00	1.00E+00	9.00E-01	2.70E-01	4.10E-02	5.70E-03	7.70E-04	1.00E-04
59.5	1.00E+00	1.00E+00	1.00E+00	1.00E+00	1.00E+00	1.00E+00	9.60E-01	3.40E-01	5.50E-02	7.70E-03	1.00E-03	1.40E-04
60.5	1.00E+00	1.00E+00	1.00E+00	1.00E+00	1.00E+00	1.00E+00	9.80E-01	4.00E-01	6.60E-02	9.20E-03	1.20E-03	1.70E-04

Table 6 Probability of intercepting a particle with size ≥ D_0 if an aircraft is travelling through a region of hail with a given radar reflectivity. Width of region=5km. Aircraft cross sectional area= 50 m^2. These probabilities are also appropriate for collisions with the horizontal cross section of the aircraft (assuming 400 m^2, an airspeed of 250 m s^{-1} and hail fallspeed of 40 m s^{-1}.)

This is then combined with the full Z_{dBZ} pdf to obtain the probability of intercepting at least one hailstone of the given size or larger if an aircraft flies randomly through a series of 5km regions within each temperature range (table 7 from eq 6.4). (The full pdf is for land only regions at 16-20 LT, JJA).

Threshold [dBZ]	Tmin [C]	Tmax [C]	D0 10	20	30	40	50	60	70	80	90
45	-2	-5	2.20E-04	2.20E-04	2.20E-04	2.20E-04	2.20E-04	1.60E-04	4.30E-05	6.70E-06	9.30E-07
	-15	-20	4.30E-05	4.30E-05	4.30E-05	4.30E-05	4.30E-05	3.20E-05	7.90E-06	1.20E-06	1.70E-07
	-35	-40	6.00E-06	6.00E-06	6.00E-06	6.00E-06	6.00E-06	4.20E-06	9.80E-07	1.50E-07	2.00E-08
48	-2	-5	8.00E-05	8.00E-05	8.00E-05	8.00E-05	8.00E-05	7.20E-05	2.40E-05	4.00E-06	5.50E-07
	-15	-20	1.40E-05	1.40E-05	1.40E-05	1.40E-05	1.40E-05	1.20E-05	3.90E-06	6.20E-07	8.70E-08
	-35	-40	1.40E-06	1.40E-06	1.40E-06	1.40E-06	1.40E-06	1.30E-06	3.70E-07	5.80E-08	8.10E-09
50	-2	-5	3.40E-05	3.40E-05	3.40E-05	3.40E-05	3.40E-05	3.20E-05	1.30E-05	2.30E-06	3.30E-07
	-15	-20	4.80E-06	4.80E-06	4.80E-06	4.80E-06	4.80E-06	4.70E-06	1.90E-06	3.10E-07	4.40E-08
	-35	-40	3.60E-07	3.60E-07	3.60E-07	3.60E-07	3.60E-07	3.40E-07	1.30E-07	2.10E-08	2.90E-09

Table 7 Probability of intercepting at least one hailstone of the given size, D0 (mm), or larger assuming a cross-sectional area of 50 m^2 and a path length of 5km and random flight over land between 16-20LT in JJA and within the given temperature ranges. The three sets of data are the results for assuming different threshold reflectivities to indicate the presence of hail. Exponential slope parameter, $\lambda=200m^{-1}$.

Probability values decrease with temperature for a given size by about 2 orders of magnitude reflecting the fact that higher reflectivities are observed more frequently at warmer temperatures. Increasing the hail threshold from 45 to 50 dBZ reduces the probability values by about an order of magnitude. Hailstones that are intercepted at approximately the 10^{-5} probability event level are have a diameter of about 70 mm for the -2 to -5C and -15 to -20C temperature ranges, while diameters will be less than 10 mm for the -35 to -40C range. This result is not strongly dependent upon the reflectivity threshold chosen.

Finally, if an aircraft is flying through regions already containing hail (reflectivity exceeds or equals threshold) then the probability of striking at least one hailstone of the given size or greater is given in table 8 (from eq. 6.5). Given that regions of hail are being flown through, varying the Z_{dBZ} threshold from 45 to 50 dBZ does not produce much variability in the probability values. In contrast, changes in the choice of exponential slope parameter can have a large effect of the final probability values. The best estimate of the worst case slope parameter is 200 m^{-1} based on the lowest reported values in the literature. For the 10^{-3} event probability level when flying in hail regions is the diameter of the hail is 100 mm for all temperature ranges.

Threshold [dBZ]	Tmin [C]	Tmax [C]	λ=200 m^{-1} D0 10	20	30	40	50	60	70	80	90	100	110	120
45	-2	-5	1.00E+00	1.00E+00	1.00E+00	1.00E+00	1.00E+00	7.30E-01	1.90E-01	3.00E-02	4.10E-03	5.50E-04	7.50E-05	1.00E-05
	-15	-20	1.00E+00	1.00E+00	1.00E+00	1.00E+00	1.00E+00	7.30E-01	1.90E-01	2.90E-02	3.90E-03	5.40E-04	7.20E-05	9.80E-06
	-35	-40	1.00E+00	1.00E+00	1.00E+00	1.00E+00	1.00E+00	7.10E-01	1.70E-01	2.50E-02	3.50E-03	4.70E-04	6.40E-05	8.70E-06
48	-2	-5	1.00E+00	1.00E+00	1.00E+00	1.00E+00	1.00E+00	9.00E-01	3.00E-01	5.00E-02	7.00E-03	9.50E-04	1.30E-04	1.70E-05
	-15	-20	1.00E+00	1.00E+00	1.00E+00	1.00E+00	1.00E+00	8.90E-01	2.90E-01	4.70E-02	6.60E-03	8.90E-04	1.20E-04	1.60E-05
	-35	-40	1.00E+00	1.00E+00	1.00E+00	1.00E+00	1.00E+00	8.80E-01	2.70E-01	4.30E-02	5.90E-03	8.00E-04	1.10E-04	1.50E-05
50	-2	-5	1.00E+00	1.00E+00	1.00E+00	1.00E+00	1.00E+00	9.60E-01	4.00E-01	7.10E-02	1.00E-02	1.40E-03	1.80E-04	2.50E-05
	-15	-20	1.00E+00	1.00E+00	1.00E+00	1.00E+00	1.00E+00	9.60E-01	3.90E-01	6.70E-02	9.30E-03	1.30E-03	1.70E-04	2.30E-05
	-35	-40	1.00E+00	1.00E+00	1.00E+00	1.00E+00	1.00E+00	9.60E-01	3.60E-01	6.10E-02	8.50E-03	1.10E-03	1.60E-04	2.10E-05
			λ=100 m^{-1}											
48	-2	-5	1.00E+00	1.00E+00	1.00E+00	1.00E+00	1.00E+00	1.00E+00	1.00E+00	1.00E+00	9.70E-01	7.60E-01	4.30E-01	2.00E-01
	-15	-20	1.00E+00	1.00E+00	1.00E+00	1.00E+00	1.00E+00	1.00E+00	1.00E+00	1.00E+00	9.70E-01	7.50E-01	4.20E-01	1.90E-01
	-35	-40	1.00E+00	1.00E+00	1.00E+00	1.00E+00	1.00E+00	1.00E+00	1.00E+00	1.00E+00	9.60E-01	7.30E-01	4.00E-01	1.70E-01
			λ=300 m^{-1}											
48	-2	-5	1.00E+00	1.00E+00	1.00E+00	1.00E+00	5.50E-01	4.30E-02	2.20E-03	1.10E-04	5.50E-06	2.80E-07	2.70E-09	0.00E+00
	-15	-20	1.00E+00	1.00E+00	1.00E+00	1.00E+00	5.40E-01	4.10E-02	2.10E-03	1.00E-04	5.20E-06	2.60E-07	1.70E-09	0.00E+00
	-35	-40	1.00E+00	1.00E+00	1.00E+00	1.00E+00	5.10E-01	3.70E-02	1.90E-03	9.30E-05	4.60E-06	2.40E-07	5.70E-10	0.00E+00

Table 8 Probability of intercepting at least one hailstone of the given size, D0 (mm), or larger assuming a cross-sectional area of 50 m^2, a path length of 5km and only flying in regions of radar reflectivity greater than a threshold for the presence of hail. Results are shown for different temperature ranges, Z_{dBZ} thresholds and exponential slope parameters.

7.2.4 Reflectivity extremes.

An alternative to combining the hail pdf with the probabilities is to consider an extreme value for the reflectivity and then use this to select from table 6 the most appropriate probabilities. Through inspection of fig. 7.11 the reflectivities observed in each temperature range at the 10^{-5} and 10^{-6} occurrence frequency are given in table 9. This again indicates that once the aircraft is assumed to be in hail the diameter of particles at the 10^{-3} probability level will be 100-110 mm.

	10^{-5}	10^{-6}
-2 to -5C	51 dBZ	54 dBZ
-15 to -20C	47	51
-35 to -40C	47	-

Table 9 TRMM radar reflectivities in each temperature range, 16-20LT and JJA for the 10^{-5} and 10^{-6} probability levels.

7.2.5 Multi-strike result

Assuming the exponential distribution parameters given in the table 5, the number of strikes expected for an aircraft with a cross sectional area of 50 m^2 traversing a 5km region with the given reflectivity value is given in table 10. It can be seen that for particles smaller than ~50 mm multiple hits can be expected as a worst case. The number of collisions with 20 mm particles can vary from 1000s to nearly 10^5 across the reflectivity range given in the table.

Estimates of the typical spacing between particles along the leading edge can be made by dividing the values in table 10 by 50 m^2 and taking the square root of the inverse of this value. For example, typical horizontal spacings for 30 mm particles for an aircraft traversing 5 km regions of 47.5 dBZ will be √(50/5.40E+02) = 0.3 m. Similarly, for the horizontal surface in flight the cross sectional area of 400 m^2 is used: √(400/5.40E+02) = 0.86 m.

			Number (D>D0)									
			D0 [mm]									
Z [dBZ]	λ [m^{-1}]	N_0 [m^{-4}]	10	20	30	40	50	60	70	80	90	100
45.5	200	1.20E+02	2.00E+04	2.70E+03	3.70E+02	5.00E+01	6.80E+00	9.20E-01	1.20E-01	1.70E-02	2.30E-03	3.10E-04
46.5	200	1.40E+02	2.40E+04	3.30E+03	4.50E+02	6.00E+01	8.20E+00	1.10E+00	1.50E-01	2.00E-02	2.70E-03	3.70E-04
47.5	200	1.70E+02	2.90E+04	4.00E+03	5.40E+02	7.20E+01	9.80E+00	1.30E+00	1.80E-01	2.40E-02	3.30E-03	4.50E-04
48.5	200	2.20E+02	3.80E+04	5.10E+03	6.90E+02	9.30E+01	1.30E+01	1.70E+00	2.30E-01	3.10E-02	4.20E-03	5.70E-04
49.5	200	3.00E+02	5.10E+04	6.80E+03	9.30E+02	1.30E+02	1.70E+01	2.30E+00	3.10E-01	4.20E-02	5.70E-03	7.70E-04
50.5	200	3.60E+02	6.10E+04	8.20E+03	1.10E+03	1.50E+02	2.00E+01	2.80E+00	3.70E-01	5.00E-02	6.80E-03	9.20E-04
51.5	200	4.30E+02	7.30E+04	9.80E+03	1.30E+03	1.80E+02	2.40E+01	3.30E+00	4.50E-01	6.00E-02	8.20E-03	1.10E-03
52.5	200	5.50E+02	9.30E+04	1.30E+04	1.70E+03	2.30E+02	3.10E+01	4.20E+00	5.70E-01	7.80E-02	1.10E-02	1.40E-03
53.5	200	7.40E+02	1.30E+05	1.70E+04	2.30E+03	3.10E+02	4.20E+01	5.70E+00	7.70E-01	1.00E-01	1.40E-02	1.90E-03
54.5	200	8.90E+02	1.50E+05	2.00E+04	2.80E+03	3.70E+02	5.10E+01	6.80E+00	9.30E-01	1.30E-01	1.70E-02	2.30E-03
55.5	200	1.20E+03	2.00E+05	2.70E+04	3.70E+03	5.00E+02	6.80E+01	9.20E+00	1.20E+00	1.70E-01	2.30E-02	3.10E-03
56.5	200	1.40E+03	2.40E+05	3.30E+04	4.50E+03	6.00E+02	8.20E+01	1.10E+01	1.50E+00	2.00E-01	2.70E-02	3.70E-03
57.5	200	1.70E+03	2.90E+05	4.00E+04	5.40E+03	7.20E+02	9.80E+01	1.30E+01	1.80E+00	2.40E-01	3.30E-02	4.50E-03
58.5	200	2.20E+03	3.80E+05	5.10E+04	6.90E+03	9.30E+02	1.30E+02	1.70E+01	2.30E+00	3.10E-01	4.20E-02	5.70E-03
59.5	200	3.00E+03	5.10E+05	6.80E+04	9.30E+03	1.30E+03	1.70E+02	2.30E+01	3.10E+00	4.20E-01	5.70E-02	7.70E-03
60.5	200	3.60E+03	6.10E+05	8.20E+04	1.10E+04	1.50E+03	2.00E+02	2.80E+01	3.70E+00	5.00E-01	6.80E-02	9.20E-03

Table 10 Number of strikes expected for an aircraft with 50 m^2 forward facing cross sectional area traversing a 5km region with a given reflectivity. This table is table 5 multiplied by the sample volume (5000m x 50 m^2). The highlighted entries indicate greater than 10 hits.

7.2.6 Conditions at the ground

To estimate conditions on the ground it is assumed that the -2 to -5C data is representative of the surface. This assumes that melting and evaporation have little effect on the size distribution. This assumption leads to a worst case estimate. It may be recalled that the CDP approach assumes that all hail melts before reaching the ground if the freezing level is higher than 4400m. Next, an estimate of the sample volume has to be made as a 5km region of hail passes overhead. This sample volume depends upon the ground speed of the storm, the size of the particles and the horizontal cross section of the aircraft. For example, if the storm speed was ~20 m s^{-1} , the mean particle fallspeeds were ~40 m s^{-1} and the aircraft horizontal cross sectional area was ~400 m^2 then the sample volume would be about an order of magnitude larger than that of an aircraft flying through the volume. When table 7 is recomputed for the larger sample volume it increases the probabilities (see table 11). This has the effect of shifting the probabilities in table 7 and 8 to sizes about 10mm larger. Therefore table 12 indicates that 110 mm hail would be encountered at the 10^{-3} event probability level for an aircraft on the ground exposed to hail. Table 12 also includes the probabilities for random weather passing over an aircraft on the ground (the assumption of 20 m s^{-1} advection will not necessarily be appropriate for different weather conditions). Again the random weather pdf is for land, between 16-20 LT and JJA, so this provides the worst case. The hail size at the 10^{-5} level is 110 mm for this case.

The number of multiple strikes in table 10 would also increase by an order of magnitude.

Z [dBZ]	D0 [mm] 10	20	30	40	50	60	70	80	90	100	110	120
45.5	1.00E+00	1.00E+00	1.00E+00	1.00E+00	1.00E+00	1.00E+00	8.60E-01	2.40E-01	3.60E-02	4.90E-03	6.70E-04	9.10E-05
46.5	1.00E+00	1.00E+00	1.00E+00	1.00E+00	1.00E+00	1.00E+00	9.10E-01	2.80E-01	4.30E-02	5.90E-03	8.00E-04	1.10E-04
47.5	1.00E+00	1.00E+00	1.00E+00	1.00E+00	1.00E+00	1.00E+00	9.40E-01	3.20E-01	5.10E-02	7.10E-03	9.60E-04	1.30E-04
48.5	1.00E+00	1.00E+00	1.00E+00	1.00E+00	1.00E+00	1.00E+00	9.80E-01	3.90E-01	6.50E-02	9.10E-03	1.20E-03	1.70E-04
49.5	1.00E+00	1.00E+00	1.00E+00	1.00E+00	1.00E+00	1.00E+00	9.90E-01	4.90E-01	8.70E-02	1.20E-02	1.70E-03	2.30E-04
50.5	1.00E+00	1.00E+00	1.00E+00	1.00E+00	1.00E+00	1.00E+00	1.00E+00	5.50E-01	1.00E-01	1.50E-02	2.00E-03	2.70E-04
51.5	1.00E+00	1.00E+00	1.00E+00	1.00E+00	1.00E+00	1.00E+00	1.00E+00	6.20E-01	1.20E-01	1.80E-02	2.40E-03	3.20E-04
52.5	1.00E+00	1.00E+00	1.00E+00	1.00E+00	1.00E+00	1.00E+00	1.00E+00	7.10E-01	1.50E-01	2.30E-02	3.10E-03	4.20E-04
53.5	1.00E+00	1.00E+00	1.00E+00	1.00E+00	1.00E+00	1.00E+00	1.00E+00	8.10E-01	2.00E-01	3.00E-02	4.10E-03	5.60E-04
54.5	1.00E+00	1.00E+00	1.00E+00	1.00E+00	1.00E+00	1.00E+00	1.00E+00	8.70E-01	2.40E-01	3.60E-02	5.00E-03	6.70E-04
55.5	1.00E+00	1.00E+00	1.00E+00	1.00E+00	1.00E+00	1.00E+00	1.00E+00	9.30E-01	3.10E-01	4.80E-02	6.70E-03	9.10E-04
56.5	1.00E+00	1.00E+00	1.00E+00	1.00E+00	1.00E+00	1.00E+00	1.00E+00	9.60E-01	3.60E-01	5.80E-02	8.00E-03	1.10E-03
57.5	1.00E+00	1.00E+00	1.00E+00	1.00E+00	1.00E+00	1.00E+00	1.00E+00	9.80E-01	4.10E-01	6.90E-02	9.60E-03	1.30E-03
58.5	1.00E+00	1.00E+00	1.00E+00	1.00E+00	1.00E+00	1.00E+00	1.00E+00	9.90E-01	4.90E-01	8.70E-02	1.20E-02	1.70E-03
59.5	1.00E+00	1.00E+00	1.00E+00	1.00E+00	1.00E+00	1.00E+00	1.00E+00	1.00E+00	6.00E-01	1.20E-01	1.70E-02	2.30E-03
60.5	1.00E+00	1.00E+00	1.00E+00	1.00E+00	1.00E+00	1.00E+00	1.00E+00	1.00E+00	6.60E-01	1.40E-01	2.00E-02	2.70E-03

Table 11 Probability of intercepting a particle with size ≥ D_0 if an aircraft is on the ground when a region of hail with a given radar reflectivity passes overhead. Width of region=5km. Aircraft cross sectional area= 400 m^2, hail fallspeed of 40 m s^{-1} and a storm advection speed of 20 m s^{-1}.

Threshold [dBZ]		λ=200 m^{-1} D0 10	20	30	40	50	60	70	80	90	100	110	120
48	In hail	1.00E+00	1.00E+00	1.00E+00	1.00E+00	1.00E+00	1.00E+00	9.90E-01	5.30E-01	1.00E-01	1.50E-02	2.10E-03	2.80E-04
	Random	8.00E-05	8.00E-05	8.00E-05	8.00E-05	8.00E-05	8.00E-05	7.90E-05	4.20E-05	8.30E-06	1.20E-06	1.60E-07	2.20E-08

Table 12 Probability of intercepting at least one hailstone of the given size, D0 (mm), or larger when regions of radar reflectivity greater than a threshold for the presence of hail pass overhead an aircraft on the ground (In hail), and for random 'weather' (Random). Width of region=5km. Aircraft horizontal cross sectional area= 400 m^2, hail fallspeed of 40 m s^{-1} and a storm (or weather) advection speed of 20 m s^{-1}.

8 Aviation Component: Literature Review

8.1 Increasing usage of composites in aircraft structures

There has been a progressive increase in the use of polymer composites in aircraft structures over the last 30 years but several factors have led to a more significant increase in composite usage more recently. These factors include: advancements in automated and low cost manufacturing techniques for composites; improvements in designers' knowledge of how to optimise composite structures; lower part-count and improved corrosion resistance, as well as a continually increasing drive for mass reduction due to environmental concerns and airline operator pressure to reduce prices per passenger mile. This change in composites usage is illustrated in fig. 8.1 below which shows the recent increase in the uptake of composites in Airbus aircraft (Buckley 2007).

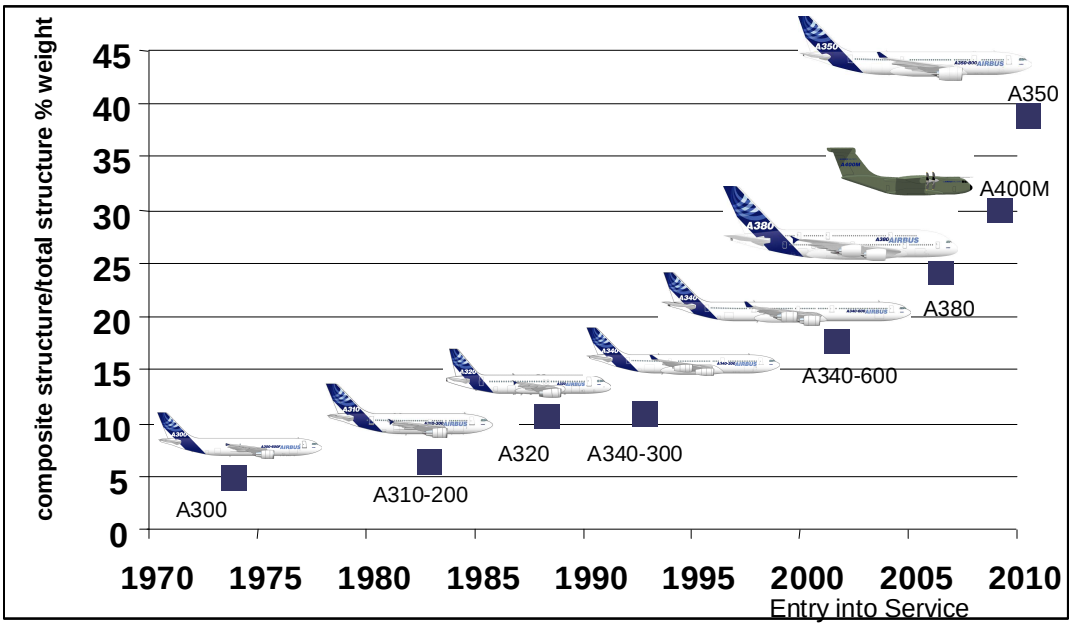

Figure 8.1 Increasing composite usage in Airbus Aircraft (Buckley 2007)

A similar trend can be seen for both Boeing and Airbus aircraft (see fig. 8.2). These trends look set to continue more generally within the civil aviation sector, with some forecasters predicting growth in carbon fibre demand from 5100 tonnes in 2008, to 13,443 tonnes by 2014 (Roberts, 2008).

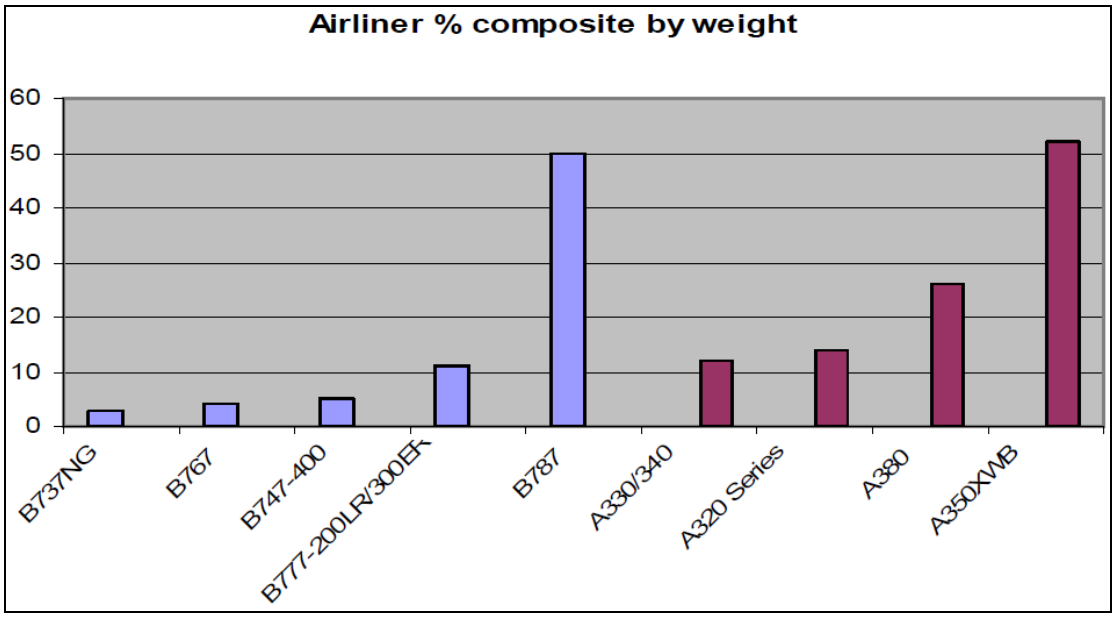

Figure 8.2 Comparison of composite usage in Boeing (blue) and Airbus (red) aircraft

The increased usage of advanced composite materials in aircraft structures is not restricted to the two largest original equipment manufacturers (OEMs), Airbus and Boeing. Other major civil passenger aircraft

OEMs such as Bombardier, Hawker Beechcraft (formerly Raytheon), Embraer and ATR (Avions de Transport Regional) are all increasing their usage of composite in current and future aircraft.

8.2 Types of composite aircraft structure exposed to hail impact threat

As discussed above, the increased use of composites in aircraft offers significant benefits for airline operators and their customers alike. However, the increased prevalence of composites does mean that there is a significant increase in the likelihood of these materials being exposed to impact threats from hail events. Thus, it is important to consider the types of composite structures currently in-service, and those which may be introduced in the future, in order to consider how these structures will behave when subject to hail impact. The second part of this question will be answered later in this report, when structural components will be analysed against typical hail threats. This section of the report therefore focuses on a range of typical aerospace composite components which may be exposed to the threat of impact due to hail.

The range of composite structures currently deployed in civil aircraft is now vast. This is illustrated by fig. 8.3 which shows how the use of composites has moved from initially being focused on secondary and tertiary structures, such as fairings, to current applications where very large primary structures, weighing several hundred kilograms (e.g. centre wing boxes), are now routinely flown in service.

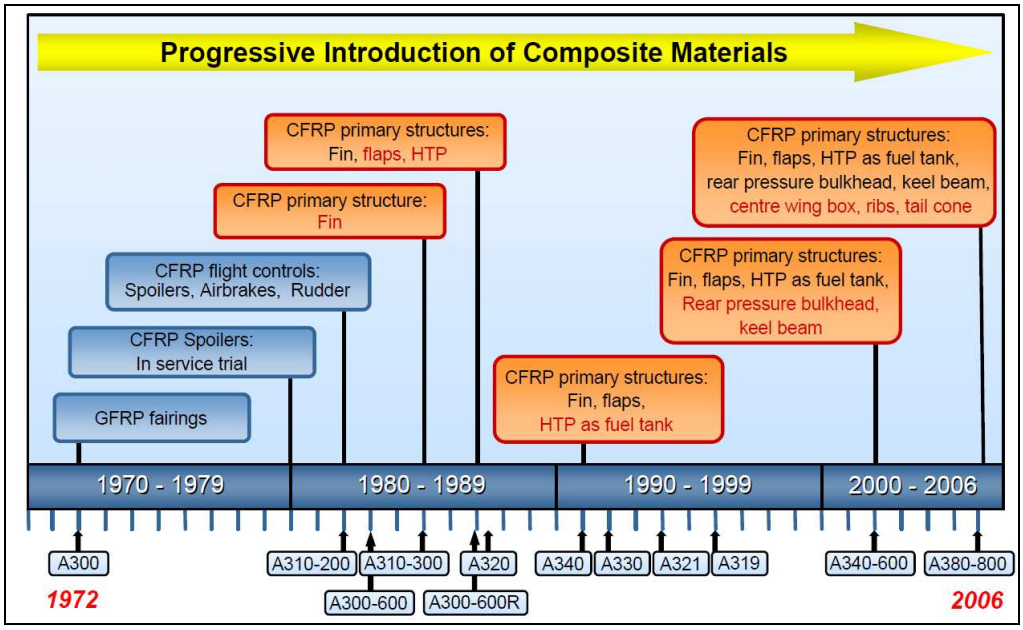

Figure 8.3 The development of composites components in Airbus aircraft (Ferguson 2004)

In order to illustrate the types of aircraft composite structures which may be subject to a hail impact threat, the following sections review relevant components by major civil aircraft manufacturer.

8.2.1 Airbus

Airbus A380

Figure 8.4 illustrates the major external composite components of the Airbus A380 which may be subject to hail impact threats, ranging from the upper fuselage section, which is manufactured from a glass fibre / aluminium laminated material (GLARE), to spoilers, flaps, ailerons and elevators which are all manufactured from carbon fibre reinforced plastic (CFRP). Forward facing structures like the wing leading edges and the radome are also manufactured from composite materials.

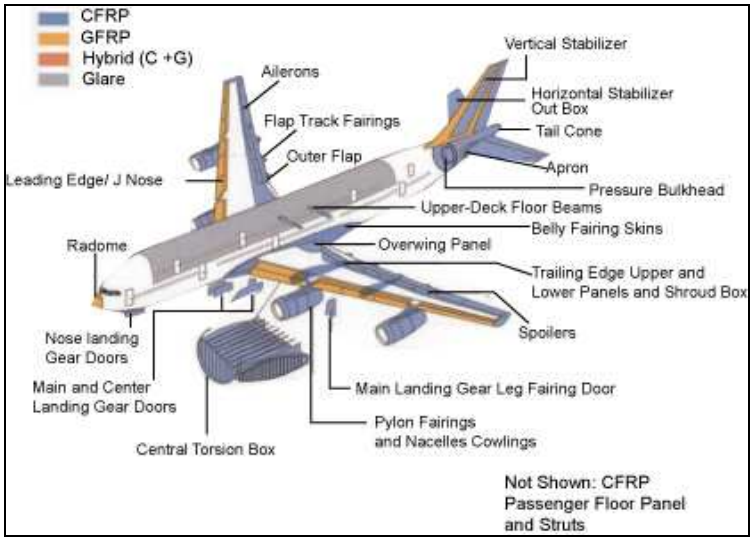

Figure 8.4 The use of composite materials in the Airbus A380 aircraft (Ferguson 2004)

Thermoplastic composites make up fully two-thirds of the A380's fixed leading edge; the structure is manufactured from glass fibre / polyphenylene sulphide (PPS) and has a surface area of 55m^2 running from each wing's inboard engine to its wingtip.

Figure 8.5 Airbus A380 wing leading edge (http://www.airliners.net/photo/Singapore-Airlines/Airbus-A380-841/1289753/L/&tbl=&photo_nr=23&sok=&sort=&prev_id=1289754&next_id=1289752)

Airbus A320/319/330

Figure 8.6 and fig. 8.7 illustrate the plethora of composite components which make up the external surfaces of the Airbus A320, A319 and A330. It can be seen that the engine cowls, spoilers, flaps, ailerons and tail surfaces are all potentially exposed to the threat from hail impact. Forward facing structures like the radome, tailplane and fin leading edges are perhaps the most susceptible to hail damage.

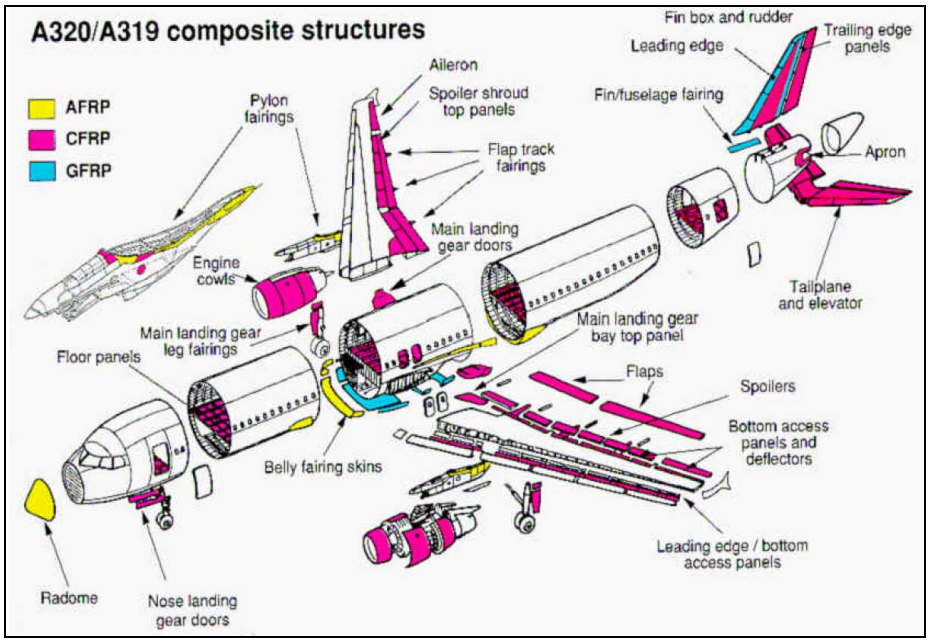

Figure 8.6 Airbus A320/A319 composite usage

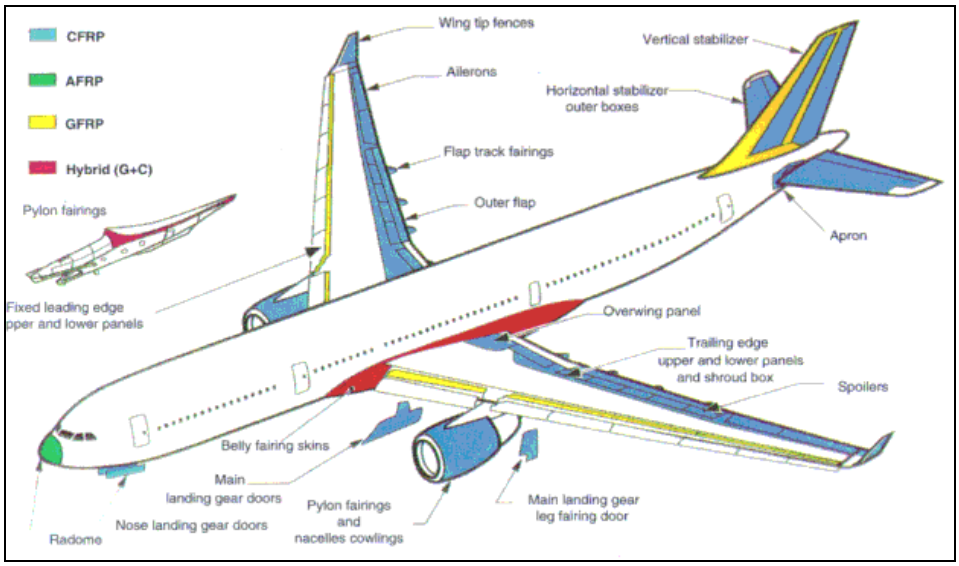

Figure 8.7 Airbus A330 composite usage

Airbus A350XWB

Airbus' development and future introduction of the A350XWB will represent a step change in their usage of composite materials in aircraft structures; it is currently anticipated that the aircraft will deploy composites in over 50% of its structural mass.

In addition to an all composite wing, including upper and lower external wing skin surfaces, for the first time, Airbus will deliver an aircraft which utilises composites extensively in the fuselage construction. Construction of the A350XWB's fuselage sections will be made by assembling four-skin panel sections – two lateral side panels, one at the crown, and another for the belly – onto composite structural frames. Two fuselage demonstrators have been assembled and photographs released by Airbus show the proposed construction of the fuselage panels ('Airbus set to roll out carbon fibre A350 fuselage demonstrator' Flight International 22/05/08), see fig. 8.8.

Figure 8.8 Airbus manufactured composite fuselage panels for A350XWB (Flight International, 22/05/08)

8.2.2 Boeing

Boeing 777

Approximately 12% of the structural weight of the Boeing 777 is made up of composite materials, with the majority of that mass being contained within the 777's empennage (i.e. horizontal and vertical stabilisers, elevators and rudder). The stabiliser is a two-cell box, consisting of a main structural box and an auxiliary or forward torque box, leading edges, tip and fixed trailing edges. The main torque boxes are made from CFRP composite material: solid-laminate front and rear spars, honeycomb sandwich ribs and integrally stiffened laminate skin panels.

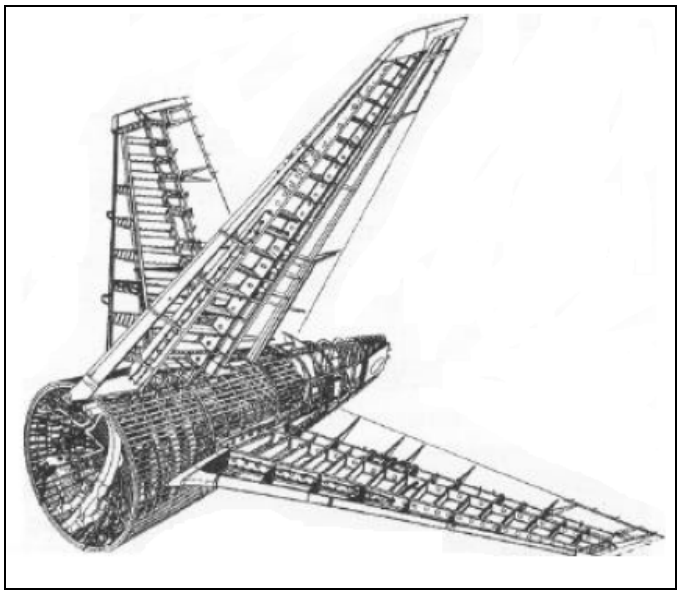

Figure 8.9 Boeing 777 Empennage without surface panels (Fawcett et al. 1997)

The main box panels and spars feature a toughened-matrix CFRP material from Toray. The pre-impregnated fibre/resin system is T800/3900-2. The auxiliary torque box and fixed trailing edges are glass reinforced plastic (GRP) or GRP/CFRP sandwich panels with aluminium ribs. The leading edge, tip and auxiliary spar are aluminium construction.

The elevator and rudder are also constructed from CFRP sandwich panels, ribs and spars and are hinged from the stabiliser or fin fixed trailing edge. The rudder incorporates a lower tab of CFRP sandwich construction.

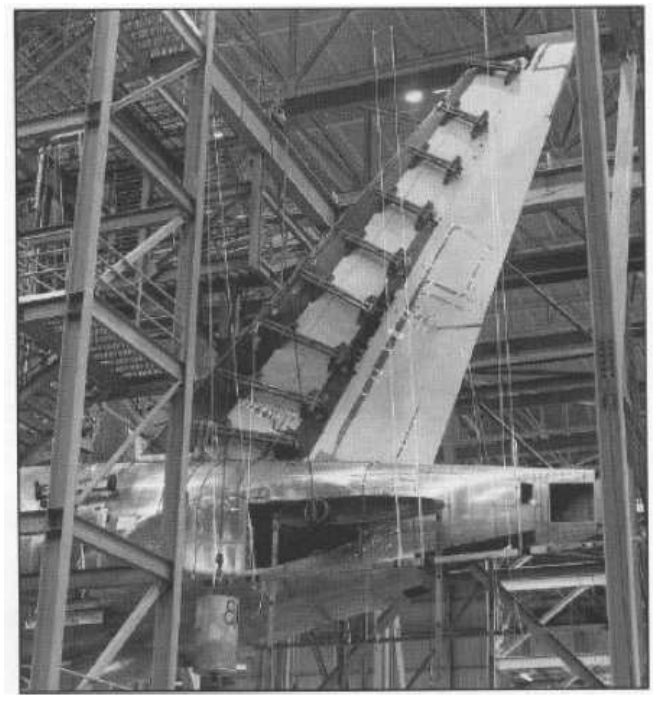

Figure 8.10 Boeing 777 empennage under test (Fawcett et al. 1997)

Boeing 787 Dreamliner

Boeing's new 'Dreamliner', the 787, will become the first full-size commercial aircraft to utilise composite wings and fuselage, with composites accounting for 50% of the aircraft's structural weight. It can be seen in fig. 8.11 below, that composite materials now completely dominate the external surfaces of the aircraft, implying that the likelihood of hail impact threats onto composites structures is higher than ever before.

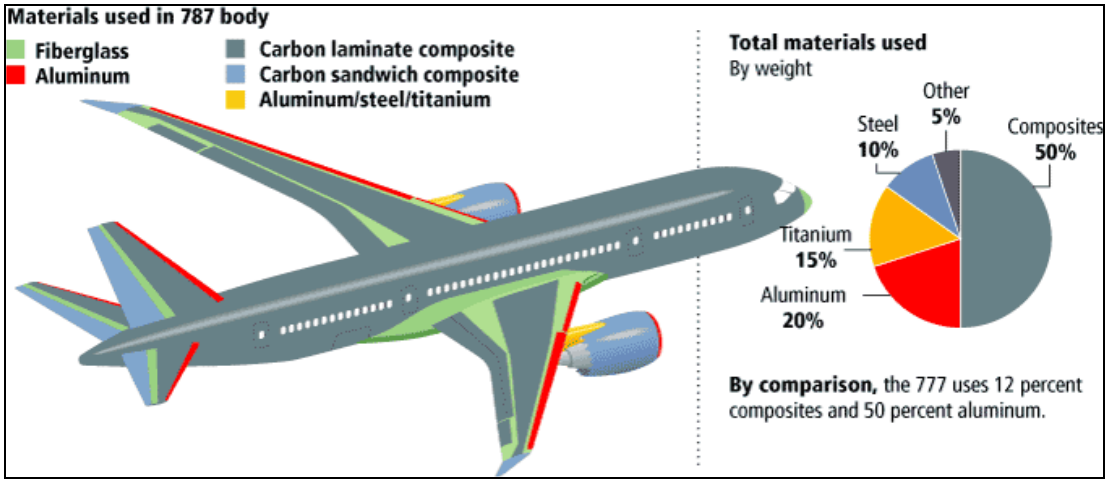

Figure 8.11 Composite materials usage in the Boeing 787

The material being used for the 787's primary structure, such as the wings and fuselage, is a redevelopment of the Toray Composites 3900-2 pre-preg material, comprised of intermediate-modulus T800 carbon fibre and a toughened 350℉-cure epoxy.

The fuselage is being manufactured via computerised lay-down of composite tape on a cylinder-shaped mandrel that is rotated as the tape is applied (see fig. 8.12). After wrapping, the part is cured in an autoclave. The hat-sectioned longitudinal stringers are co-cured with the fuselage skins, being placed in the mandrel before the fuselage outer skin's solid laminate is tape layed. Application of RFI (Resin Film Infusion) is planned for the movable trailing and leading edges on the wing and for fuselage frames.

Figure 8.12 787 Dreamliner fuselage under construction (Boeing Blog. http://boeingblogs.com/randy/archives/2007/03/dreamlifting.html)

Engine fan cases on General Electric's GEnx jet engine, one of the two power plants that will be available to customers for the 787, are also made from composite materials, using an infusion process. This first use of an all-composite structure to contain fan blade failure represents a significant weight savings (Griffiths, 2005).

The Boeing 787 wing leading edge is made of 18 layers of glass-fibre/epoxy resin composite. For extra strength, the edges and areas where the attaching screws are positioned are reinforced with a layer of carbon-fibre composite. The outer surface is fitted with an aluminium erosion shield.

8.2.3 Hawker Beechcraft (formerly Raytheon)

The US FAA granted the Hawker 4000 type certification in December 2004 and, following a series of modifications, the first production Hawker 4000 was delivered in June 2008. The Hawker 4000, as well as the companies Premier I and Premier II commercial jets, features an all-composite fuselage manufactured using a computer numerical controlled (CNC) Carbon Fibre Tape Placement System that was developed by Cincinnati Milacron (see fig. 8.13). This system has allowed Hawker Beechcraft to reduce the fuselage assembly into two main pieces, forward and aft sections, as well as reducing fuselage wall thickness from 3 to 0.81 inches due to the change from an aluminium structure to composite design. Because of the CNC machine's capabilities, designers were able to use a sandwich of inner and outer carbon fibres around a honeycomb core to fabricate the fuselage walls. This design results in almost 60% more cabin volume and significant weight saving.

Figure 8.13 Hawker Beechcraft 4000 fuselage under construction

8.2.4 Avions de Transport Regional (ATR)

The ATR42 is one of a family of twin turboprop passenger aircraft developed and manufactured by Avions de Transport Regional (ATR). Most notably, the ATR42 was the first airliner to have a composite wing. More generally, the ATR family utilises composite materials such as carbon fibre reinforced monolithic structure, carbon / Nomex sandwich and Kevlar / Nomex sandwich, leading to approximately 19% of the total weight of the aircraft structure (for the ATR42-500).

8.2.5 Bombardier

Bombardier's C-Series aircraft is a family of aircraft specifically designed for the 110 to 130 seat market with an expected entry into service (EIS) date of 2013. It is predicted that about 46% (by weight) of the aircraft will be of composite construction, with composite structures currently being developed for use in the centre and rear sections of the fuselage, the tail cone, empennage and wings.

8.2.6 Embraer

The most recent example of Embraer’s use of composites in its aircraft is exemplified by the Phenom 100, a very light jet, which was certified by the Federal Aviation Administration (FAA) on December 12, 2008. The aircraft utilises a high percentage of composite materials in its construction – estimated as 20% carbon fibre composite by weight. Composites are included in the tail structure (a first for Embraer's jets), rear pressure bulkhead, the control surfaces, nose and belly fairings, and dorsal fin.

8.3 Hail impact on composite structures

8.3.1 GARTEUR Action Group 30

The most significant recent research activity completed in Europe has been completed by the GARTEUR Action Group 30 consortium. A thorough review of the work completed will be completed once agreement has been secured from the partners regarding open release of the data, however, in summary, AG30 has been undertaking a number of fundamental tests to gain a greater understanding of the mechanical properties of ice at different temperatures and the behaviour of ice under impact to more closely define the threat it poses to aircraft.

Evidence shows that ice exhibits a clear strain rate effect behaving in a ductile manner at low strain rates whereas at higher strain rates the mechanical behaviour becomes much more brittle. The temperature of the ice during the impact event is critical. In addition a range of ice impact tests have been performed on both carbon and glass composite panels to determine the type (modes) and extent of damage that is generated. Composites are particularly susceptible to damage when loaded out-of-plane, such as in the case of ice impacts, and often the damage sustained is barely visible, existing in the form of subsurface matrix cracks, back face fibre failure and delaminations between the different plies. In carrying out these tests the group has been able to develop new test procedures to help ensure adequate quality, consistency and repeatability in the ice projectile is attained (Willows 2007).

8.3.2 Open literature

In addition to the GARTEUR work mentioned above, other research groups have published in the open literature on the subject of hail impact and composite structures. Hence, this section of the report highlights and reviews a number of relevant research papers. Combining the review's findings with the hail threat work being completed by the Met Office is useful in defining future research requirements in this field, and thus, in turn, facilitating the production of data required to develop future airworthiness standards specific to the problem of hail impact on aircraft composite structures.

An investigation, in 1998, by a team of researchers from North Dakota State University compared impacts onto composite materials using aluminium and ice impactors of equivalent size and energy (Mahinfalah and Skordahl, 1998). Sixteen-ply coupons, manufactured from intermediate modulus carbon fibres and 'industrial grade' epoxy, were subjected to simulated hail impact by ice balls of 25.4 mm (1 in) or 38.1 mm (1.5 in) diameter. Upon impact, the 25.4mm diameter ice ball possessed 7.1 J of kinetic energy, while the 38.1mm diameter ice ball possessed a kinetic energy of 27.4 J. For further comparison, additional coupons were impacted with a 12.7 mm diameter aluminium sphere with either 7.1 or 27.4 J of kinetic energy. Inspection revealed that neither ice ball impact event caused any internal damage, while each aluminium sphere impact

caused delaminations within each coupon. The 7.1 J aluminium sphere impact caused a circular area of delamination about 37 mm in diameter, extending from a depth of 15% to 100% of the laminate thickness. The 27.4 J aluminium impact caused extensive delaminations, ranging from 50 to 62 mm diameter. After being impacted and inspected, each coupon was subjected to constant amplitude tension-tension fatigue. It was determined that neither the 25.4 mm diameter ice ball impact nor the 38.1mm diameter ice ball impact affected the fatigue performance of this particular laminate. The 7.1J aluminium sphere impact also did not affect this laminate, while the 27.4J aluminium impact did adversely affect the fatigue performance of this material. Although the relative size of the hail and aluminium indenters is such that the aluminium impactor imparts its energy over a smaller area, the dramatic increase in damage area does illustrate the potential severity of using rigid metallic impactors to simulate hail events.

Kim and Kedward (2000) performed numerical analysis then compared their results with physical test data produced by Kim et al (2002), in order to predict the damage caused by hail impact on carbon/epoxy composite panels. A Finite Element model was created to simulate hail strikes, with a large portion of the work focused on accurate re-creation of hail. Comparison was then made with test data which was gathered by firing ice balls from a Nitrogen gas cannon at composite test specimens some of which were under load. Tests were run over a range of 10 – 200m/s. It was seen that the severity of the impact does not always increase with the threat and that the structure will respond differently to damage depending on its loading. A progression of failure modes was seen starting with delamination (fig. 8.14).

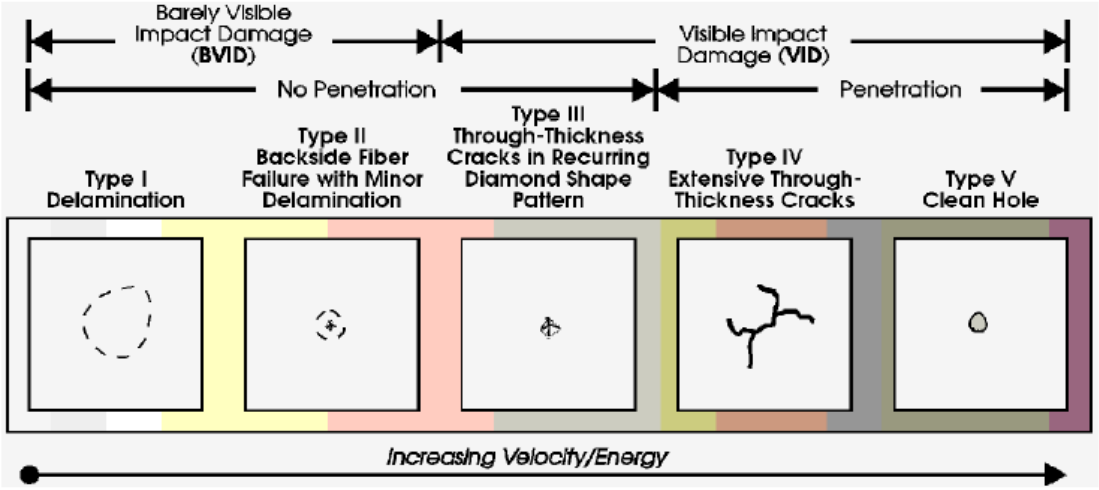

Figure 8.14 Change in damage to composite test specimen due to increased impact energy (Kim and Kedward 2000)

Glancing impacts were also analysed and showed the same linear relationship between increasing damage and increasing energy. These angled impacts were treated as a normal impact, with the force equal to that of the normal component of the total angled force. The simulation model was shown to be accurate for prediction of the peak forces and pulse shapes.

QinetiQ has conducted research in the field of hail impact and in particular for military aircraft structures. Foreman (2003) reported how the threat posed by hail strike may not be accommodated by current design and military airworthiness requirements. For example, the current requirements do not consider the potential for multiple damaging hail impacts during a storm. In addition, consideration needs to be given to a combined and more severe loadcase which could occur if the aircraft is struck during climb or other manoeuvres where impact is coupled with structural loading. Despite this, given the damage characteristics of the materials in questions, it was concluded that hail impact damage would be predominantly visible and thus readily detectable. The primary structures under threat were also shown to be reinforced due to other requirements such as the need to withstand bird strike on leading edges.

Asp and Juntikka (2009) compared two Olsson models and experimental data from ice impact onto composite plates. Ice spheres and small granite stones were fired from a gas gun at panels manufactured using non-crimp fabric reinforced epoxy composites. The impacts were recorded and analysed using a high-speed camera. The results showed that the ice and granite could not be modelled as solid bodies due to the nature of the failure modes present at impact. The ice and granite stone tested were seen to crumble on impact and cause minimal if no damage, as illustrated in Figure 8.15. The authors also stated that the resultant impact damage would be likely considerably higher if the projectile behaved like a solid body, this is confirmed by Mahinfalah and Skordahl (1998).

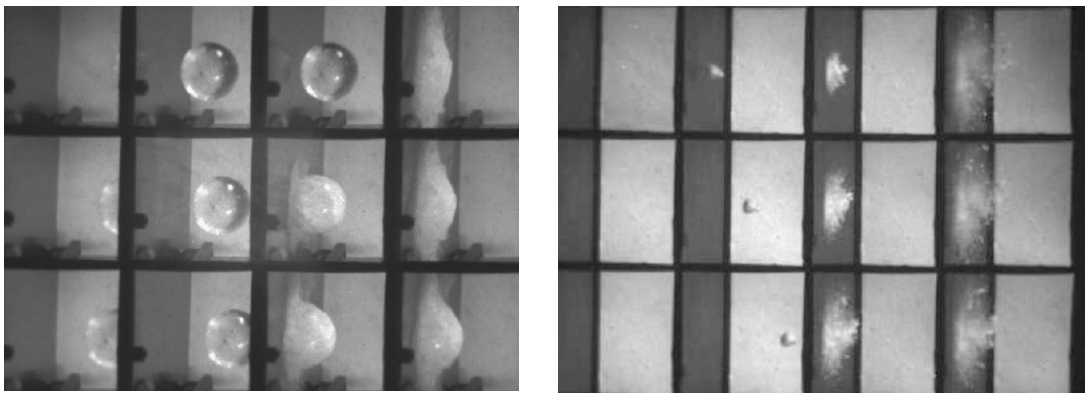

(a) Typical impact of a 25mm ice sphere (impact velocity 96 m/s)

(b) Composite plate impact with 0.32g stone (impact velocity 175m/s)

Figure 8.15 Impactor deformation during high velocity impact onto NCF plate

Das et al (2009) developed a method to assess and analyse hail damage, then quantify the residual strength of the composite. This then lead to an in-service method for selecting the best repair type and procedure. To assess damaged panels, new triangular shell elements were created for a finite element model. These were able to represent the varying properties through the thickness of a sandwich composite. A ‘dummy’ material of reduced strength was added to the outer surface to represent the impacted area. With these elements, a complete stress and strain field analysis of the damaged area could be created. Slits, dents and punctures were analysed under tension to validate the model over a range of situations. Experimental data was then compared against the computer meshed shell model, as well as a traditional solid element model, and was seen to be credible.

8.4 Review of damage tolerance

8.4.1 Introduction

Undoubtedly the analysis of weather patterns reduces the occurrence of flight routes intersecting hailstorm regions, but sometimes passage through a hailstorm is inevitable and thus it is mandatory that aircraft structures can sustain a certain damage tolerance level to hail impact. A specified degree of functionality must be guaranteed after the aircraft has been impacted by a number of hailstones.

Observation of damaged aircraft and experimental tests have shown that the extent of hail impact damage depends upon the properties of both the hailstone (mass, velocity and impact angle), and the geometry and material of the structure being impacted (Anghileri 2005). Also the effect of an impact may be different if the component is loaded primarily in compression or in tension. The damage generated also depends upon the intensity/coverage of hail falls. Damage from multiple impacts is related to the density or number of hailstones falling over a specified area, the maximum and/or average hail size and the wind gusts (or associated heavy rainfall and down drafts) that can accelerate falling hailstones, further increasing the amount of damage generated (Hohl 2002). However, the extent of hail damage has been shown to be more highly correlated with maximum hailstone sizes than with numbers of hailstones per surface area, such that often there is a minimum hailstone size required before any significant damage is sustained.

The Climatology data generated within this programme by the Met Office has identified typical hailstones sizes, densities, masses and impact velocities. Subsequently this information has been combined with an understanding probability of occurrence, to characterise a number of potential threats.

The following sections of the report investigate the effect that a range of probable hail events could have on aircraft materials and structures, manufactured using composite materials, such as those identified previously in Section 8.1.

In general terms, aircraft that are stationary on the ground are subject to perpendicular hail impacts from above, whereas, for aircraft in flight, higher velocity impacts usually occur to forward facing structures, such as the nose and wing leading edges, whilst the top skins experience relatively low impact velocities. If only the velocity vectors are considered, then the worst case is normal impact to the front facing sections of the aircraft during horizontal flight when aircraft speeds reach their maximum, as the vertical component from falling hailstones is comparatively minor . Primarily due to stringent bird strike requirements, these forward facing structures are very tough and research has shown them to be sufficiently damage tolerant to hail impact. However, if an aircraft starts to climb at an angle during a hailstorm, then the vertical component of the aircraft velocity begins to contribute more to the hail impact velocity (ignoring the effects of up and down draughts). Glancing impacts have been found to act as normal impacts with an effective velocity equal to the

normal component of the projectile's true velocity (Kim 1999). Most in-flight impacts are of a glancing nature. There may be a possibility that an aircraft that is climbing may be subject to more severe hail impact loads, particularly when considering the upper wing skins which will not generally be required to be as damage tolerant as the lower wing surfaces. This could give rise to an impact velocity of around 200ms^{-1} on the top skins which would clearly result in severe damage.

8.4.2 The complex behavioural response of composites

Laminated polymer composites have found widespread use in the design of aerospace structures. While these materials offer excellent in-plane performance, they are susceptible to damage when severely loaded out-of-plane, (e.g. in a perpendicular direction during impact). Often the damage relating to these impacts is difficult to detect, forming *Barely Visible Impact Damage (BVID)*, which exists in the form of subsurface matrix cracks, back face fibre failure and delaminations. The latter two damage forms can significantly degrade a structure's performance (Kim 1999).

For example, a low speed impact will overstress the matrix material, producing local sub-critical cracking (micro-cracking). This does not necessarily produce gross fracture, but it will result in load redistribution and the concentration of energy and stress at the inter-ply regions where large differences in material stiffness exist. These conditions are ideal for a fracture-based inter-ply delamination to initiate and grow. The interlaminar shear stress peaks at a time well in advance of the time needed to develop maximum bending strain on the surface of the plate, and hence delamination occurs first (Kim 2000). The onset and rapid propagation of a crack, results in sudden variations in both section properties and load paths within the composite local to the impactor.

Experimental studies have shown that smaller diameter, higher velocity ice projectiles produce higher interlaminar shear stress and bending strain in less time. Thus an *impact by a smaller diameter sphere is often considered to be more severe* (more aggressive in the initiation of damage) *than an equivalent energy impact involving a larger diameter sphere* (fired at lower velocity to achieve the same kinetic energy) (Kim 2000). This is because the impact force is more localised on the target for a smaller sized projectile. In general, for normal impacts, the peak force varies linearly with the projectile kinetic energy. It is expected that this linear relationship is valid for all high velocity ice projectile impacts, regardless of the projectile size, onto any target real structure, assuming that similar ice failure modes result (i.e. localised crushing). The peak force increases significantly with projectile velocity. However, the time to achieve peak force does not vary significantly but is slightly shorter for the higher velocity cases (Kim 2003).

However, it is important to note that *the severity of damage does not always increase with a higher impact velocity*. A higher velocity impact could result in limited fibre failure within one ply only at the back face and minor delamination, which may be more acceptable in some structural applications than a lower velocity impact which causes extensive delamination. Thus, studying failure mode progression over a range of impact velocities is important. Often structural validation tests are performed at a single impact velocity only,

which is based on the maximum perceived threat. This standard approach, often applied in industry, could potentially miss some failure modes in composites that are excited by slightly lower impact velocities but which may generate more severe damage (Kim 1999).

The effect of temperature on the response of the composite structure to ice impact may also be important, as discussed below; the typical operating range for aircraft undercarriage and lower skins is -50ºC to +100ºC and impact could occur at any temperature in this range.

8.4.3 Variation in ice properties during impact

The factors which influence ice formation and its crystalline structure will also have a strong influence on its mechanical properties and hence its ability to generate damage. When considering temperature effects, artificially manufactured ice, as used in experimental testing, tends to exhibit a plastic response at temperatures close to 0^0C and a brittle failure at temperatures below -15^0C. Regarding impact, the influence of ice temperature and strain rate on the failure stress is important and this is well documented by Mills and Hallam (1988).

Ice also exhibits a strong strain rate dependency, thus when increasing from low to high strain rates the mechanical behaviour of ice similarly undergoes a ductile to brittle transition, but for rates above 10^{-2} s^{-1} there is a brittle failure region in which the strength properties are largely independent of loading rate. The axial compression strength of ice increases with strain rate and the tensile strength is much lower than the compressive strength at strain rates greater than 10^{-5} s^{-1}. In addition, it has been reported that the compressive strength of ice increases dramatically as the temperature decreases from -10 to -50^oC. Investigations measuring the adiabatic shock Hugoniot (pressure-volume relationship) of ice on impact have shown that an extremely large pressure of 23.5GPa is required to cause a phase change from a solid to liquid state. However, with ice projectiles there is insufficient confinement to allow such a large build up of pressure, and hence the ice does not undergo a phase change during impact (Kim 2003).

8.4.4 Ice impact testing

Ice impact tests are expensive and notoriously difficult to perform. The GARTEUR consortium under AG30 has been developing suitable testing methods and has performed a number of ice impact tests to further the understanding of its behaviour under load and impact. Some of this work is summarised below.

8.4.5 Mechanical ice impact tests

Since it is so difficult to obtain real hailstones for testing, an ice fabrication procedure has been developed to minimise the formation of microcracks that are generated by internal stresses developing within the ice as it forms. Ice cylinders are best fabricated in flexible moulds that allow some unconstrained lateral expansion/contraction during freezing, which is performed at -22^{0}C, to minimise the amount of microcracking generated.

Ice which is white in colour contains numerous voids and microcracks, and if loaded into a gas gun and fired, it would fragment prematurely in the gun barrel. Often just moving the ice projectile from the freezer into room temperature causes it to crack. A good ice impactor consists of 'clear' ice which contains many less micro-crystals but its modulus and failure mode are still sensitive to temperature.

The ice needs to be protected as it travels down the gun barrel so that it is not damaged prior to impacting the target. One method is to place the ice projectile in a low density open cell foam sabot which can be caught at the end of the barrel, leaving the ice to impact the target unrestrained. Since the mechanical properties of the ice are highly dependent upon temperature the ice must be launched at a consistent temperature e.g. -17^{o}C with only minor variations of plus or minus 1 degree allowed. This can be achieved by firing the gun within a *few minutes* of removing the ice from the freezer.

To be able to define the behaviour of the ice more clearly, a series of mechanical tests were performed on ice cylinders (of length 80mm and diameter 39mm) at temperatures in the range -5^{o}C to -30^{o}C (Figure 8.16) (Johnson 2006). Approximately 25 cylinders were loaded axially by compression under quasi-static conditions. The ice cylinders were tested under displacement control at a constant cross-head speed of 200mm/min (an effective strain rate of 1.8x10^{-2} s^{-1}).

Figure 8.16 Mounted ice cylinder test specimen

On impact, hailstones essentially fail by compression crushing. Most of the test specimens failed abruptly in essentially a brittle failure mode with extensive microcracking. Failure was usually preceded by multiple cracking in the axial direction as shown in Figure 8.17.

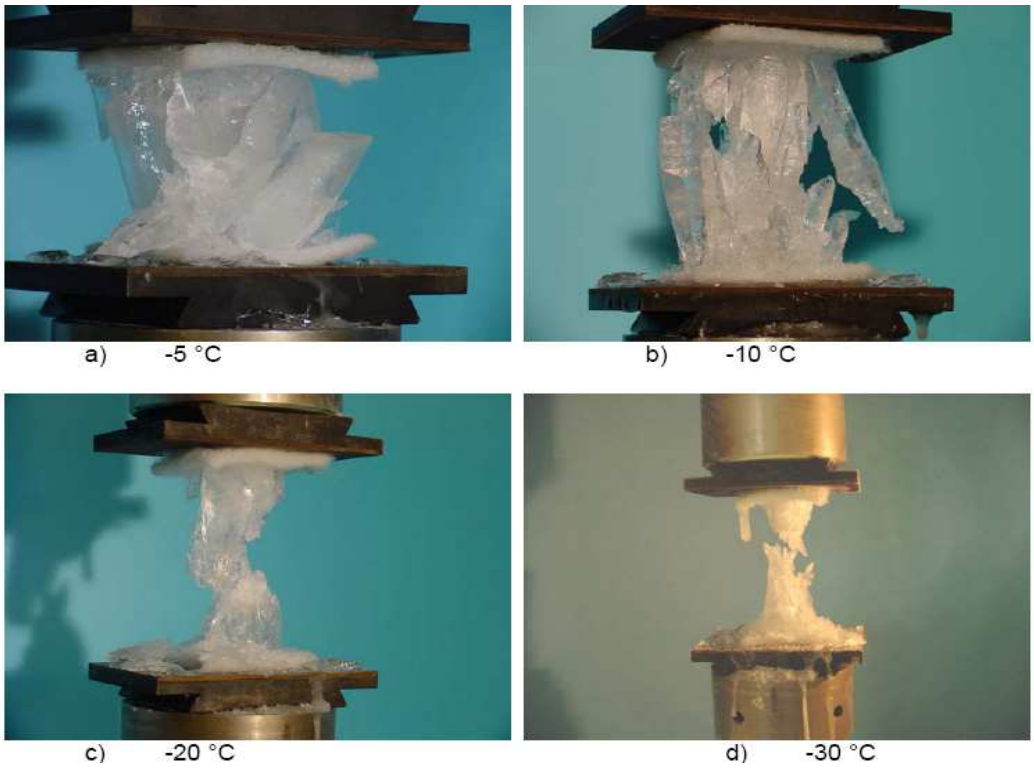

Figure 8.17 Fracture of ice cylinder specimens at different temperatures

The fracture surfaces observed were dependent upon temperature. At the higher temperature of -5^{0}C and -10^{0}C the ice crystals were larger, whilst at the lower temperatures of -20^{0}C and -30^{0}C the crack pattern was much finer leading to smaller ice fragments. The failure modes at all temperatures were brittle.

The measured compression stress-strain curves at various temperatures are given in Figure 8.18 to 8.21. Despite the scatter evident at the lower temperatures of -20^{0}C and -30^{0}C, the ice response was more brittle, as seen by the sharp cut-off at fracture, where the maximum stress is reached. At -5^{0}C and -10^{0}C the stress falls more gradually after fracture, indicating that the ice sustains a reduced load as it is crushed. In all cases, the ice response was approximately linear elastic up to the maximum stress i.e. up to failure. The fracture stress and failure strain were seen to be significantly dependent on temperature. The fracture stress rises from values of about 5MPa at -5^{0}C to about 12MPa at -30^{0}C i.e. increasing with decreasing temperature.

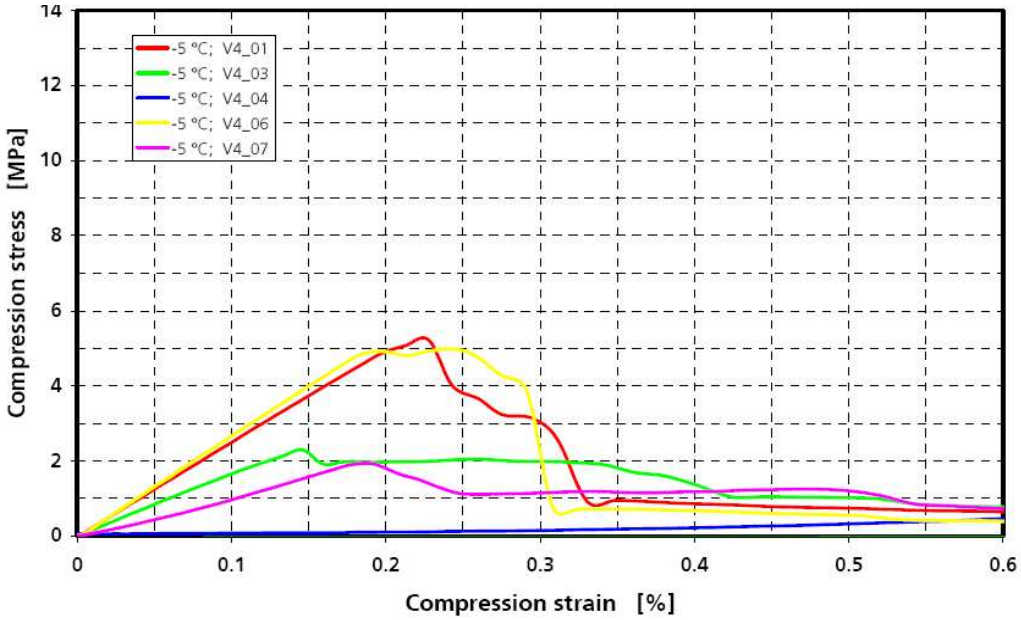

Figure 8.18 Compression stress-strain response at -5°C (Different coloured lines represent repeat tests) (Johnson 2006)

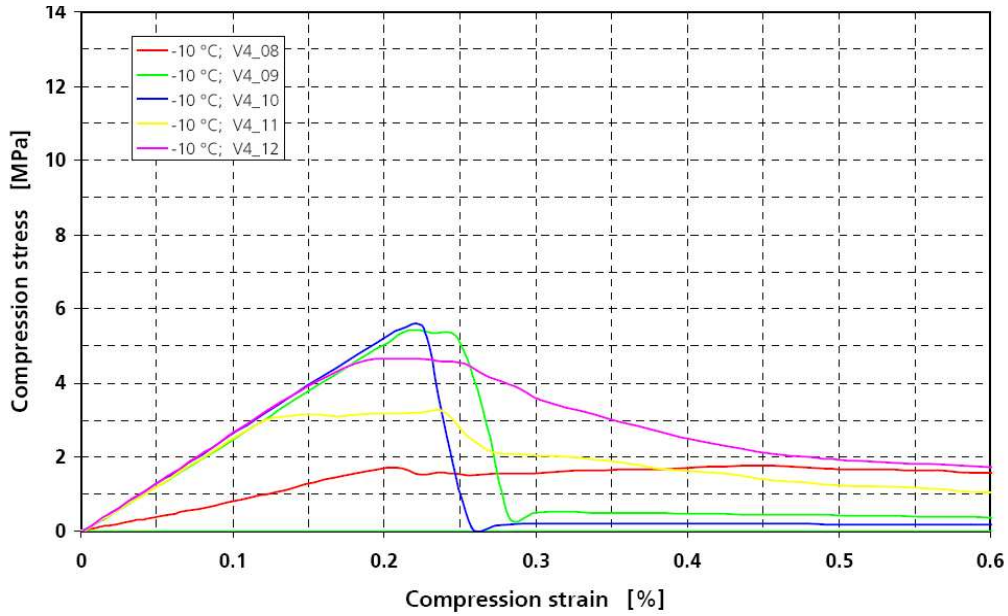

Figure 8.19 Compression stress-strain response at -10°C (Different coloured lines represent repeat tests) (Johnson 2006)

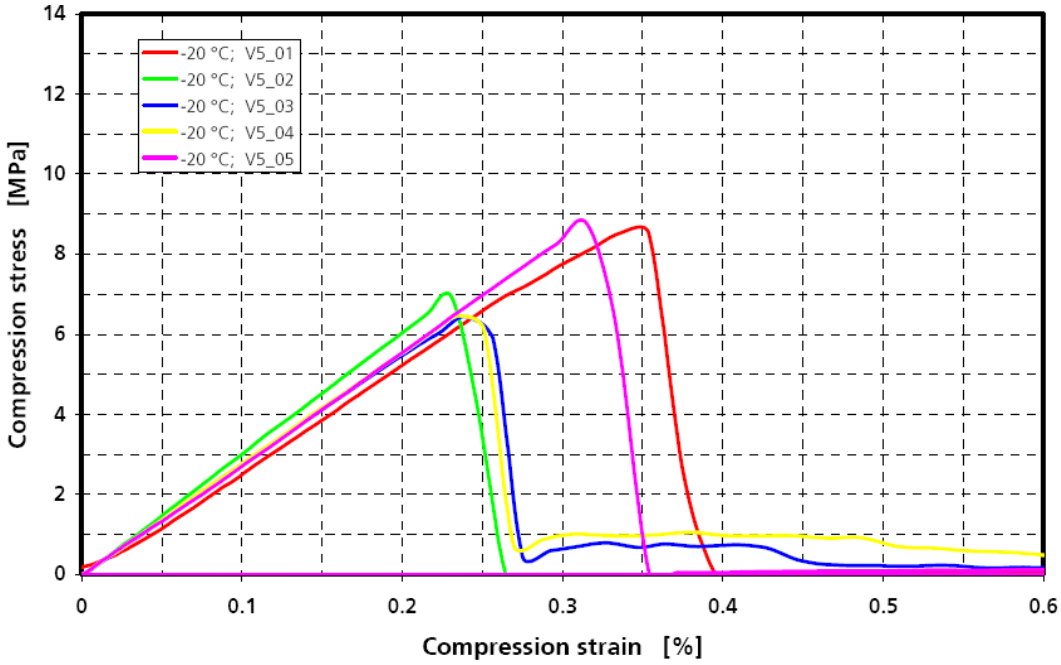

Figure 8.20 Compression stress-strain response at -20°C (Different coloured lines represent repeat tests) (Johnson 2006)

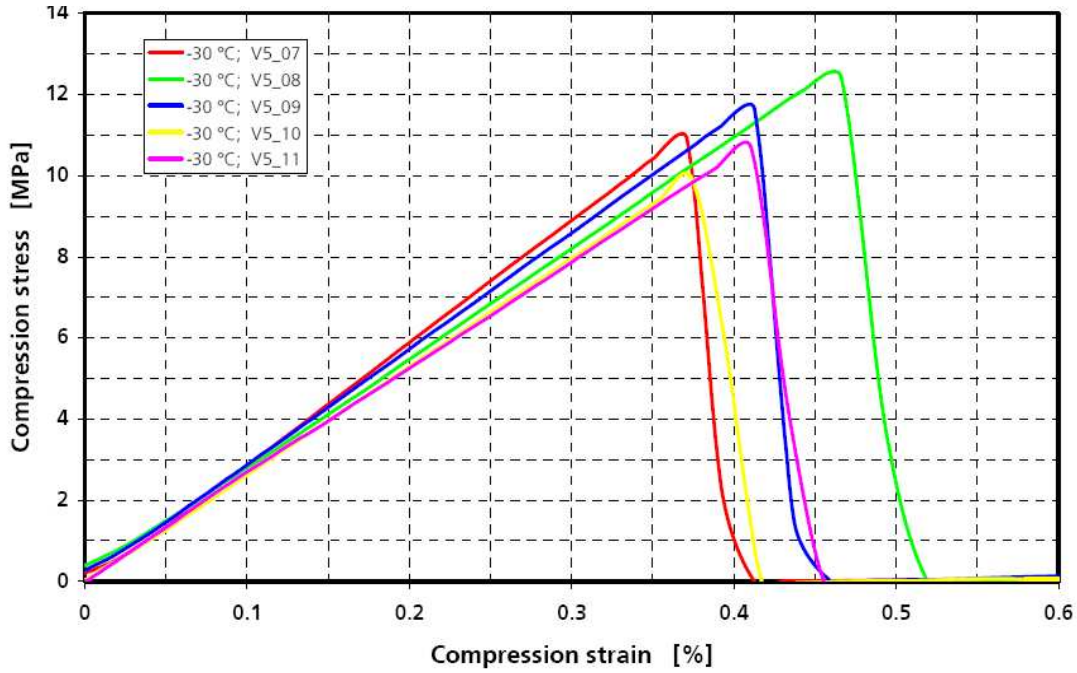

Figure 8.21 Compression stress-strain response at -30°C (Different coloured lines represent repeat tests) (Johnson 2006)

Compilation data for compression modulus and maximum failure stress taken from these detailed stress-strain curves is provided in Figure 8.22. The test curves are close to linear up to the maximum stress, sometimes with a lower initial slope due to load introduction in the test fixture. Thus to avoid any initial effects, the moduli were calculated from the average slope over the stress range 10 – 50 % of the maximum

stress. Mean values and standard deviations of these properties at each test temperature are summarised in Table 13.

Temperature		- 5 °C	- 10 °C	- 15 °C	- 20 °C	- 25 °C	- 30 °C
No. of specimens		4	5	2	5	2	5
E-modulus [GPa]	Mean value	1,982	2,224	2,764	2,816	2,907	2,757
	Standard deviation	0,629	0,572	0,161	0,100	0,071	0,127
	Coeff. of variation [%]	31,757	25,699	5,839	3,547	2,441	4,618
σ_{max} [MPa]	Mean value	3,605	4,113	8,016	7,428	9,941	11,104
	Standard deviation	1,498	1,291	0,377	0,975	0,336	0,727
	Coeff. of variation [%]	41,558	31,398	4,699	13,119	3,375	6,549
ε at σ_{max}	Mean value	0,202	0,267	0,309	0,274	0,354	0,434
	Standard deviation	0,033	0,071	0,008	0,047	0,004	0,048
	Coeff. of variation [%]	16,284	26,680	2,688	17,131	1,176	11,130

Table 13 Summary of E-modulus and maximum stress for ice as a function of temperature (Johnson 2006)

Marked on Figure 8.22 are the best fit least square linear curves to the test data. These show very clearly the scatter in the ice test data, but also the clear trend of increase in E-modulus, and maximum stress as the test temperature decreases from –5 ℃ to –30 ℃. Th e change in compression modulus is relatively small, but that in failure stress is significant with the mean value of stress rising from 3.61 MPa to 11.10 MPa over this temperature range, with the failure strain doubling from 0.20 to 0.43 %.

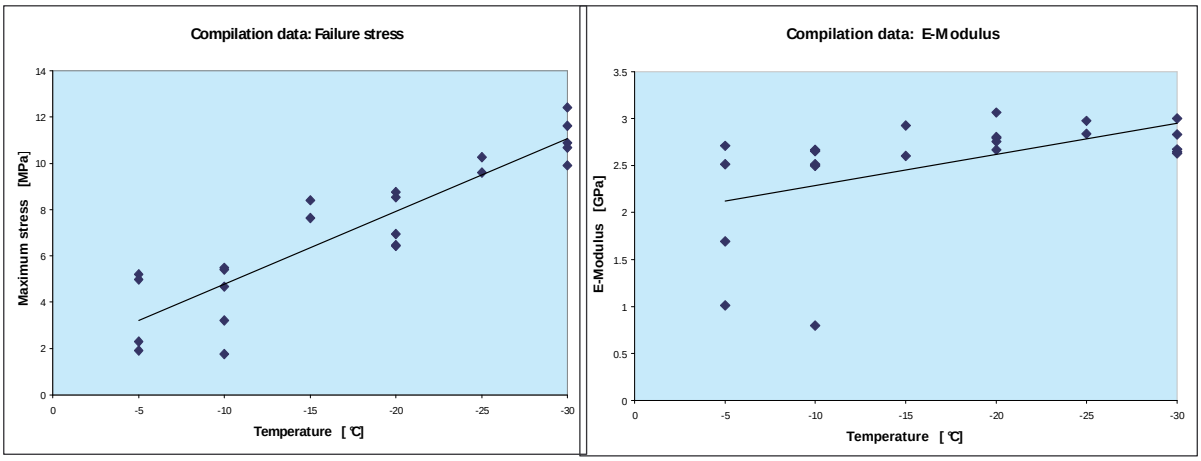

Figure 8.22 Compilation data for ice compression properties, a) Failure stress b)E-modulus (Johnson 2006)

The main conclusion from the tests is that the ice behaviour is linearly elastic with a brittle failure at the loading rates tested. The observed scatter in failure properties is typical for brittle solids, where failure is initiated at flaws in the material, which in this case, could be due to impurity particles, air bubbles and microcracks arising during ice fabrication. This should be accounted for in any test programme by ensuring an adequate number of repeat test are performed.

8.4.6 Ice impacts onto load cells

Additional ice impact tests were performed using a gas gun, involving both spherical and cylindrical ice specimens (Johnson 2006). The objective of these tests was to observe the ice failure modes under high velocity impact and to obtain contact force data during impact, which is very useful for calibrating hailstone numerical models. To obtain quantitative data on dynamic contact loads during impact a new test fixture was developed in which a load cell, mounted on a rigid foundation (concrete block), was the target for the impact tests (Figure 8.23).

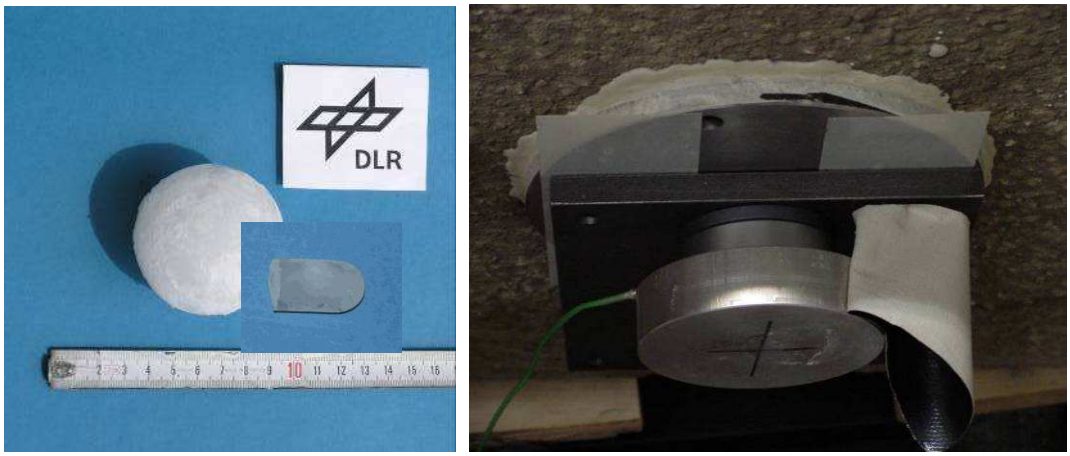

Figure 8.23 a) Ice projectiles b) Target disc with load cell

Impact velocities used were in the range of 46m/s to 158m/s, with ice projectiles of cylindrical shape with rounded ends and masses varying from 9g to 45g. In tests performed at room temperature the ice flowed whereas, with ice taken directly from the freezer at -20^{o}C, plastic type of deformation was visible and ice crystals could be seen flying off. Typical compression strengths were found to be in the range of 2MPa to10MPa. Figure 8.24 shows a typical ice cylinder during impact.

Figure 8.24 Ice impact on load cell at 150m/s

Figures 8.25 and 8.26 give a summary of typical ice impact pulses (force-time data) for a range of projectile masses and velocities. It is seen that measured dynamic peak contact pressures in the high velocity impact tests are estimated to be in the range of 7MPa to 25MPa. At higher impact velocities there is an initial 'Hugoniot peak load' similar to those seen in bird strike tests. The elastic-plastic contribution to the constitutive law may be effective in modelling the ice steady crush response, but the Equation of State (EoS) contribution to the shock front can no longer be neglected when developing ice impactor models. Also evident is a broadening of the pulse for the larger projectile masses.

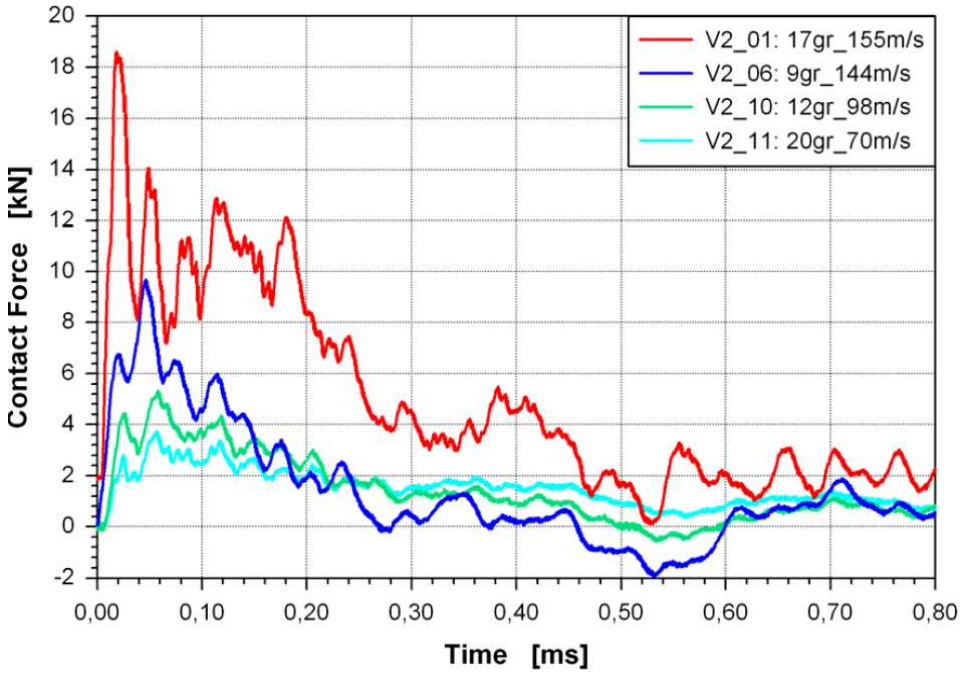

Figure 8.25 Contact force pulses from 24mm diameter ice projectiles

(Johnson 2006)

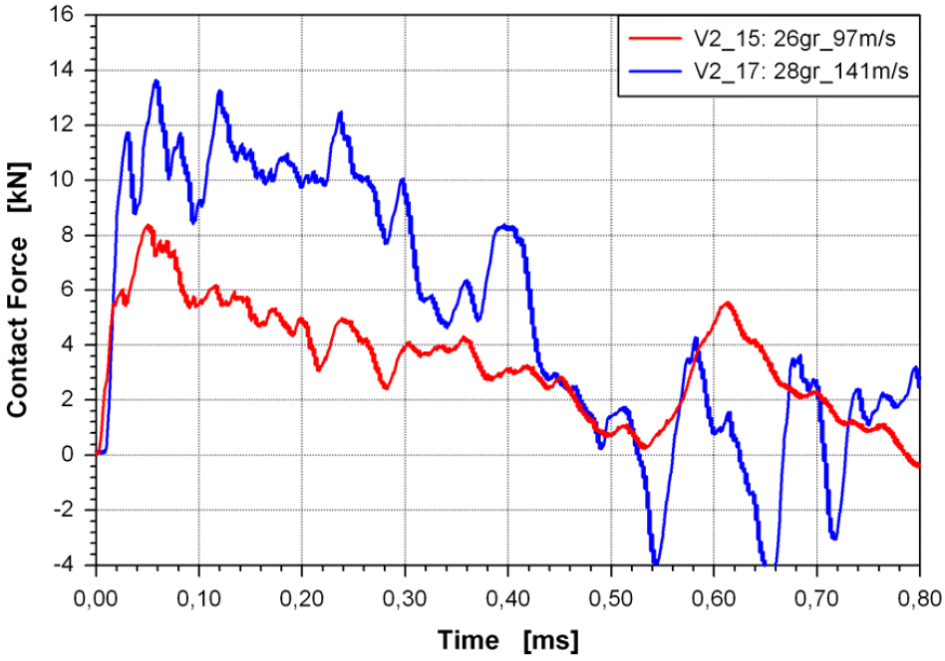

Figure 8.26 Contact force pulses from 30mm diameter ice projectiles

(Johnson 2006)

8.4.7 Ice impacts onto carbon composite plates

A series of ice impact tests were performed on a number of carbon epoxy quasi-isotropic composite NCF (Non-Crimp Fabric) plates. The plates were manufactured by vacuum infusion and the resulting fibre volume fraction was approximately 50%. The panels were cured according to the supplier's recommendations.

Impact tests onto 4mm and 6mm plates

The laminates consisted of biaxial NCF fabrics of direction 0°/90° and ±45° stacked into a quasi-isotropic lay-up. The laminate lay-ups were $[0 / 90 / 45 / -45]_{2S}$ and $[0 / 90 / 45 / -45]_{3S}$ for the 4mm and 6mm thickness plates respectively. The specimens were machined from the panels to a final dimension of approximately $150 \times 100\text{mm}^2$. Eight plates of each configuration were impact tested.

For each test the cut plates were mounted in a window fixture according to the EN standard prEN6038 and the bolts were finger tightened. The inner dimensions of the window frame used in the impact tests were $125 \times 75\text{mm}^2$. The impact velocity was controlled by altering the compressor pressure.

The plates with a thickness of 4mm were impacted using ϕ25mm ice at velocities ranging from 115m/s to 192m/s. The plates with a thickness of 6mm were impacted using ϕ25mm ice at velocities between 103m/s and 114m/s, and using ϕ50mm ice at velocities of 103m/s to 165m/s.

The ice was kept in an insulated box and continuously cooled using a container partially filled with fluid nitrogen. The temperature in the box was in the range of -10 ºC to -40ºC. The 50mm diameter ice impactors were generated by drilling a hole into a circular shell, adding water and freezing slowly, whereas for the 25mm ice impactors, balloons were used. Unfortunately the quality of the ice formed from the balloons was not as good. Of the methods employed it was found that slow freezing was the most effective at inhibiting the formation of voids, which may otherwise produce cracking due to the presence of internal shear forces.

The mid-point deflection of the clamped composite plate was measured using a laser displacement transducer (MEL M7L/20mm) located behind the plate. The behaviour of the impacting ice body was monitored using a high-speed video camera (IMCO Ultranac FS 501 Astromed system frame grab and IMCO Ultranac ICS 20 CCD) with a maximum capacity of 20 million frames per second. The video camera was set-up for a 100 μs delay between the frames and a 5 μs exposure time.

After impact the plates were dismounted, visually inspected, and any observed damage was recorded. Following the impact testing, all the plates were analysed by ultrasonic C-scan, and some plates were cross-sectioned, polished and assessed fractographically to generate detailed damage maps to aid in the understanding of the impact damage evolution.

The impact behaviour exhibited by the ice was significantly different to a solid body impact of the same dimension and weight. It is clear from these experiments that a supposedly 'equivalent' or 'representative' metallic sphere, (for example, one made from aluminium), does not behave in the same manner as an ice sphere on impact. There are a number of reasons for this which can be related to a difference in the energy transfer between the impacting bodies:

- Firstly, part of the initial kinetic energy of the ice sphere is transferred into creating new surfaces, by crack initiation and crack propagation, a phenomena not generally present in solid body impacts. At this initial stage the ice begins to crush and fail locally by micro-cracking.
- Secondly, as the impact progresses, the ice now behaves as a material which is much more compliant than the original solid ice.
- Thirdly, the yielded ice, now basically in fragments, hits the plate and flows in a very similar way to a fluid.

This transitional behaviour is clearly evident in Figure 8.27 which shows high-speed camera pictures from an ice impact. The figure depicts the basic ice impact behaviour, the local crushing and the subsequent fluid-like flow of the ice. Only a small portion of the sphere's volume had disintegrated by the time the peak force was reached. The 'whitening' that is clearly evident in high speed film/photography is evidence of micro-crack generation away from the crush front.

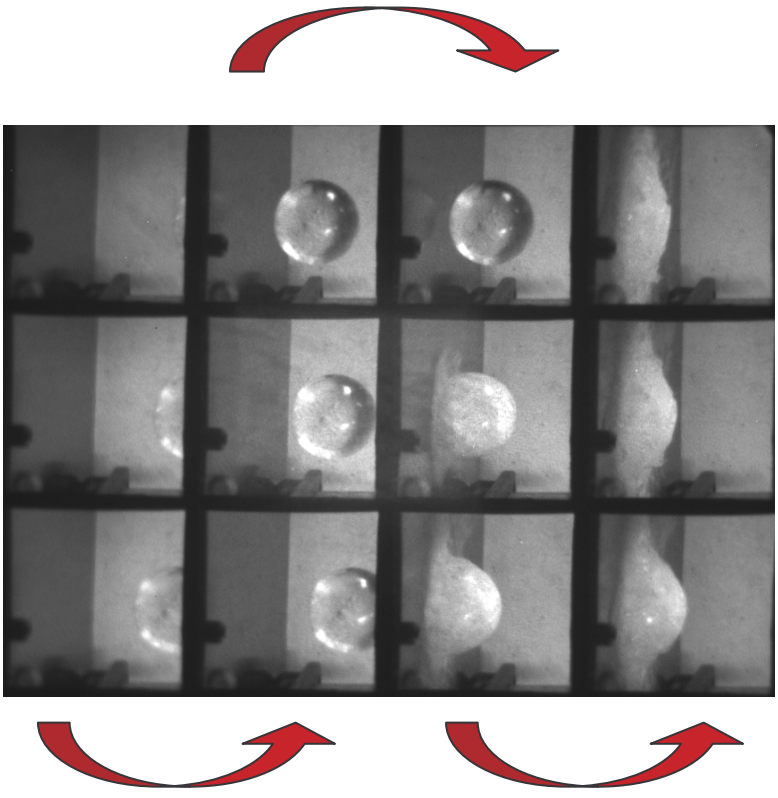

Figure 8.27Ice (diameter 25mm) impacts (Johnson 2009). The red arrows show the sequence of images taken (i.e. top left to bottom right). Within each of those images the ice sphere is travelling from right to left and changes from clear ice to white ice as it hits the wall, starts to crack and spreads out over the impacted surface.

The typical response of a 6mm thick plate to small and large diameter ice impacts is plotted in Figure 8.28. The out-of-plane (i.e. movement perpendicular to the laminate) displacement is measured in the centre of the plate.

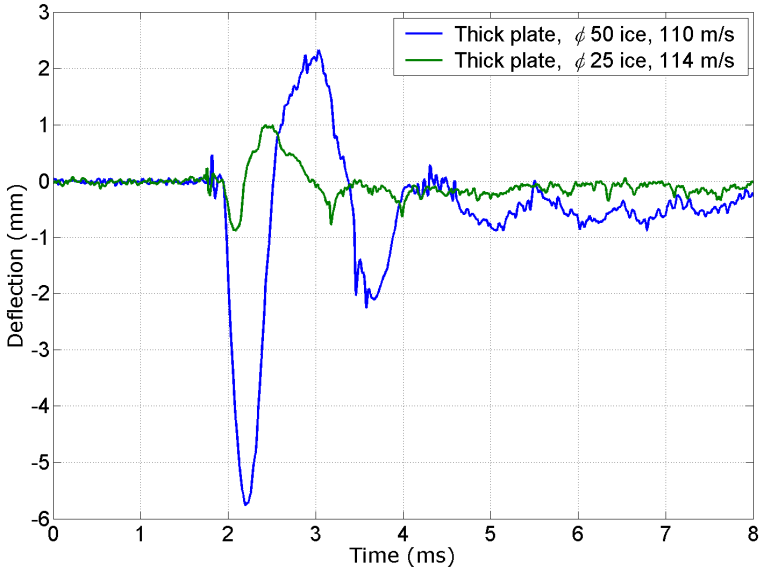

Figure 8.28 Response from ϕ25mm (114m/s) and ϕ50mm (110m/s) ice impact onto a 6mm plate (Johnson 2009)

The ϕ25mm ice impacts did not cause any visible damage to the thick plates and the ultrasonic C-scans confirm this.

For the ϕ50mm ice impacts the situation was different. Impacts occurring at speeds below 110m/s did not cause any visible damage to the plate surfaces or edges. However, at increased speeds (from 110m/s to 136m/s) visible damage on the surface was detected (Figure 8.29).

Figure 8.29 Surface damage after impact at increased speeds (from 110m/s to 136m/s)

The damage was not located at the impact site, but it was found in the clamping regions (at the window frame position) in the form of matrix splits and fibre fractures. The ultrasonic C-scan pictures are depicted in Figure 8.30 and the polished cross section shown in Figure 8.31. The matrix cracks visible in Figure 8.31 are solely contained in the ±45º and 90º layers which are closest to the impacted surface. The damage consisted of matrix cracks directly below the impact point extending a couple of layers downwards. No damage was found in or below the uppermost 0º layer (fourth layer from the impacted side). Thus, it is believed that the damage was initiated by high contact forces created at the very beginning of the impact event.

For the higher impact velocities matrix cracks developed deeper within the material. By increasing the impact velocity to 107m/s these matrix cracks evolved into delaminations.

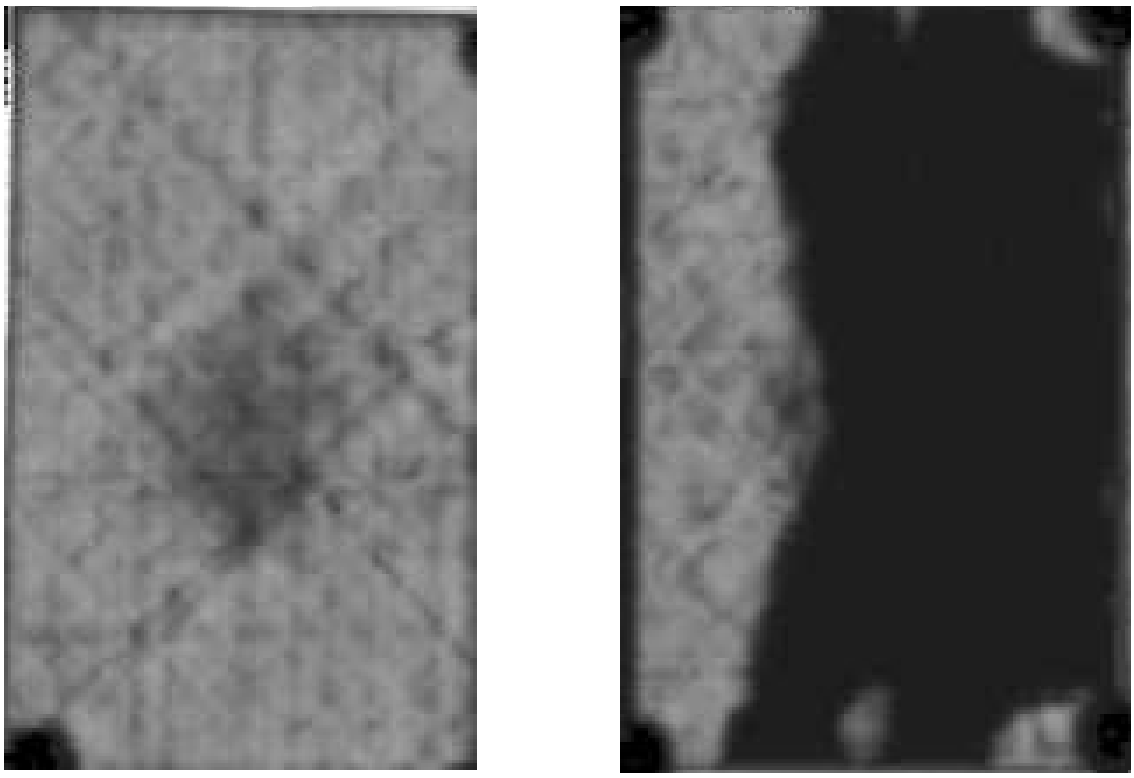

a) b)

Figure 8.30 Ultrasonic C-scan of two 6mm thick plates impacted by ϕ50mm ice at a) 103m/s and b) 107m/s

For ϕ25mm ice impact on the 4mm thick laminates at high velocities (i.e. higher than 190m/s) conspicuous surface damage (surface splits and edge delaminations) occurred at the clamped regions. The ultrasonic C-scan showed massive delaminations. For lower impact speeds, no delaminations due to the ice impacts could be detected. Under no ice impact condition was fibre failure at the impact site identified.

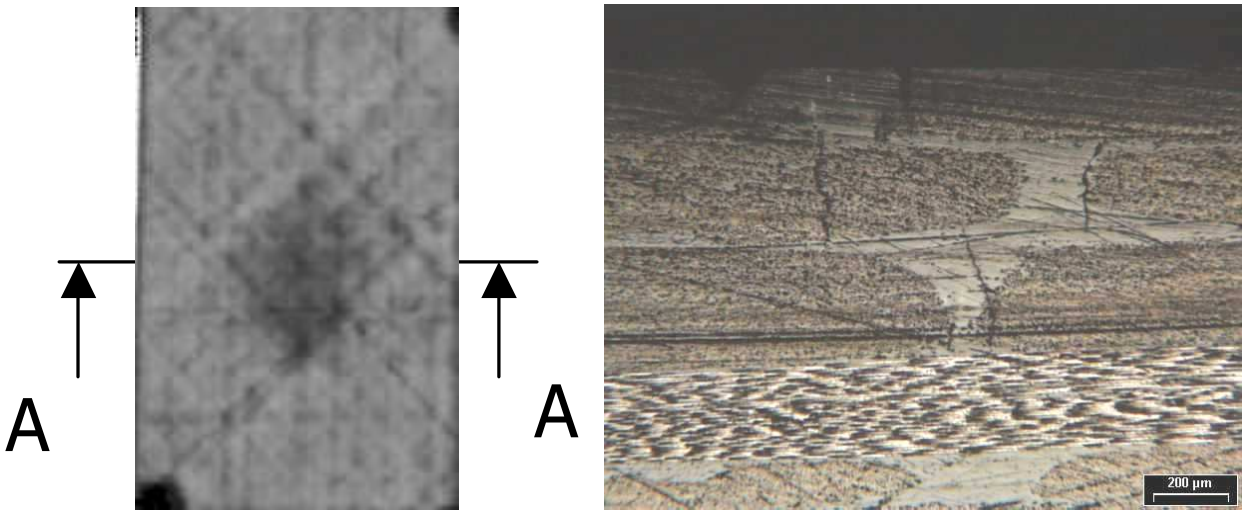

A-A

Figure 8.31 Damage in cross-section A-A (weft-direction) of a 6mm plate impacted at 103m/s; Matrix cracks in the ±45° and 90° layers closest to the impact surface

The results indicated that the delamination threshold for impact using 50mm diameter ice spheres, onto 6mm composite plates, is in the region of 103m/s to 107m/s. The former velocity resulted in matrix cracks while the latter created massive delaminations.

Impact tests onto 1.8mm and 5.4mm plates

Subsequently a second set of tests were performed. Two material configurations using different thickness, namely 1.8mm and 5.4mm, were investigated. The laminates were again made from biaxial carbon fibre NCF and epoxy. The laminates consisted of biaxial NCF fabrics of direction 0°/90° and ±45° stacked into a quasi-isotropic lay-up. The laminate lay-ups were $[0 / 90 / 45 / -45]_S$ and $[0 / 90 / 45 / -45]_{S3}$ for the 1.8 and 5.4mm thickness plates respectively. Specimens were saw cut from panels to a final dimension of approximately $250 \times 250\text{mm}^2$. Two plates of each configuration were impact tested. The diameter of the ice ball was 48mm with an average density of 970 kg/m^3.

The measured quantities were ice velocity, centre deflection of the plate, and back plate centre and off-centre strain. The strains were measured in the fibre direction and the off-centre gauge was placed 50mm off the centre. The test setup is illustrated in Figures 8.32 and 8.33. The dimensions of the rig window measured 200 x 200mm.

Figure 8.32 Test rig with pipe end in test no. 2

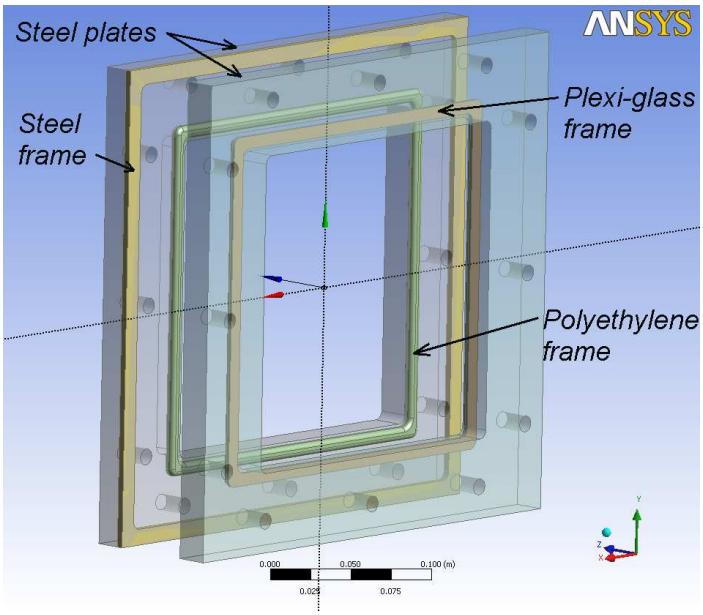

Figure 8.33 Drawing of clamping device in test no. 2

The ice impact sequences as captured by photography for the ϕ50mm ice impacts are shown in Figure 8.34.

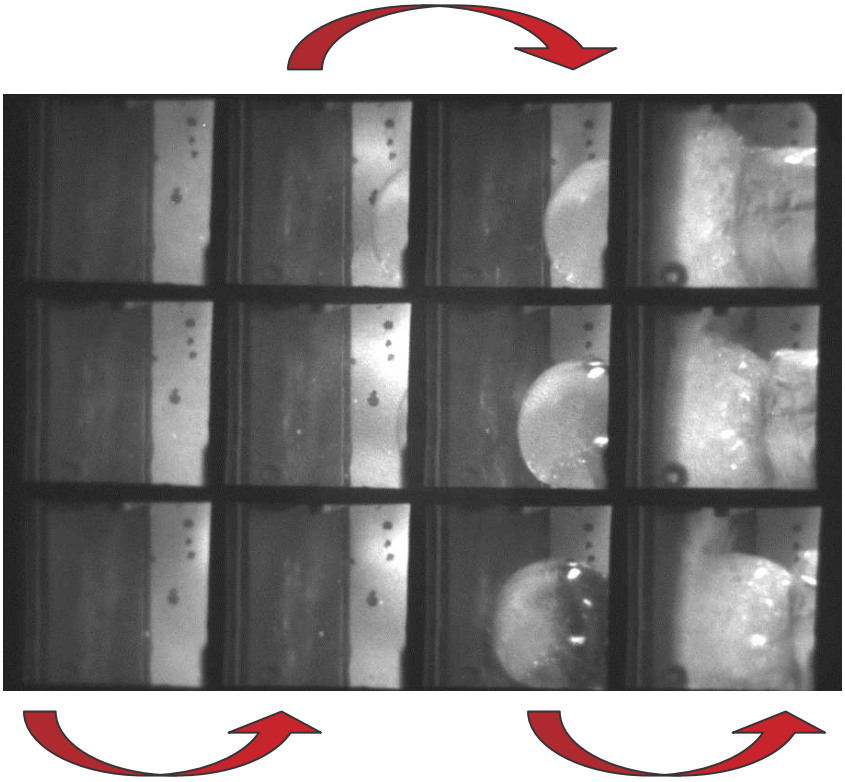

Figure 8.34 Ice impact test sequence for 50mm ice ball

(Johnson 2009)

As seen during previous tests, there was a rapid progression of delamination covering the whole panel area as soon as damage was initiated. From the limited number of tests performed, it was difficult to determine the velocity threshold for damage initiation, and the damage progression after damage initiation.

More test results are given in Figures 8.35 and 8.36.

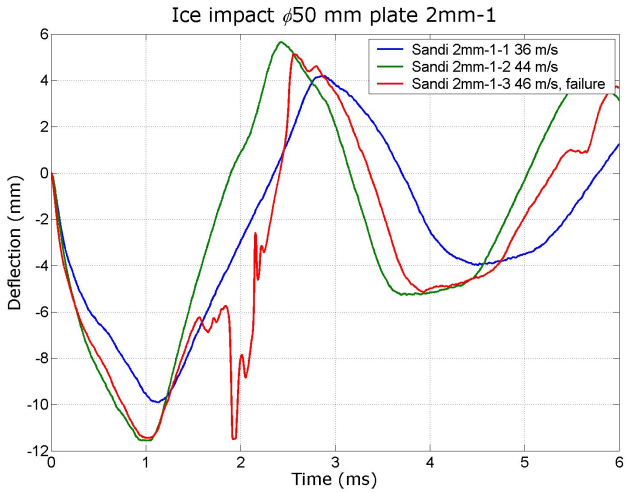

a) Deflection

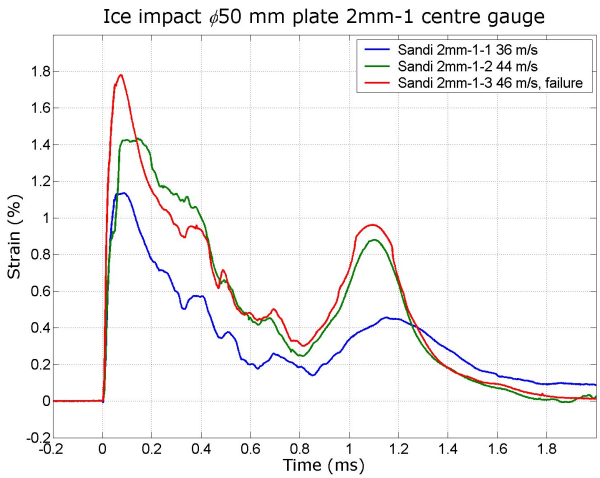

b) Strain for centre strain gauge

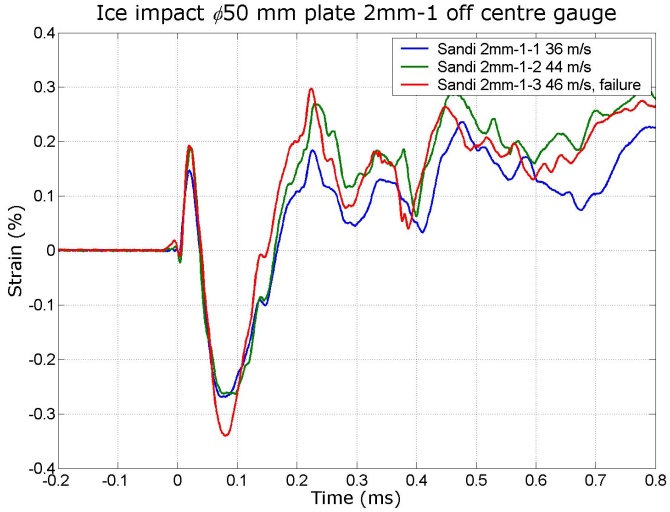

c) Strain for off centre strain gauge

Figure 8.35 Results from ice impact onto plate with 1.8mm thickness

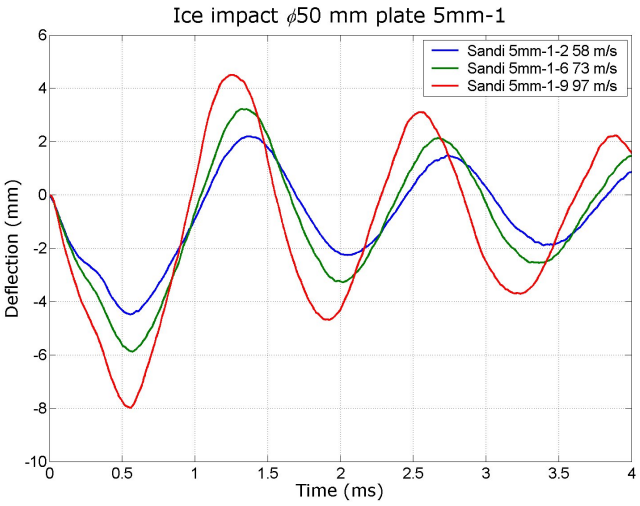

a) Deflection

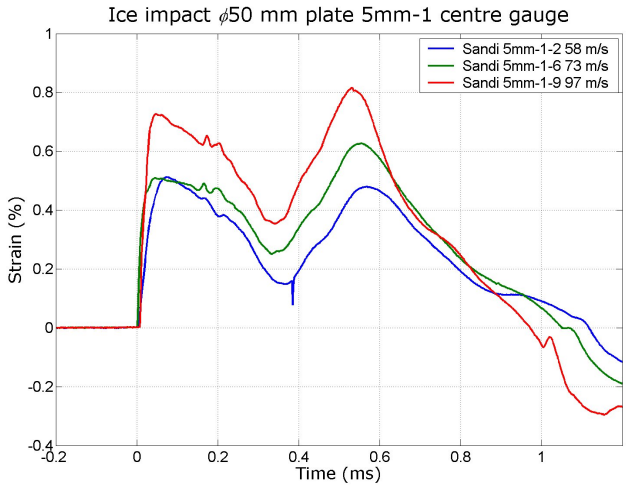

b) Strain for centre strain gauge

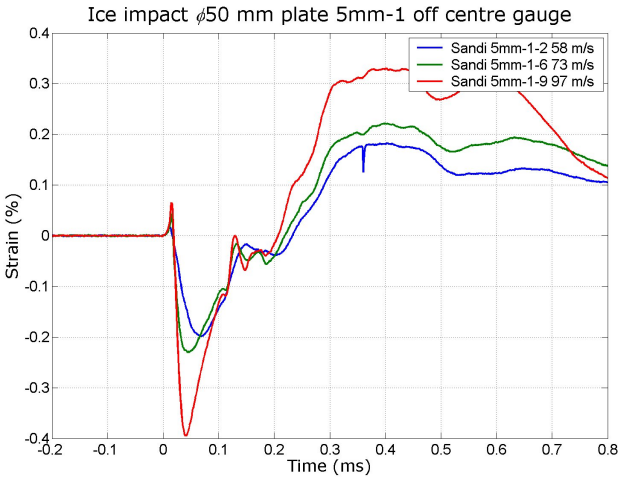

c) Strain for off centre strain gauge

Figure 8.36 Results from ice impact onto plate with 5.4mm thickness

These tests have shown that either: it is the duration of the stagnation pressure which drives Mode II failure, and hence the results showed either no delamination or a very large delamination with minimal increase in impact velocity, (it was extremely difficult to obtain a small delamination); or, alternatively, the delamination is partly caused by the through-thickness 'shock' wave which is reflected in tension at the back face of the panel, thus creating the delamination under Mode I conditions. This tends to be the dominant mechanism when the panel is comparatively thick and when no bending occurs during impact.

8.4.8 Ice impacts onto glass composite sandwich panels

Ice impacts at velocities ranging from 48m/s up to 265m/s were performed to evaluate the impact of ice on to the fuselage of a composite seaplane. Cylinders of ice (of length 110mm, diameter 12.5mm, and mass

13.5g) were fired at 10mm thick sandwich panels composed of woven glass fabric with an epoxy resin system (GFRP), either side of a foam core.

At the lower velocities, for example at 48m/s, the ice rebounded after the impact. In these tests the ice tended to flow over the surface and damage in the panel was barely discernible with the naked eye; it was limited to a slight discoloration in the contact area. At low magnification a fine network of matrix cracks was visible in the contact area, roughly 0.2mm apart and running in the $+45^0$ and 45^0 directions. Cracks in the 0^0 and 90^0 directions were minimal.

As the impact velocity increased, delaminations formed and then fibre failure followed, as the ice did not have time to flow and it behaved more like a hard impact. At 265m/s the plate was perforated and a flat disk formed at the front face, about 25cm by 1.5cm in size which had been punched out from the skin along three quarters of its circumference with the other quarter acting as a hinge (Figure 8.37). It was bent inwards and behind it most of the foam had vanished. The damaged area was much larger than the impacting ice cylinder cross-sectional area.

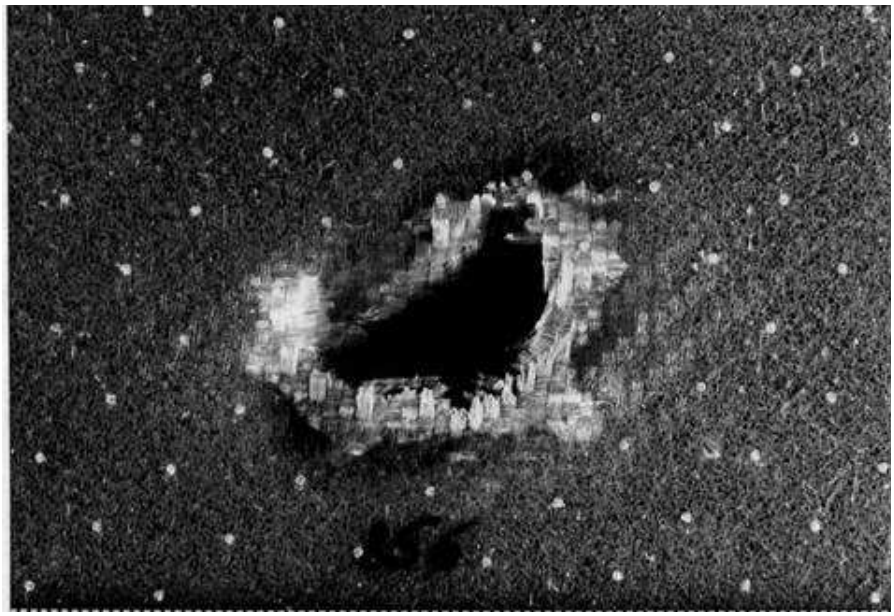

Figure 8.37 Impact at 265m/s: front face

On the back face, a flat disk, about 25mm by 23mm had been pushed out, again with a quarter of the circumference remaining attached. The most severe damage was not at the impact centre but a short distance away, where the disks had been punched out. This is termed shear plug failure (Figure 8.38). The ice specimen had flown through the hole. Matrix cracking was evident at the front and at the back was a large delamination (155mm by 165mm in size).

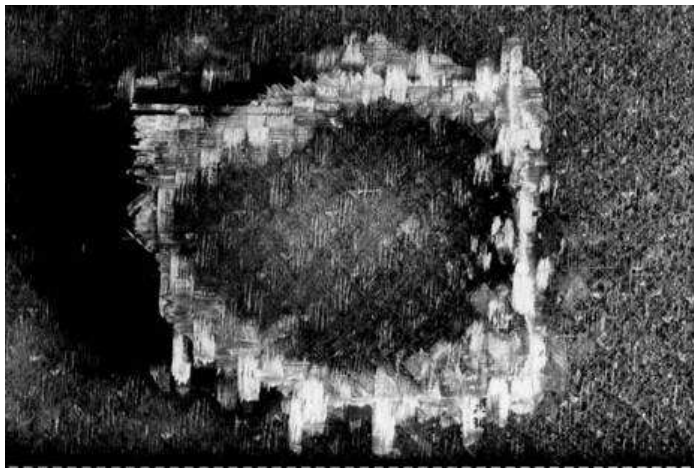

Figure 8.38 Impact at 265m/s: back face

Since the composite was fairly elastic the hole closed up after the ice had passed through. The sandwich panel was locally very stiff in bending and thus could not absorb energy by elastic deformation. Hence the ice penetrated the composite instead of energy being absorbed through shell bending.

8.5 Review of existing standards.

8.5.1 Introduction

This section provides a review of the readily available standards currently in general use in both the civil and military worlds. The review will identify specific requirements for hail resistance and the hail environment.

Although it was evident from research that the Civil Original Equipment Manufacturers (OEMs) are taking into consideration the hail threat (For example Reference 1, see Reference section, an Airbus presentation describing some of the hail threat), this information could not be obtained for this analysis and has not been considered in this report.

This review therefore concentrates on the more readily available standards. Table 14 identifies the documents reviewed as part of this exercise.

Standard	No.	Standard overview	Applicable details
DEF STAN	00-970	This document provides requirements and guidance for the design of aircraft to meet the airworthiness requirements for UK military operation. The DEF STAN is broken down into sections for different types of aircraft.	There are several references to hail, although they are limited to ingestion of hail into engines.
DEF STAN	00-35	This standard provides requirements for the environmental conditions experienced by defence material in service.	Part 3 defines the hail threat environment and includes a global threat model that identifies the greatest hail threat. It also covers the areas of the aircraft that are at most risk. Part 4 defines the basic elements of a test in regards to a one off large hailstone impact and an 'erosion' test from repeated impacts of smaller stones.
MIL Standard	MIL-HDBK-17-3F - Damage Resistance, Durability and Damage Tolerance.	MIL-HDBK-17 provides methodologies and lessons learned for the design, analysis, manufacture, and field support of fibre-reinforced, polymeric-matrix composite structures. It also provides guidance on material and process specifications and procedures for utilization of the material data.	Hail is clearly defined as a threat to structural integrity, although specific parameters are not covered.
MIL Standard	MIL-HDBK-310 – Global Climatic data for developing military products.	This handbook provides climatic data primarily for use in engineering analyses to develop and test military equipment and material.	This section identifies the specific hail environment.
ASTM	ASTM F320-05	The document defines a test methodology for the impact resistance of aircraft windshields during hailstorm conditions using simulated hailstorms.	Although this is designed to be used for a specific area of the airframe (windshields) a lot of the methodology will also be applicable to other risk areas of the aircraft structure; e.g. leading edges.
CS-23	Certification Specifications For Normal, Utility, Aerobatic, and Commuter Category Aeroplanes.	EASA Certification Specifications for Normal, Utility, Aerobatic, and Commuter Category Aeroplanes – 14th November 2003	There are no specific references of a hail threat. However, the standard does cover some of the key requirements related to damage tolerance due to impact damage which is applicable to the hail threat.
CS-25	Certification Specifications For Large Aeroplanes	Certification Specifications for Large Aeroplanes CS-25 - Amendment 2 - 2 October 2006	There are no specific references of a hail threat. However, the standard does cover some of the key requirements related to damage tolerance due to impact damage which is applicable to the hail threat.
FAR-25	Title 14: Aeronautics and Space Part 25 airworthiness standards: transport category airplanes.	Part 25 - airworthiness standards: transport category airplanes Version from the e-CFR (Electronic Code of Federal Regulations) website (www.gpoaccess.gov/ecfr/) was reviewed. Version current as of the 14th October 2010	There are no specific references describing the threat from hail. The only reference to hail is in section 25.773 which relates to maintaining clear visibility in severe hail conditions.

Table 14 Reviewed standards

8.5.2 Hail Threat

The key requirement from a structural safety perspective is to prevent damage during flight and ensure that when an aircraft encounters a hailstorm, it is able to survive it and land. In the flight phase, the threat is related to the speed of the aircraft as well as the size of the hailstones. It is the flight phase threat that is of primary interest in most of the available standards.

There is also a risk to the aircraft whilst stationary on the ground, as identified in MIL HDBK 17-3F, Reference 2 (Para 7.5.2.3). This standard identifies the risk to such aircraft and highlights the requirement to design composite aircraft structure to be resistant to typical hail strike energies to minimize the amount of repair required following a hailstorm.

8.5.3 Hail Environment

Most standards focus on aspects such as the hail size and hail density to provide a level of kinetic energy threat. However, both DEF STAN 00-35 (References 3) and the MIL-HDBK 310 (Reference 4) go further and identify the global locations where aircraft are at most risk of experiencing hail. They also look at typical sizes of hailstones, storm duration and storm size with the likelihood of encountering them. Other aspects that are covered are the density and terminal velocity of the stone. The DEF STAN (Reference 5) even goes as far as to identify the range and maximum hailstone size in a given area (1m).

Hailstone Extremes for Design, Reference 6, was prepared prior to the revision of MIL-STD-210A (the predecessor MIL-HDBK-310) to define the risks / probabilities of occurrence of hailstones. The author goes through a logical process of defining the key parameters (for example maximum hailstone size and frequency hail storm days) used to derive this probability data. Where possible, the author has used published works to support and justify the figures chosen at each stage. The figures concluded in this report have been read across to the MIL-HDBK 310.

The second reference included in the MIL-HDBK, Reference 7, is an article published in Weatherwise magazine. The article talks about a new record sized hailstone which fell in Kansas in September 1970. There is some more limited information defining other properties such as dimensions and weight.

8.5.4 Specific Threats due to hail.

Impact Damage Resistance and Damage Tolerance

The greatest threat to aircraft structures from hail, is impact damage. This area is of particular concern where aircraft structures are increasingly being produced from composite materials and there is a possibility that damage could be incurred that is barely visible to the naked eye. Although most standards (Including MIL, CS 23 (Reference 8) and JAR 25 (Reference 9)) are starting to take into account impact damage resistance and damage tolerance (A impact damage resistance section for DEF STAN[1] 00-970 has been ratified and

[1] DEF-STAN contact:Nige' Braunton
Editor Def Stan 00-970
Elm 1B #4126, DES SE Air-MAEI-1-ADS2, ABBEYWOOD, BRISTOL, BS34 8JH
* External (44) 03067935366
desseair-maei-1-ads2@mod.uk

will be included in the next issue of the document), only DEF STAN 00-35 (References 10, 11) provides a specific impact test to determine the possible affect on structural integrity.

Multiple / Repeat strikes

Impact damage is typically inflicted by a single strike e.g. caused by a dropped tool. The threat from hail, however, is different, as it exposes the aircraft to multiple (typically smaller) impacts over a prolonged period of time.

There are a number of examples of multiple impact to in-service aircraft and one such example is depicted in Figure 8.39 which shows damage to a Boeing 737 EasyJet aircraft.

Figure 8.39 Hail damage to Boeing 737 aircraft

Hail damage was sustained to the Douglas DC-9-81 (MD81) of the Scandinavian Airlines System (SAS) whilst flying at 140 m/s in the middle of a heavy hailstorm. Hailstones up to 50 mm were reported that generated serious dents in the nacelle leading edge. These dents were up to 50-70 mm in diameter and 5 mm deep. In this case, the most critical scenario to be considered would be a hailstone impacting the most prominent point on the lower section of the intake in a direction parallel to the nacelle axis.

Hail ice impact events can cause significant damage, as exemplified by a hail storm that occurred in the Dallas/Fort Worth area in 1995. This hailstorm dropped hailstones that were up to grapefruit size (about 100mm in diameter). Significant damage occurred to composite and metal parts of over 100 aircraft parked outside.

A further example is reported when BAX aircraft flight 705BX encountered severe weather over Alberta Canada on Friday, 11 Aug 2006 at Time 15:56. The aircraft was cruising at 35,000 feet when it encountered *tennis ball* sized hail. All *landing lights* were destroyed, as was the *radar*, and the crew was forced to make a "**blind**" emergency landing. Upon safe return to the ground, the first officer and flight engineer quit. It was thought that the aircraft was a *total loss,* as its structural integrity had been compromised. Figure 8.40 below shows the damage sustained.

Figure 8.40 Hail damage to BAX aircraft

Although most standards fail to consider this unique threat, DEF STAN 00-35 Part 4 (References 11) defines an ‘erosion’ test whereby very small multiple ice balls are ‘fired’ at the surface for the specific purpose of eroding the material surface (This test is discussed further in later sections of this report).

Investigating the origins of the erosion test described in DEFSTAN 00-35 Part 4 (Reference 11) involved trying to identify the references that underpin DEFSTAN 00-35. However, despite exhaustive research, the primary reference, Liquid and solid particle erosion testing prepared by the Cavendish Laboratories, could not be found. It is likely that much of the detail of this DEF STAN would have been derived from this paper.

During this search, QinetiQ made contact with several key stakeholders involved with the development of DEF STAN 00-35. It was noted during discussions that an exercise to update the sections relating to hail in

the DEF STAN was in progress and that the initial focus would be to better define the hail environment, although the stakeholders had concerns about the availability of data.

The primary concern the authors of the hail sections of DEFSTAN 00-35 held related to erosion testing was the shortage of test houses that had the capability to undertake this type of testing. When the current issue of the standard was published in 1997, the authors reported that there were three recognised facilities that had this capability, but were aware of at least one that no longer existed and were unsure of the rest. Several global test houses that may be able to conduct erosion testing were identified, the Saab rotating arm facility in Sweden (although this was limited to liquid erosion with max drop size of 2mm in diameter), Cavendish Laboratories (University of Cambridge) and Stork Material Technology.

The DEF STAN authors were unaware of any facility that had the capability to conduct testing with larger hail particles at varying speeds.

Whilst looking for the hail reference, QinetiQ also made contact with some of the researchers at the Cavendish Laboratories. It's clear from discussions, and available documentation, that the Cavendish Laboratories have done a significant amount of research in erosion and erosion testing, some of which was related to hail. Although only a small section of the paper covers hail/ice impacts, Reference 12 summarises some of the research work done by the Cavendish Laboratories in this area.

Although this investigation did not fully identify the origins of the data within DEF STAN 00-35 as hoped, discussions with stakeholders have raised some interesting questions about the viability of such testing. The availability of test houses that may have the capability to conduct such testing would be a restriction on what could be achieved. Consensus seemed to suggest that multiple impact hail testing including varying sized hail and speeds would be incredibly difficult (not least generating representative hail) and thus very expensive

8.5.5 Ingestion into the engine

One area where the threat from hail has been defined in the standards is ingestion into the engines. DEF STAN 00-970 in particular (References 11 through 13) and the FAA standard (References 14 and 15) define the risk presented by hail and some of the necessary measures for qualifying engines. Some of the main parameter requirements from these standards are defined in table 15

Standard	Max hail size (inches)	Altitude (ft)	Speed	Number of hail impacts per Square ft of frontal area	Specific Gravity
DEF STAN 00-970, Part 7, Section 7 – Leaflet 700 Propulsion System Installations - Para 3.3	2	From Sea level up to Max cruise altitude or 8000ft whichever is lower.	max	2 hailstones	0.8 to 0.9
DEF STAN 00970, Part 1, Section 5 – Powerplant	2	From Sea Level up to max cruise altitude or 40,000ft whichever is lower	max	2 hailstones	0.8 to 0.9
	Aeroplanes capable of operating at sustained supersonic speed shall be evaluated at typical supersonic cruise speeds up to the cruise altitude of the aeroplane at the applicable design cases listed below				
	2.0	40,000	Typical	1	0.8 to 0.9
	1.0	50,000	supersonic	8	0.8 to 0.9
	0.25	60,000	cruise	40	0.8 to 0.9
DEF STAN 00-970 Part 11, Section 3 – 3.E790 – Ingestion of rain and hail.	Not specified	Not specified	The hail ingestion velocity and engine operating conditions should be such to simulate the most arduous conditions with respect to ingestion within the relevant part of the flight envelope.	Not specified	Not Specified
FAA (Federal Aviation Regulations), Part 33, Section 78 – Rain and Hail ingestion	One 1-inch diameter hailstone for engines with inlet area s of not more than 100 square inches	Up to 15,000	Max True Airspeed	1	0.8 to 0.9
	One 1-inch and one 2-inch diameter hailstones for each 150 square inches of inlet area, or fraction thereof, for engine inlet areas of more than 100 square inches	Up to 15,000	Max True Airspeed	2	0.8 to 0.9
	Supersonic aircraft				
	1 inch Or ¼ inch	35,000ft Or 60,000ft	Supersonic cruise velocity	Not specified in this section	Not specified in this section

Table 15 Parameter requirements for aircraft standards.

8.5.6 Qualification of a hail design

Although there is recognition that aircraft are under threat from hail and guidelines exist for design against impact, there is little detailed information related to the qualification requirements to demonstrate the ability to meet the hail threat.

DEF STAN 00-35 Chapter 3.19 Section 2.3 (Reference 8) provides the basics for two hail tests. The first of these uses clusters of small hailstones to determine the erosion resistance of materials. This is the only time a multi-impact test is defined in the standards reviewed. Ideally, measured data should be used to define the test parameters as much depends on the aircraft speed and global location. However, in the absence of measured data, the standard identifies that a rain intensity of 25mm/hr with a predominant particle size of 5mm and stone density 0.9 g cm^{-3} should be used. The second test is used to determine the structural performance of materials when impacted at high velocity with a single large hailstone. It is noted that a standard test cannot be defined and that the test conditions should be defined on a case by case basis. Where actual data for the max hailstone likely to be encountered is not available, a default size of 19mm diameter (considered to represent a 1% risk of being encountered in flight through 160km flights cells), should be used. The standard also describes the facilities that can undertake the work and the basic test procedures.

Another hail test is defined in ASTM-310 (Reference 16). This document defines an impact test involving a single ice ball. The standard has been designed primarily for the determining the impact resistance of aerospace transparent enclosures. Ice balls of diameter 0.5, 1.0 and 2.0 are used at velocities ranging from 200-2000ft/s (depending on aircraft type).

9 Outcomes

No global hail climatology currently exists. In response to this hail climatologies have been produced from global model and satellite data in line with the objectives of this study. The NWP-model-based hail prediction used to provide global climatological data is empirically based relating ground observations of hail size to radiosonde measurements of upper air temperature and humidity structures over the USA. Old but still relevant data was obtained for 274 occasions of hail during the period from Jan 1st 1950 through to 1953. The radar data that was used here to estimate the probabilities of encountering hail of different sizes has been compared to ground observations of hail between 1998 and 2006. Using the radar based three dimensional climatology, tables of the probability of intercepting hail of different sizes within different temperature ranges have been produced. Sensitivities to these assumptions have also been explored. This study has provided a survey of hail physical characteristics and hail size distribution properties as set out in the objectives. The extreme values provide worst case estimates for hail density, fallspeed and relative frequency as a function of size. The probability tables can be used as an estimate of the worst case probabilities of intercepting hail of different sizes for use in designing aircraft structures. The tables also indicate that multiple hits from smaller hailstones are potentially a problem that aircraft designers need to consider.

A comprehensive review has been produced of the use of composites in aircraft production, the existing test standards that are relevant for hail threat, the mechanical characteristics of ice and the damage caused to test composite structures. This has been carried out for a range of relevant hail sizes and impact velocities.

10 Conclusions

While the density of hail can vary, especially for sizes smaller than ~20 mm, it approaches the density of solid ice for larger particles. Therefore, it seems appropriate to assume a worst case hail density of 917 kg m^{-3} for safety applications.

Because of shape and density variations the terminal fallspeed of hail can vary. The worst case fallspeed relationship as a function of air density is $V(m/s) = \rho_{air}(kg/m^3)^{-1/2} 156 D(m)^{1/2}$, assuming a hail density of 917 kg m^{-3} and a drag coefficient of 0.5.

Hail occurrence is largely confined to land areas and has a strong diurnal character with the peak in observations occurring in the late afternoon. Outside of the tropics a seasonal peak in hail occurrence is observed in early summer. Radar observations suggest that hail is more frequent close to the freezing level than at colder temperatures (higher altitudes).

While the model based approach provided a global climatology of hail at the surface only the radar based approach was able to provide information concerning variations with altitude. Therefore, probability tables for collisions with hail were constructed using the radar data. Using a value of 200 m^{-1} for the slope parameter in the exponential distribution means that these results are worst case estimates. They will not reflect typical conditions. Using the radar reflectivity pdf for over land, 16-20 LT (Local Time) and the JJA season gives rise to the highest probabilities for an aircraft flying randomly within different temperature ranges. Hail that is intercepted at approximately the 10^{-5} probability event level have diameters of about 70 mm for the -2 to -5C and -15 to -20C temperature ranges, but will be less than 10 mm for the -35 to -40C range. These values are similar for an aircraft intercepting particles along the leading edge and from above assuming forward and horizontal cross sectional areas of 50 and 400 m^2. For the case when only hail regions are encountered the diameter of hail at the 10^{-3} event level when flying in hail regions is 100 mm for all temperature ranges. On the ground the worst case size of hail at the 10^{-3} event level is ~110 mm. Hail sizes for other event levels and cases are given in table 16. This table was generated from those given in section 7 by choosing tabulated values close to the event levels quoted. The estimates at the 10^{-9} event level fall outside of the tables generated in the analysis. Therefore we have indicated that hail sizes for this level of event will exceed the largest considered in section 7. We feel that the extrapolation required to estimate more exact sizes at the 10^{-9} level would be too great.

			Probability level		
			10^{-3}	10^{-5}	10^{-9}
	Trange(C)				
In air					
Random flying	-2	-5	<<10 mm	70 mm	>90 mm
	-15	-20	<<10 mm	70 mm	>90 mm
	-35	-40	<<10 mm	10 mm	>90 mm
In hail	-2	-5	100 mm	120 mm	>120 mm
	-15	-20	100 mm	120 mm	>120 mm
	-35	-40	100 mm	120 mm	>120 mm
On ground					
Random weather			<<10 mm	90 mm	> 120 mm
In hail			110 mm	>110 mm	>110 mm

Table 16 Summary table of hail size encountered at the 10^{-3}, 10^{-5} and 10^{-9} event levels. Inequality symbols (<<, >) indicate that the sizes are beyond the bounds of the tables given in section 7. These values are based on the assumptions, such as cross sectional areas, given in the text.

The power of a model based or satellite based approach is that it can give a consistent global or near-global picture of hail. However, the results obtained are sensitive to the assumptions made. The probability results are based upon assumptions about the nature of the environment sampled by the radar and so the assumptions have been made to attempt to capture a worst case scenario. Therefore we believe that the hail sizes indicated for the different probability levels are conservative (i.e. larger hail than would be typically encountered).

It is inevitable that an aircraft will pass through a hailstorm at some stage during its lifetime and therefore will be subjected to some level of hail impact damage which depends not only upon the mass, velocity and impact angle of the hailstone (and indeed the number or intensity of hailstones), but also upon the geometry and material of the structure that is being impacted.

Composites offer many advantages as they are lightweight and strong but their laminated nature makes them susceptible to damage when impacted. In particular delamination may form internally between plies where it is difficult to detect and can adversely effect structural performance.

Factors governing the way in which ice develops to form a hailstone are also significant in terms of the impact damage the hailstone can inflict. At temperatures around 0^0C and similarly at high strain rates, ice tends to flow over the target structure, exhibiting plastic deformation; whereas below -15^0C, and at low strain rates, brittle failure is often evident. The interaction and differing mechanisms of energy transfer between the hailstone and the underlying impacted structure will have an affect on the failure mode and/or the extent of damage sustained. However, there is insufficient data available for any justifiable trends to be identified. Experimental evidence shows that ice which contains microcracks (voids, air bubbles) is inherently weaker, shattering on impact, and thus it can generate damage that is significantly different from that sustained by impacts from solid (clear) ice (i.e. it has the potential to activate alternative failure modes)

The most readily available standards acknowledge that hail is a threat to aircraft structure. The DEF STANs and MIL HDBKs define the hail environment including the global threat, hail size, density and velocity to define a risk from hail. However, most standards fail to consider that hail has unique traits that make it difficult to relate to other, more traditional, forms of impact in regard to the design/qualification requirements for aircraft structure, to meet the hail threat.

Standards related to impact damage resistance and damage tolerance are still very much under development (DEF STAN 00-970 updates in progress for Impact Damage Resistance), and only DEF STAN 00-35 provides a test methodology for a hail impact test. The limitations of such a test are noted, however, as being a limited impact test as it only deals with a single “one-off” occurrence. The tables generated from the radar data suggest that for hail sizes smaller than 50 mm in diameter, multiple hit scenarios need to be considered.

Aircraft operate over a wide temperature profile, from -50^0C to $+100^0$C and ice has been shown to be temperature sensitive. Hence, it is important to consider and appropriately select which temperatures should be used during ice impact tests. Individual hailstones may not necessarily constitute a high risk, but they do have the potential to collectively generate damage that coalesces into a large area of delamination.

Ice is strain rate sensitive exhibiting a ductile behaviour at low strain rates and brittle behaviour at high strain rates.

The use of metallic spheres during impact tests does not provide an impact event which is representative of actual ice impacts. This is because the unique crush behaviour of ice will affect the damage sustained. The ice impactor must also be free from microcracks and maintain its integrity prior to impact. Due to the inherent complex nature of composite materials and the way in which different failure modes (and damage) develop in relation to the impactor velocity, the impactor material and impactor shape, it is not possible to state that a metal impactor is more or less conservative than an ice impactor. As discussed in Section 8.4.7 the response exhibited by both is significantly different due to the way in which energy transfer occurs between the two impacting bodies. It is also debatable as to what should be considered to be more ‘severe’ damage: a small perforation/hole or an extensive area of delamination/disbond, (see section 8.4.2).

The amount of damage generated by an ice impact is related to its mass, velocity and angle of impact, the geometry or structural configuration and material properties of the target. Any additional loading, either before or after the impact event, can also have a significant effect on the damage produced.

Composites are inherently vulnerable to out-of-plane (i.e. loads perpendicular to the laminate) loads such as those generated under impact. The concern is that this form of damage (termed Barely Visible Impact

Damage or BVID) is extremely difficult to detect from a surface inspection and requires specialist equipment such as C-scans to identify it. If left undiagnosed, BVID has the potential to lead to a serious failure.

Due to the complex response behaviour of composites under impact it is difficult to form a direct correlation between the hailstone size/mass and the level of damage sustained. As the hailstone size/mass increases, the damage generated within the composite material changes from matrix cracking, shear cracking, delamination, fibre failure to punch through, with a combination of these different failure modes, occurring at any one time. It is a matter of judgement as to whether an aircraft structure containing a large area of delamination and debonding (generated by a higher mass, low velocity ice impacts) or a small perforation displaying very localised fibre and matrix cracking (generated by a low mass, higher velocity ice impact but having the same kinetic energy) is the greater threat to aircraft structural performance.

This work clearly illustrates that, in the development of certification standards, a range of hail masses and velocities, which generate a combination of composite failure modes, including delamination and/or fibre failure must be considered.

11 Implications

A consistent global hail climatology provided by satellite offers the safety community a way of estimating route-based and fleet exposure risks. Knowledge about geographical, seasonal and diurnal behaviour of hail occurrence could be used to plan aircraft routing. The limitation of the model climatology is that it is a diagnostic designed for predicting effects at the surface. Increased model resolution in the forthcoming years will allow more advanced diagnostic relations to be implemented and regional scale high resolution modelling of prognostic graupel and hail amounts. Therefore it would be useful to ***develop more powerful global model-based diagnostics to predict hail vertical profiles for use with higher resolution global models (e.g. 25km UK Met Office model becomes operational in Jan 2010).***

The satellite radar approach provides vertical information, but the coverage of the TRMM radar is between 37N and 37S. The probability tables presented in this study are dependent upon the assumptions made about the hail environment that the radar is sampling. The sensitivity studies have shown that the assumed slope parameter in the exponential distribution can strongly modify the results. ***Analysis of legacy aircraft data and further analysis of hail pad data to provide pdfs of the slope parameter are required.***

To avoid having to make an assumption about one of the exponential distribution parameters it may be possible to make use of other datasets such as lightning flash rate and microwave brightness temperatures in combination with reflectivity to provide estimates of both the exponential distribution parameters. Such an approach would introduce other assumptions such as vertical structure and models that link hail amount to lightning flash rate. Nevertheless, it is likely that it would be useful to ***develop multi-parameter satellite***

retrievals based on radar, passive microwave sampling and perhaps lightning information. This could potentially better characterise the size distributions of the hail.

12 Recommendations

Based on the results of this study the following recommendations are made:

- A simple reproducible hail particle model that is free of microcracks needs to be developed for physical testing of aircraft materials. The worst case impactor is a solid ice sphere. Metal spheres are not good hail models. [section 8.4]

- Assuming an aircraft is flying in hail and a 10^{-3} event level is considered as a design safety threshold, then impacts from hail sizes up to 110 mm in diameter (solid ice) need to be evaluated in the design of aircraft structures. [section 7.2.4]

- The effect of multiple hits by hail smaller than 50 mm in diameter needs to be considered in aircraft design. This requires the development of montecarlo multiple strike computer codes and methods of preparing and firing multiple impactors at test targets. Multiple strikes could potentially lead to delamination of composites over a large area. [section 7.2.5]

- Hail impact tests need to be considered across the operating temperature range of aircraft because the mechanical characteristics of ice vary with temperature. [section 8.4]

13 References and Glossary

Anghileri M, Castelletti L, Invernizzi F and Mascheroni M, “A survey of numerical models for hail impact analysis using explicit finite element codes”, International Journal of Impact Engineering, Vol 31, 2005.

Asp, L. and R. Juntikka, 2009. High velocity impact on NCF reinforced composites SICOMP, Composites Science and Technology, 69, 1478–1482.

Auer AH and Marwitz JD, 1972. Hail in the vicinity of organised updrafts. J Appl. Met., 11, 748-752.

Barge, B.L., Isaac, G.A. 1973, The shape of Alberta hailstones, Journal de Recherchés Atmosphériques, Vol. 7 ,11-20.

Bashkirova, G.M. and T.A. Pershina. 1964. O masse snezhinok iskorosti ikh padeniya [On the mass of snow crystals and their fall velocity]. Trudy GGO, 165, 83–101.

Braham, R.R., 1963: Some Measurements of Snow Pellet Bulk-Densities. J. Appl. Meteor., 2, 498–500.

Blyth A. M., H.J. Christian Jr., K. Driscoll, A.M. Gadian, John Latham, 2001: Determination of ice precipitation rates and thunderstorm anvil ice contents from satellite observations of lightning. Atmospheric Research 59-60 (2001) 217– 229

Brimelow, J.C., G.W. Reuter, and E.R. Poolman, 2002: Modeling Maximum Hail Size in Alberta Thunderstorms. Wea. Forecasting, 17, 1048–1062.

Brimelow, J.C., G.W. Reuter, R. Goodson, and T.W. Krauss, 2006: Spatial Forecasts of Maximum Hail Size Using Prognostic Model Soundings and HAILCAST. Wea. Forecasting, 21, 206–219.

Browning K.A. 1985: Morphology and classification of middle-latitude thunderstorms. In 'Thunderstorm morphology and dynamics' Ed Kessler E., University of Oklahoma Press.

Browning, K.A., 1963: The growth of large hail within a steady updraught. QJR Meteorol. Soc., 89, 490-506.

Buckley M. 2007. Future needs for technical textiles in Aerospace, Technical textiles in composite structures, NCN seminar.

Castellano, NE; Nasello, OB. 1997. Comments about the drag laws used in hail growth simulations. Atmos. Res. 43 (4): 315-323.

Castellano, NE; Nasello, OB; Levi, L. 2002. Study of hail density parametrizations. Q. J. Royal Meteorol. Soc. 128 (583): 1445-1460, Part A.

Cecil, DJ, 2009.Passive Microwave Brightness Temperatures as Proxies for Hailstorms. Journal of Applied Meteorology and Climatology, 48 (6): 1281-1286.

Changnon, S.A., 1999: Data and approaches for determining hail risk in the contiguous United States. J. Appl. Met. , 38, 1730-1739.

Cheng, L., and M. English, 1983: A Relationship Between Hailstone Concentration and Size. J. Atmos. Sci., 40, 204–213.

Christian HJ et al. 2003. Global frequency and distribution of lightning as observed from space by the optical transient detector. J. Geophys. Res., 108, D1, 4005, doi:10.1029/2002JD002347.

Court A., and Griffiths J.F. 1986: Thunderstorm climatology. In 'Thunderstorm morphology and dynamics' Ed Kessler E., University of Oklahoma Press.
D00A18, doi:10.1029/2008JD009982.

Dalezios, N.R. and N.K. Papamanolis, 1991: Objective assessment of instability indices for operational hail forecasting in Greece. Meteorol. and Atmos. Physics, 45, 87-100.

Das, M., Oterkus, E., Madenci, E. and H. Razi, 2009. Residual strength of sandwich panels with hail damage, Composite Structures, 88, 403-412.

Dehenauw, D., 2003. An objective hail size forecasting method based on mesoscale model output. Scientific publication, Royal Meteorological Institute of Belgium. Available at www.kmi.be/meteo/download/de/519779/pdf/rmi_scpub-022.pdf

Deierling W, Petersen WA, Latham J, Ellis S and Christian H. 2008. The relationship between lightning activity and ice fluxes in thunderstorms. J. Geophys. Res., 113, D15210 doi:10.1029/2007JD009700.

Dessens J. 1986. Hail in Southwestern France. I: Hailfall characteristics and hailstorm environment. J. Clim. Appl. Met., 25, 35-47.

Dessens, J., Fraile, R., Pont, V. and J.L. Sanchez, 2001: Day-of-the-week variability of hail in south-western France. Atmos. Research, 59, 63-76.

Donavon, RA; Jungbluth, KA, 2007. Evaluation of a technique for radar identification of large hail across the upper midwest and central plains of the United States. Weather and Forecasting, 22 (2): 244-254.

Edwards, R. and R.L. Thompson, 1998: Nationwide comparisons of hail size with WSR-88D vertically integrated liquid water and derived thermodynamic sounding data.
Wea. and Forecasting, 13, pp277-285.

Etkin, D. and S.E. Brun, 1999: A note on Canada's hail climatology: 1977-1993. Int. J. Climat., 19, 1357-1373.

European Severe Storms Laboratory (ESSL) – preliminary hail climatology 2000-2007. http://www.essl.org/research/

Fawbush, E.J. and R.C. Miller, 1953: A method for forecasting hailstone size at the earth's surface. Bull. Am. Meteorol. Soc., 34, 235-244.

Fawcett, A., Trostle, J. and S. Ward, 1997. 777 Empennage Certification Approach, The 11th International Conference on Composite Materials (ICCM-11), Gold Coast, Australia, July 14-18.

Federer B and Waldvogel A, 1975. Hail and raindrop size distributions from a Swiss multicell storm. J. Appl. Met., 14, 91-97.

Ferguson R., 2004. Large scale composite testing at Airbus Filton site, 2nd International Conference on Composites Testing and Model Identification.

Ferraro, RR; Weng, FZ; Grody, NC; Zhao, LM; Meng, H; Kongoli, C; Pellegrino, P; Qiu, S; Dean, C. 2005. NOAA operational hydrological products derived from the advanced microwave sounding unit. IEEE Transactions on Geoscience and Remote Sensing 43 (5): 1036-1049.presented at 8th Specialist Meeting on Microwave Radiometry and Remote Sensing Applications in Rome, Italy, Feb 24-27, 2004.

Ferrier, B.S., W.K. Tao, and J. Simpson, 1995: A Double-Moment Multiple-Phase Four-Class Bulk Ice Scheme. Part II: Simulations of Convective Storms in Different Large-Scale Environments and Comparisons with other Bulk Parameterizations. J. Atmos. Sci., 52, 1001–1033.

Foreman A., 2003. A Review of the Damage Tolerance Capability of Typhoon Carbon Fibre Composite Structure, QinetiQ Technical Report No. QINETIQ/FST/WP032183, September 2003.

Fraile, R., Berthet, C., Dessens, J. and J.L. Sanchez, 2003: Return periods of severe hailfalls computed from hailpad data. Atmos. Research, 67-8, 189-202.
Fraile, R; Sanchez, JL; de la Madrid, JL; et al.1999. Some results from the hailpad network in Leon (Spain): Noteworthy correlations among hailfall parameters. Theoretical and Applied Climatology, 64 (1-2): 105-117.

Frisby, E.M. and H.W. Sansom, 1967: Hail incidence in the Tropics. J. Appl. Met., 6, 339-354.

Giaiotti, D., Nordio, S. and F. Stel, 2003: The climatology of hail in the plain of Friuli Venezia Giula. Atmos Research, 67-8, 247-259.

Golding, B.W., 1998: Nimrod: a system for generating automated very short range forecasts. Meteorol. Applications, 5, 1-16.

Gordon, J.D., 2000: A comprehensive severe weather forecast checklist and reference guide. NOAA Technical Service publication. CR-10.

Griffiths B., 2005. Boeing sets pace for composite usage in large civil aircraft, High Performance Composites. http://www.compositesworld.com/articles/boeing-sets-pace-for-composite-usage-in-large-civil-aircraft.aspx

Hand, W.H., 2000: An investigation into the potential of Miller's technique for forecasting large hail. Met Office, Forecasting Research Technical Report, No. 329. (Unpublished report available at http://www.metoffice.gov.uk/research/nwp/publications/papers/technical_reports/2000/FRTR329/FRTR329.pdf)

Hand, W.H., 2001: Automated severe weather prediction project case studies - Part 2. Met Office, Forecasting Research Technical Report, No. 323. (Unpublished report available at http://www.metoffice.gov.uk/research/nwp/publications/papers/technical_reports/2001/FRTR323/FRTR323.pdf).

Heymsfield, A.J., 1978. The characteristics of graupel particles in northeastern Colorado cumulus congestus clouds. J. Atmos. Sci., 35, 284-295.

Heymsfield, A.J., and M. Kajikawa, 1987: An Improved Approach to Calculating Terminal Velocities of Plate-like Crystals and Graupel. J. Atmos. Sci., 44, 1088–1099.

Hohl R, Schiesser H and Aller D, “Hailfall: the relationship between radar-derived hail kinetic energy and hail damage to buildings”, Atmospheric Research, Vol 63, 2002.

Johnson A, Holzapfel M, Kraft H, and Reiter A, “Measurement of Ice Mechanical Properties”, DLR Report-IB 435 – 2006/55, 2006.

Kelly DL, Schaefer JT and C.A. Doswell 1985. Climatology of non-tornadic severe thunderstorm events in the United States. Mon. Weath. Rev., 113, 1997-2014.

Kim H and Kedward K, “Experimental and numerical analysis correlation of hail ice impacting composite structures”, 40th AIAA/ASME/ASCE/AHS/ASC Structures, Structural Dynamics, and Materials Conference, St Louis, April 12-15, 1999.

Kim, H. and K. Kedward, 2000. Modelling hail ice impacts and predicting impact damage initiation in composite structures, AIAA Journal, 38, No. 7.

Kim, H. Welch, D. and K. Kedward, 2003. Experimental investigation of high velocity ice impacts on woven carbon/epoxy composite panels, Composites: Part A, 34, 25-41.

Knight C.A. and Knight N.C., 2001. Hailstorms. In 'Severe Convective Storms' Ed. Doswell C.A., AMS Met. Mono. Ch6, 223-254.

Knight C.A. and Knight N.C., 2005. Very large hailstones from Aurora, Nebraska. Bull. Americ. Met. Soc., 12, 1773-1781.

Knight C.A. and Squires P., 1982: The National Hail Research. Col. Assoc. Univ. Press. Two volumes.

Knight C.A., Miller L.J., Knight N.C. and Breed D., 1982: The 22 June 1976 Case Study: Precipitation Formation. In ‘Hailstorms of the Central High Plains. Volume 2. Case studies of the National Hail Research Experiment’ edited by Knight C.A. and Squires P. Col. Assoc. Univ. Press.

Knight C.A., Smith P. and Wade C., 1982: Storm types and some radar reflectivity characteristics. In 'Hailstorms of the Central High Plains. Volume 1. The National Hail Research Experiment' edited by Knight C.A. and Squires P. Col. Assoc. Univ. Press.

Knight, NC; Heymsfield, AJ. 1983. Measurement and interpretation of hailstone density and terminal velocity. Journal of the Atmospheric Sciences 40 (6): 1510-1516.

Latham J, Petersen WA, Deierling W, Christiam HJ. 2007. Field identification of a unique globally dominant mechanism of thunderstorm electrification. Q. J. Roy. Meteorol. Soc., 133, 1453-1457.

Lay EH, Jacobson AR, Holzworth RH, Rodger CJ and Dowden RL. 2007. Local time variation in land/ocean lightning flash density as measured by the world wide lightning location network. 2007, 112, D13111, doi:10.1029/2006JD007944.

Lin, Y.L., R.D. Farley, and H.D. Orville, 1983: Bulk Parameterization of the Snow Field in a Cloud Model. J. Appl. Meteor., 22, 1065–1092.

List R. 1985: Properties and growth of hailstones. In 'Thunderstorms: a social, scientific and technological documentary. Vol 2. Thunderstorm morphology and dynamics.' 2nd edition. Edited by E. Kessler, University of Oklahoma Press.

Liu, CT; Zipser, EJ; Cecil, DJ; et al. 2008. A Cloud and Precipitation Feature Database from Nine Years of TRMM Observations. Journal of Applied Meteorology and Climatology, 47 (10): 2712-2728.

Locatelli, J. D. and P. V. Hobbs. "Fall Speeds and Masses of Solid Precipitation Particles." J. Geophys. Res., 79, 2185-2197.

Long, A.B., 1980: On estimating hailfall frequency and hailfall area. J. Appl. Meteor., 19, 1351–1362.

Lozowski E.P. and Beattie A.G., 1979: Measurements of the kinematics of natural hailstones near the ground. Q. J. Roy. Meteorol. Soc., 105, 453-459

Macklin W.C., 1962: The density and structure of ice formed by accretion. Q. J. Roy. Meteorol. Soc., 88, 30-50.

Macklin W.C., Strauch E., Ludlam F.H., 1960: The density of hailstones collected from a summer storm. Nubila, 3,12-17.

Magono, C., 1953. On the growth of snowflakes and graupel. Science Report. Yokohama National University, Japan, Ser. I, No. 2, 18–40

Mahinfalah, M. and R. Skordahl, 1998. The effects of hail damage on the fatigue strength of a graphite/epoxy composite laminate, Composite Structures, 42.

Matson, R.J., and A.W. Huggins, 1980: The Direct Measurement of the Sizes, Shapes and Kinematics of Falling Hailstones. J. Atmos. Sci., 37, 1107–1125.

Milbrandt, J.A., and M.K. Yau, 2005: A Multimoment Bulk Microphysics Parameterization. Part I: Analysis of the Role of the Spectral Shape Parameter. J. Atmos. Sci., 62, 3051–3081

Miller, R.C., 1972: Notes on analysis and severe storm forecasting procedures of the Air Force Global Weather Center. AWS Technical report 200 (Rev), Headquarters, Air Weather Service, Scott AFB, IL, 106pp.

Mills M R and Hallam S D, "Ice loading on off-shore structures: The influence of ice strength", Euromech 239, 152-167, Leicester University, 1988.

Morgan G. M., 1982: Precipitation at the ground. In 'Hailstorms of the Central High Plains. Volume 1. The National Hail Research Experiment' edited by Knight C.A. and Squires P. Col. Assoc. Univ. Press.

Morgan G.M. and Summers P.W., 1986: Hailfall and hailstorm characteristics. In 'Thunderstorm morphology and dynamics' Ed Kessler E., University of Oklahoma Press.

Morrison, H., J.A. Curry, M.D. Shupe, and P. Zuidema, 2005: A New Double-Moment Microphysics Parameterization for Application in Cloud and Climate Models. Part II: Single-Column Modeling of Arctic Clouds. J. Atmos. Sci., 62, 1678–1693.

Musil DJ, Christopher SA, Deola RA and Smith PL, 1991. Some interior observations of southeastern Montana hailstorms. J. Appl. Met., 30, 1596-1612.

Musil et al., 1976: Structure of an evolving hailstorm, Pt IV: Internal structure from a penetrating aircraft. Mon. Wea. Rev., 104, 596-602.

NSSL (USA) http://www.nssl.noaa.gov/primer/hail/hail_climatology.html

Petersen, W. A., H. J. Christian, and S. A. Rutledge (2005), TRMM observations of the global relationship between ice water content and lightning, Geophys. Res. Lett., 32, L14819, doi:10.1029/2005GL023236.

Peterson et al., 1991: Computerized reduction of airborne foil impactor data. J. Atmos. Ocean. Tech., 8, 691-696

Pflaum, J., and H. Pruppacher, 1979: A Wind Tunnel Investigation of the Growth of Graupel Initiated from Frozen Drops. J. Atmos. Sci., 36, 680–689.

Prodi, F., 1970: Measurements of Local Density in Artificial and Natural Hailstones. J. Appl. Meteor., 9, 903–910.

Rasmussen, RM; Heymsfield, AJ. 1987. Melting and shedding of graupel and hail Part II sensitivity study. Journal of the Atmospheric Sciences 44 (19): 2764-2782.

Reisner J, Rasmussen RM, Bruintjes RT, 1998. Explicit forecasting of supercooled liquid water in winter storms using the MM5 mesoscale model. Q. J. Roy. Meteorol. Soc., 124, 1071-1107.

Renick, J. H., and J. B. Maxwell, 1977: Forecasting hailfall in Alberta. Hail: A Review of Hail Science and Hail Suppression, Meteor. Monogr., No. 38, Amer. Meteor. Soc., 145–151.

Roberts T., 2008. The carbon fibre industry worldwide 2008-2014: An evaluation of current markets and future supply and demand, Materials Technology Publications, ISBN 1 871677 59 9.

Saunders C. 2008. Charge Separation mechanisms in clouds, Space Sci. Rev.,137, 335-353.

Schuster SS, Blong RJ, Speer MS, 2005. A hail climatology of the greater Sydney area and New South Wales, Australia. Int. J. Clim., 25, 1633-1650.

Segala, S., Sairouni, A. and J. Bech, 2002: Hail forecasts with NWP derived instability indices. European Geophysical Society, 4th Plinius Conference on Mediterranean Storms, Mallorca, Spain, 2-4 October 2002.

Shakina et al., 2000: Study of large-scale numerical scheme resources for identification of hail-hazard situations over the Northern Caucasus. Russian Met. and Hydrol., 4, 36-39.

Sioutas, M., Meaden, T. and J.D.C. Webb, 2009: Hail frequency, distribution and intensity in northern Greece. Atmos. Research., 93, 526-533.

Smith, S.B., Reuter, G.W. and M.K Yau, 1998: The episodic occurrence of hail in central Alberta and the highveld of South Africa. Atmos. Ocean, 36, pp169-178.

Spahn JF and Smith PL, 1976. Some Characteristics of Hailstone Size Distributions Inside Hailstorms. Preprint Volume: 17th Conference on Radar Meteorology. Oct 26-29, 1976, Seattle, Washington. AMS.

Steiner, J.T.,1989: New Zealand hailstorms. N. Z. J. Geol. Geophys. 32, pp279–291.

Straka, J.M., and E.R. Mansell, 2005: A Bulk Microphysics Parameterization with Multiple Ice Precipitation Categories. J. Appl. Meteor., 44, 445–466.

Straka, J.M., D.S. Zrnić, and A.V. Ryzhkov, 2000: Bulk Hydrometeor Classification and Quantification Using Polarimetric Radar Data: Synthesis of Relations. J. Appl. Meteor., 39, 1341–1372.

Thompson, G., R.M. Rasmussen, and K. Manning, 2004: Explicit Forecasts of Winter Precipitation Using an Improved Bulk Microphysics Scheme. Part I: Description and Sensitivity Analysis. Mon. Wea. Rev., 132, 519–542.

TorDACH http://www.tordach.org/de/hail.htm

Tuovinen J. et al., 2006: A climatology of large hail in Finland. AMS 23rd Conference on local storms. http://ams.confex.com/ams/pdfpapers/115408.pdf

Ulbrich, C.W., and D. Atlas, 1982: Hail Parameter Relations: A Comprehensive Digest. J. Appl. Meteor., 21, 22–43.

Vinet, F., 2001: Climatology of hail in France. Atmos. Research, 56, 309-323.

Vittori O. and Di Caporiacco G., 1959: The density of hailstones. Nubila, 2, 51-57.

Webb JDJ, Elsom DM, Reynolds DJ. 2001. Climatology of severe hailstorms in Great Britain. Atmos Research. 56, 291-308.

Webb, J.D.C., Elsom, D.M. and G.T. Meaden, 2009: Severe hailstorms in Britain and Ireland, a climatological survey and hazard assessment. Atmos. Research. 93, 587-606.

Weng, FH; Grody, NC. 2000. Retrieval of ice cloud parameters using a microwave imaging radiometer. Journal of the Atmospheric Sciences 57 (8): 1069-1081.

Willows M., 2007. An Overview of Progress on GARTEUR AG30 - High Velocity Impact, QINETIQ/EMEA/S&DU/TR0701900.

Witt, A; Eilts, MD; Stumpf, GJ; et al. 1998. An enhanced hail detection algorithm for the WSR-88D. Weather and Forecasting, 13 (2): 286-303.

Zhang C., Zhang Q., Wang Y. 2008. Climatology of hail in China:1961-2005. J. Appl. Met. Clim., 47, 795-804.

Zikmunda, J., and G. Vali, 1972: Fall Patterns and Fall Velocities of Rimed Ice Crystals. J. Atmos. Sci., 29, 1334–1347.

Zipser, EJ; Cecil, DJ; Liu, CT; Nesbitt, SW; Yorty, DP. 2006. Where are the most intense thunderstorms on earth?. Bulletin of the American Meteorological Society 87 (8): 1057-1071

References for section 4.9

New ref #	Reference	Notes
1.	Composites @ Airbus, Damage Tolerance Methodology – presented by Presented by Chantal FUALDES at the FAA Workshop for Composite Damage Tolerance and Maintenance, July 19-21, 2006	Airbus composites presentation including a slide on hail.
2.	MIL-HDBK-17-3F, Volume 3, Chapter 7, Damage Resistance, Durability and Damage Tolerance	
3.	DEF STAN 00-35, Part 4, Issue 4 – Chapter 7.01 – Hail, Snow and Ice.	Defines the hail environment.
4.	MIL-HDBK-310 – Global climate data for Developing Military Products (23rd June 1997)	Defines the hail environment.
5.	DEF STAN 00-35, Part 4, Issue 4 – Chapter 7.02 – The Effects of Hail, Snow and Ice.	Defines the typical damage that might be caused by impact from hail.
6.	Gringorten, 1.1. (1972) Hailstone Extremes for Design, AFCRL-TR-72- 081, Air Force Surveys in Geophysics No. 238, AD743831.	
7.	The “New Champ” Hailstone, Weatherwise 24, 4:151, Ludlum D (ed.)	Magazine article detailing a new hailstone record.
8.	Certification Specifications for Normal, Utility, Aerobatic, and Commuter Category Aeroplanes CS-23. ED Decision 2003/14/RM Final 14/11/2003	
9.	JAR 25 – Large Aeroplanes – Amendment 18.	
10.	DEF STAN 00-35, Part 2, Issue 4 – Chapter 3.10 – Hail Snow and Ice.	Introduces the tests related to hail.
11.	DEF STAN 00-35, Part 3, Issue 4 – Chapter 3.19 – Test CL19 – Erosion and Structural Damage in Flight by Rain, Hail, Dust or Sand	Test methodology for hail.
12.	The contribution of the Cavendish Laboratory to the understanding of solid particle erosion mechanics – S.M. Walle, J.E. Field – October 2004	Paper describing some of the solid particle erosion testing that has been conducted by the Cavendish Laboratory.
13.	DEF STAN 00-970, Part 7, Section 7 – Leaflet 700 Propulsion System Installations - Para 3.3	Rotorcraft section relating to ingestion of hail.
14.	DEF STAN 00970, Part 1, Section 5 – Power plant	Details the requirements for hail ingestion for fixed wing aircraft.

15.	DEF STAN 00-970 Part 11, Section 3 – 3.E790 – Ingestion of rain and hail.	This Part of the DEF STAN looks at the requirements for all propulsion systems fixed wing or rotorcraft. This includes the requirement for an analysis.
16.	FAA (Federal Aviation Regulations), Part 33, Section 78 – Rain and Hail ingestion	Definition of tests for hail ingestion into
17.	FAA (Federal Aviation Regulations), Appendix B to Part 33—Certification Standard Atmospheric Concentrations of Rain and Hail	
18.	ASTM F320-05 – Standard Test Method for Hail Impact Resistance of Aerospace Transparent Enclosures.	Test method.

Glossary

Accretion: In cloud physics, usually the growth of an ice hydrometeor by collision with supercooled cloud drops that freeze wholly or partially upon contact. (from the American Meteorological Society meteorological glossary)

Aggregates: Combinations of smaller pristine ice crystals that form through collision. They are commonly referred to as snowflakes.

AMS: American Meteorological Society

CAPE: convective available potential energy—(Abbreviated CAPE.) The maximum energy available to an ascending parcel, according to parcel theory. (from the American Meteorological Society meteorological glossary)

DJF, MAM, JJA, SON: Seasonal groupings of months commonly used in climatological studies. DJF: December-January-February. MAM: March-April-May. JJA: June-July-August. SON: September-October-November.

Graupel : Heavily rimed snow particles, often called snow pellets; often indistinguishable from very small soft hail except for the size convention that hail must have a diameter greater than 5 mm. (from the American Meteorological Society meteorological glossary)

Hail: Precipitation in the form of balls or irregular lumps of ice, always produced by convective clouds, nearly always cumulonimbus. An individual unit of hail is called a hailstone. By convention, hail has a diameter of 5 mm or more, while smaller particles of similar origin, formerly called small hail, may be classed as either ice pellets or snow pellets. (from the American Meteorological Society meteorological glossary)

LT Local Time. Approximated as GMT+Longitude(degrees)/15.

NCEP reanalysis data: National Centers for Environmental Prediction reanalysis data. Reanalysis provides a global historical view of the meteorological environment using a single numerical weather prediction model as a reference combined with different observation sources.

NWP: Numerical Weather Prediction. The combination of fluid dynamics, physical processes and initialising data to forward model the current weather conditions and predict the weather over timescales of a few days.

ROI: Region of Interest

Appendix 1 - Useful relationships for exponential distributions

An exponential distribution representation of the graupel and hail size distribution can be easily integrated to find useful bulk parameters. Concentration is obtained by integrating the size distribution

$$concentration = \int_0^\infty N_0 \exp(-\lambda D) dD = N_0 \frac{\Gamma(1)}{\lambda} \quad \text{m}^{-3}, \qquad \text{(A1)}$$

where Γ is the gamma function.

Hail or graupel water content is given by integrating the hail or graupel mass over the size distribution

$$hail\_water\_content = \int_0^\infty N_0 \exp(-\lambda D) \frac{\pi}{6} D^3 \rho_{hail} dD = \frac{\pi}{6} N_0 \rho_{hail} \frac{\Gamma(4)}{\lambda^4} \quad \text{kg m}^{-3}, \qquad \text{(A2)}$$

where ρ_{hail} is the density of hail.

Therefore, if hail_water_content can be determined from a climatology then we can either choose values for N_0 or λ and determine the other, or make use of relationships linking N_0 to λ and determine both. Once these parameters defining the exponential distribution are known other bulk parameters can be estimated.

The kinetic energy density is computed by integrating over the size distribution. Considering the horizontal collision between hail and an aircraft travelling with a true air speed, v_{tas}, the kinetic energy density is

$$KEdensity\_hor = \frac{1}{2} \int_0^\infty N_0 \exp(-\lambda D) \frac{\pi}{6} D^3 \rho_{hail} v_{tas}^2 dD = \frac{\pi}{12} N_0 v_{tas}^2 \rho_{hail} \frac{\Gamma(4)}{\lambda^4} \quad \text{J m}^{-3}. \qquad \text{(A3)}$$

The flux of kinetic energy density is

$$KEdensityflux\_hor = \frac{\pi}{12} N_0 v_{tas}^3 \rho_{hail} \frac{\Gamma(4)}{\lambda^4} \quad \text{J m}^{-2}\ \text{s}^{-1}. \qquad \text{(A4)}$$

For the case where the motion of the hail particle is due to its terminal velocity and ignoring any additional motion due to vertical winds, the kinetic energy density is

$$KEdensity\_vert = \frac{1}{2} \int_0^\infty N_0 \exp(-\lambda D) \frac{\pi}{6} D^3 \rho_{hail} a^2 D^{2b} dD = \frac{\pi}{12} N_0 a^2 \rho_{hail} \frac{\Gamma(4+2b)}{\lambda^{4+2b}} \quad \text{J m}^{-3}, \qquad \text{(A5)}$$

Where the hail terminal velocity is $v_{hail}=aD^b$. The kinetic energy density flux will be

$$KEdensityflux\_vert = \frac{1}{2}\int_0^{\infty} N_0 \exp(-\lambda D)\frac{\pi}{6} D^3 \rho_{hail} a^3 D^{3b} dD = \frac{\pi}{12} N_0 a^3 \rho_{hail} \frac{\Gamma(4+3b)}{\lambda^{4+3b}}$$ J m^{-2} s^{-1}. (A6)

To convert these relations into values that can be compared with materials damage tests an exposure duration, t, and collision cross section, A, need to be assumed, giving

$$KE\_hor = \frac{\pi}{12} N_0 v_{tas}^3 \rho_{hail} \frac{\Gamma(4)}{\lambda^4} At$$ J and (A7)

$$KE\_vert = \frac{\pi}{12} N_0 a^3 \rho_{hail} \frac{\Gamma(4+3b)}{\lambda^{4+3b}} At$$ J (A8)

for horizontal and vertical collisions, respectively.

If the distributions are truncated or bulk values for certain size ranges are required then limits to the integration can be introduced. This will lead to the gamma function in the above equations being replaced by an incomplete gamma function.

Appendix 2 – Comparison of radar derived results with CMH-17-3F working draft (February 2010)

Volume 3, Chapter 12 Damage Resistance, Durability and Damage Tolerance contains a table (Table 12.5.2.5) relating to the probability of an aircraft being struck on the ground by hail. Based on the description given in section 12.10.2.1: "*The cumulative probability distribution of hail size detailed in Table 12.5.2.5 is based on hail records at 11 US airports collected by the US National Oceanographic and Atmospheric Administration (NOAA) between 1955 and 2006. This data is incomplete in that it only includes "severe" hail storms and the largest hail sizes within a storm (to the nearest 0.25 inches). The minimum hail diameter required to classify a storm as severe ranged from 0.53 inches at the beginning of the time period to the current limit of 0.75 inches. The reported data includes location, time of day, month, and year."* , the closest data given in this report is the 'in hail' data from table 12 in this study which refers to threat on the ground. We are not able to compare our in flight in hail or random flying data with this table.

It is still difficult to do a direct comparison between table 12 and the CMH-17 table and it may not be possible without the application of many assumptions such as the effective sample volume appropriate for those observations. Reporting maximum size could be used to represent the slope of the hail size distribution during the storm, but the percentile that reported size represents would need to be known. Additionally, reporting maximum size means that hail sizes smaller than this size are probably simultaneously observed but do not contribute to the statistics. In contrast, the analysis presented in this study assumes an exponential size distribution and so all sizes are considered. The CMH-17 table is derived from storms of

variable duration and extent as well as the area used to report an observation of hail, the sample volume attached to each report of hail size is unknown. Therefore, it is not clear that comparing data from CMH-17 and table 12 will provide a like-with-like comparison.

Table 17 is a repeat of table 12.5.2.5 from the draft CMH-17 document. An additional column is also shown indicating values picked from table 12. It can be seen that the data from this study implies that hail 110 mm in size is as likely as 90 mm hail (3.75 inches) from the CMH-17 table. For these large sizes the radar based estimates are about 20 mm larger for a given probability. Additionally, table 12 indicates that for the 48 dBZ threshold, an aircraft located below such a region populated by hail will be encounter hail up to 70 mm in size. This is in contrast to the CMH-17 table that indicates that encountering hail of such a size is unlikely. The data derived from the radar observations is worst case and dependent upon the assumptions made. We chose to use a worst case parameter value for the slope of the size distribution. If a different value for the slope of the size distribution were used (λ) the probabilities could potentially be brought into closer agreement. Therefore the recommendation that size distribution of the hail is better characterised is important for reconciling these two datasets.

Diameter		Volume		Mass		Terminal Velocity		Kinetic Energy		Cumulative Probability of Occurrence	Prob from radar study
in	cm	in^3	cm^3	lb	g	ft/s	m/s	in-lb	J		
0.25	0.64	0.01	0.13	0.0003	0.12	32.29	9.84	0.05	0.01		
0.50	1.27	0.07	1.07	0.0021	0.97	45.66	13.92	0.83	0.09		
0.75	1.91	0.22	3.62	0.0072	3.26	55.93	17.05	4.21	0.47	21.7%	
1.00	2.54	0.52	8.58	0.0170	7.72	64.58	19.68	13.31	1.50	48.1%	
1.20	3.05	0.90	14.83	0.0294	13.34	70.74	21.56	27.61	3.10	64.7%	
1.25	3.18	1.02	16.76	0.0333	15.08	72.20	22.01	32.51	3.65	68.1%	
1.50	3.81	1.77	28.96	0.0575	26.06	79.09	24.11	67.41	7.57	81.4%	
1.70	4.32	2.57	42.15	0.0837	37.94	84.20	25.66	111.21	12.49	88.3%	
1.75	4.45	2.81	45.98	0.0913	41.39	85.43	26.04	124.88	14.03	89.6%	
1.76	4.47	2.85	46.78	0.0928	42.10	85.67	26.11	127.76	14.35	**89.9%**	
2.00	5.08	4.19	68.64	0.1362	61.78	91.33	27.84	213.04	23.93	94.4%	
2.04	5.18	4.45	72.84	0.1446	65.56	92.24	28.11	230.60	25.91	**95.0%**	
2.25	5.72	5.96	97.73	0.1940	87.96	96.87	29.52	341.24	38.34	97.1%	
2.40	6.10	7.24	118.61	0.2354	106.75	100.05	30.49	441.75	49.63	98.1%	
2.50	6.35	8.18	134.07	0.2661	120.66	102.11	31.12	520.11	58.43	98.5%	
2.75	6.99	10.89	178.44	0.3541	160.60	107.09	32.64	761.49	85.55	**99.3%**	←1%
2.76	7.01	11.01	180.40	0.3580	162.36	107.29	32.70	772.63	86.80	99.3%	
3.00	7.62	14.14	231.67	0.4597	208.50	111.85	34.09	1078.49	121.16	99.7%	←40%
3.25	8.26	17.97	294.54	0.5845	265.09	116.42	35.48	1485.48	166.88	99.8%	
3.50	8.89	22.45	367.88	0.7301	331.09	120.82	36.82	1998.04	224.47	**99.9%**	←99%
3.75	9.53	27.61	452.47	0.8979	407.22	125.06	38.12	2633.04	295.80	100.0%	
4.00	10.16	33.51	549.13	1.0898	494.22	129.16	39.37	3408.57	382.93	100.0%	
4.25	10.80	40.19	658.67	1.3071	592.80	133.13	40.58	4343.98	488.02	100.0%	←99.9%
4.50	11.43	47.71	781.87	1.5516	703.68	136.99	41.75	5459.87	613.38	100.0%	

Table 17 Copy of table 12.5.2.5 from CMH-17-3F draft. The additional column indicates the equivalent probabilities taken from table 12 for the aircraft on the ground in hail case. The cumulative probability column indicates the probability of observing a hailstone size smaller than the size given in the first column. Therefore, the probability of observing a hailstone larger than a given size is 1-cumulative probability.